A comprehensive model of the superluminescent diode

Middlemast, Ian

Award date:
1986

Awarding institution:
University of Bath

A COMPREHENSIVE MODEL OF THE SUPERLUMINESCENT DIODE

submitted by Ian Middlemast
for the degree of PhD
of the University of Bath
1986

I. Middlemast

ProQuest LLC
789 East Eisenhower Parkway
P.O. Box 1346
Ann Arbor, MI 48106-1346

CONTENTS PAGE

SUMMARY

This thesis describes a comprehensive model of the superluminescent diode. Many new features have been included in the model. They include: an approximate one-dimensional formulation which, however, still yields the lateral far-intensity 'angular' distribution; a detailed representation of the wavelength dependency of the local gain and spontaneous emission distributions derived from the basic semiconductor band structure; the inclusion of polarisation dependent confinement factors, reflectivities and seperate spontaneous emission coupling factors for each polarised mode. Consequently this model is capable of reproducing the light/current characteristics, spectral distributions, lateral far-intensity distributions and polarisation properties of SLDs. A comparison between theoretical and experimental results is given for all the above mentioned features. Of particular interest is the very wide range of wavelengths and current densities over which the theoretical and experimental spectral distributions agree. Results also suggest that the change in the degree of polarisation with current is dominated by the difference in the TE and TM confinement factors. A further conclusion is that the fraction of spontaneous emission coupling into the TE mode is significantly larger than that coupling into the TM mode. This result has some practical implications when applied to active waveguides and laser amplifiers where methods of reducing spontaneous emission, a severe source of noise in such devices, are being sought. Methods of increasing the ouput power of the SLD are also examined. Theoretical results show the wavelength dependence of gain saturation in the SLD. This is shown to occur quite strongly with length and to a much lesser extent with current density.

ACKNOWLEDGEMENTS

The author wishes to express his gratitude to Dr. J.Sarma and Professor T.E.Rozzi for their expert guidance and supervision during this project.

Thanks are also due to Mr W.J.Liddell for many interesting and helpful discussions and also for the use of his computer model for calculating the local gain and spontaneous emission distributions.

Finally, the author wishes to thank the the Science and Engineering Research Council for their financial support, without which this work would not have been possible; the Universities of Bath and Liverpool for their resources and facilities; and British Telecom Research Labs, Martlesham Heath for supplying the superluminescent diodes.

CHAPTER 1

INTRODUCTION

1.1 Introductory Remarks.

The main purpose of this chapter is to provide an introduction to, and an overview of, the contents of this thesis. A description of the Superluminescent Diode, SLD, is given in section (1.2), together with the main reasons for choosing it as a topic for investigation. The close similarity between the SLD and the laser diode is highlighted because many of the technological advances made during the years of laser research have been applied directly to the SLD. The origin of the SLD also has close links with the development of the laser diode, so much so that the historical review, presented in section(1.3), would not be complete without a survey of laser diode research and it's part in the realisation of the optical communication systems that are in use today. The main objectives of this thesis are listed in section(1.4). The chapter ends with a survey of the contents of the thesis in section(1.5).

1.2 Superluminescent diodes.

The superluminescent diode, (SLD), belongs to a family of devices known as edge emitting LEDs (Light Emitting Diodes). An edge emitting diode can be defined as an LED in which the useful light is emitted in the plane of the junction and is collected from a cleaved edge. An illustration of a typical double heterostructure edge

emitting diode is illustrated in fig(1.1a), [1]. The double heterostructure confines carriers and light in the same way as it does for a laser diode, so that the far-intensity 'angular' distribution perpendicular to the plane of the junction is essentially the same for the edge emitting diode as it is for the laser. The far-intensity 'angular distribution in the plane of the junction is more complicated being dependent not only on the stripe dimensions, length and width, but also on the optical gain within the active region.

The fact that the inversion population in the double heterostructure material can possess significant optical gain means that lasing is a distinct possibility. Lasing is suppressed in the edge emitting diode shown in fig(1.1a) by including an unpumped, highly absorbing, region at the rear of the device thus destroying the optical feedback loop necessary for lasing action. It is worth mentioning, however, that if the drive current is large enough the absorbing region can be optically pumped to transparency and lasing does occur, but generally, with self sustained oscillations as seen in tandem laser structures, [2]. Structures such as the edge emitting diode and tandem lasers that possess both an active and passive region can show bistability and have therefore been investigated extensively, [2,3,4]. There are other methods of supressing lasing action, reducing the reflectivity of one, or both, facets of a laser diode with antireflection coatings, [5,6], fig(1.1b), or positioning the stripe contact at an angle to the facets of a laser diode, [7], fig(1.1c), Neither of these methods is quite so effective for making edge emitting diodes as using an unpumped region to surpress lasing. The technology for making antireflection coatings capable of reducing facet reflectivities to a low enough level,

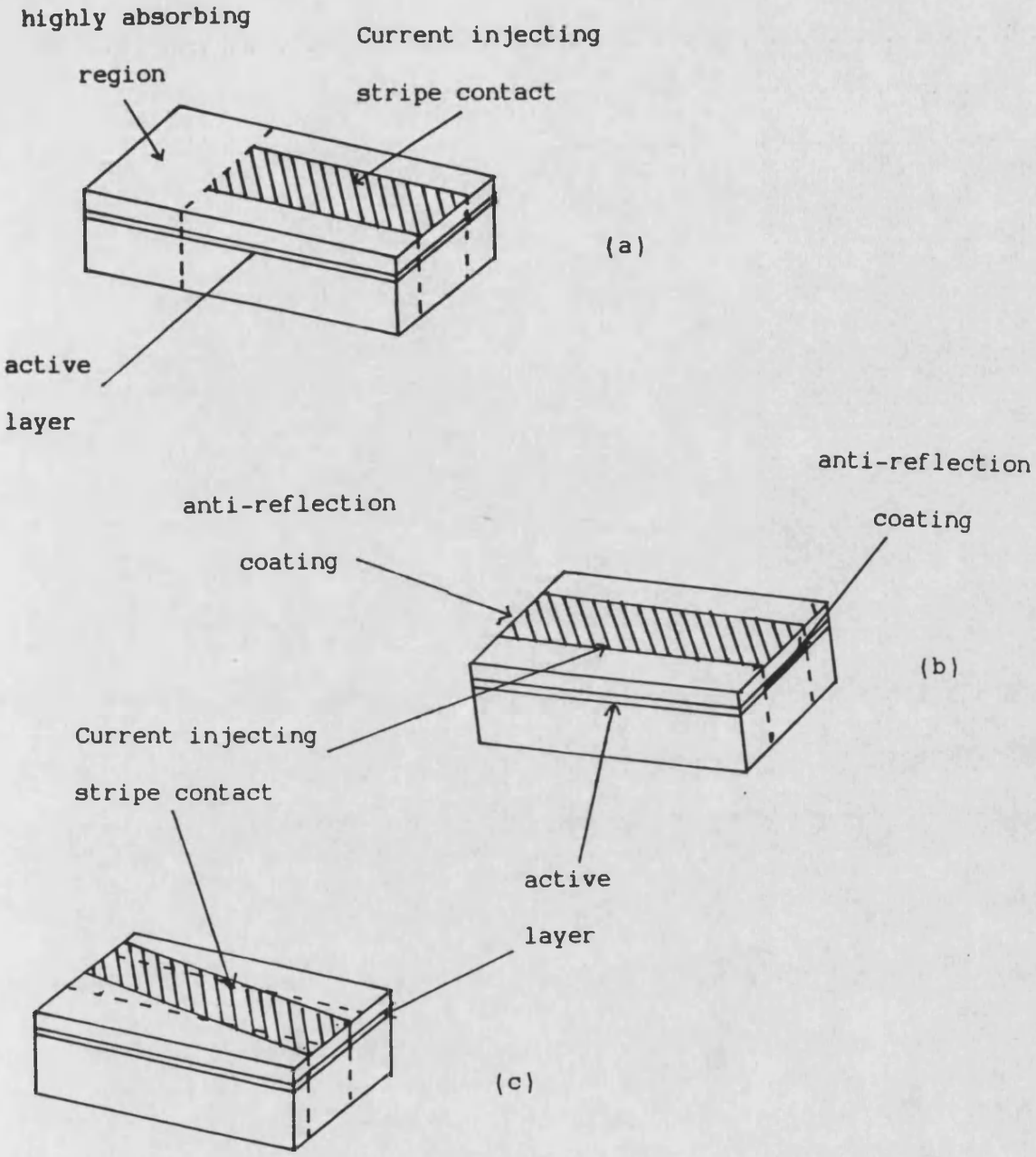

Fig(1.1) Schematic diagram of various SLD structures using different methods of suppressing optical feedback; a) highly absorbing region positioned at one end of the stripe contact; b) anti-reflection coatings on one or more facets; c) stripe contact positioned at an angle to the facets.

R ∿ 0.01%, to obtain significant output power from edge emitting diodes, made in this way, is only just becoming available, [8]. Angled stripe contact devices display lobes in their far-intensity 'angular' distributions making coupling to optical fibres difficult and inefficient, [7].

Edge emitting diodes can be subdivided into two groups;
1) restricted edge emitting diodes which are optimised for low current use with self absorption setting the optimum device length;
2) superluminescent diodes, SLDs, which are optimised for high current use and have significant optical gain along their length. It is this second category of device which provides the basis for this thesis.

1.21 Applications of Superluminescent diodes.

The SLD has characteristics that lie midway between that of the laser diode and the LED. Among the advantages of the SLD are less coherence and less susceptibility to thermal effects than the laser diode. It can also launch more power into an optical fibre, has a larger modulation bandwidth and a narrower spectral width than the surface emitting LED. These favourable properties make the SLD especially attractive for high speed communication systems operating over short distances. The SLDs short coherence length and its ability to deliver a significant ammount of power into a fibre make it an extremely useful device for reducing Rayleigh backscattering, a severe source of noise, in optical fibre gyroscopes. The relatively unpolarised nature of the SLDs light is also an advantage for reducing the polarisation noise in fibre gyroscopes. These properties are also likely to make the SLD useful in other fibre sensors where extremely low noise is required.

The SLD is not only a useful device in it's own right but it is also an extremely useful research tool in the field of integrated optics. The fact that the SLD is basically an active optical waveguide with an 'output port' allows information about the spontaneous emission, which can be regarded as noise in such systems, to be gathered. When the SLD has an anti-reflection coating applied to its output facet, and is highly pumped it provides information about the amplified spontaneous emission (noise) that is observed in single pass optical amplifiers. In fact the SLD model developed during this project has, with a few modifications and the addition of the field representation for the signal(s), been converted into a model for optical amplifiers, [9].

1.3 Historical Survey.

The light sources used in the optical fibre communication systems that are superseding the copper cable networks have a long history, brought about by some notable discoveries. It was as long ago as 1960 that the first laser was sucessfully operated by Maiman, [10]. Maiman's laser, a three level ruby laser, was quickly followed by the four level laser of Sorokin and Stevenson, [11], and by the first gas laser of Javan et al, [12]. During this period the p-n junction semiconductor laser was independently proposed by three groups, Nishizawa and Watanabe, [13], Basov et al, [14], and Agrain [15]. However, a quantitative understanding of the requirements for lasing to occur in a semiconductor was not available until 1961 when Bernard and Durafforg, [16], stated the necessary condition for stimulated emission in a semiconductor. Following this Dumke, [17], showed that laser action was indeed possible in direct bandgap semiconductors. He used available absorption data to show that

interband transitions in direct bandgap semiconductors such as Gallium Arsenide could produce the stimulated emission necessary for laser action. In 1962 three groups, Hall et al, [18], Nathan et al, [19], and Quist et al, [20], announced almost simultaneously the sucsessful operation of a semiconductor laser. Their lasers were all forward biased GaAs p-n junctions operating at cryogenic temperatures. Since the time of these initial discoveries many different laser materials have been found, operating over a wide range of wavelengths in the visible and infrared spectrum.

In the following years the development of semiconductor lasers recieved a great deal of attention because of likely applications in optical communications. It had been recognised that the semiconductor laser's unique ability to modulate it's optical output up to gigahertz rates by simply changing the current through the device gave it a distinct advantage over other types of lasers. However a number of factors hindered its initial use. First and foremost the atmospheric attenuation at the emission wavelength meant it was only useful over very limited distances. Secondly the modulation capacity of the laser was limited by the exceptionally large threshold currents at room temperature and the necessity of operating the device under very low duty cycle pulsed conditions. Finally the reliability of these early lasers was very eratic with useful lifetimes ranging from minutes to perhaps a few hundred hours at best.

The practical realization of optical communications was made possible by two breakthroughs which occured independently. Firstly, the advent of the GaAs/AlAs heterojunction in 1969, [21], which led to an order of magnitude reduction in the lasers threshold currents. This was sufficient to permit continuous wave operation at

room temperatures and also allowed the lasers to be modulated at rates in excess of one gigahertz, [22]. Secondly, and perhaps more importantly was the production of low loss optical fibres in 1970, [23]. These fibres had attenuations of about 20dB/km in the spectral emission region of the GaAs laser.

Prior to these discoveries the reliability problem which plagued early semicoductor lasers had recieved a great deal of attention, resulting in the identification of two major failure mechanisms. These were facet damage, which was shown to be related to the optical flux density, [24], and internal defect formation, which was found to be dependent on the initial defects present in the device and also on the operating current density, [25]. Facet coatings, [26], such as Al_2O_3 have alleviated the problems of facet damage considerably. Gradual degradation was not so easily combatted and has only been reduced by exercising extreme care and attention to the growth of epitaxial material and the fabrication of the diodes, in order to prevent process induced defects and built in strains in the structure. These efforts have led to GaAS laser diodes with mean time to failure values estimated to be in excess of 10^6 hours at room temperature.

Laser diodes have by no means cornered the whole market as the light source for optical fibre communications. Competition comes from the light emitting diode, LED, which at first glance may appear less attractive than the laser due to its relatively wide spectra, one or two orders of magnitude larger than the laser diode, and much lower coupling efficiency into low numerical apperture fibres. The LED does however have some advantages over the laser, namely, better linearity in the light/current curves, less sensitivity to gradual degradation, and the output power is less subject to temperature

variations. Hence LEDs do tend to be preferred to laser diodes for systems with modest bandwidth requirements and shorter fibre link distances. There are two basic types of LEDs in use, the surface emitter, [27], and the edge emitter, [7]. Both the LED and the laser share a common technology and the progress made in improving laser reliability has also had a favourable impact on the lifetime of LEDs.

There is also another competitor to laser diodes in optical communication systems, the superluminescent diode (SLD). The SLD has a very similar structure to the laser diode except that its optical feedback is removed preventing laser action. Kurbatov, [6], inadvertantly produced the first SLD in an attempt to increase the available output from a laser diode before facet damage produced catastrophic failure. His idea was to reduce the concentration of emission at a point on the facet by positioning the stripe contact at an angle to the facets thus eliminating optical feedback. This investigation was undertaken using homostructure diodes at liquid nitrogen temperatures and bares little resemblence to the double heterostructure SLD proposed by Lee et al in 1973, [1]. Lee's SLD has a very similar structure to the stripe contact laser diode the only difference being that the stripe contact terminates well before the rear facet. This provides an unpumped region which absorbs the optical radiation and surpresses the feedback necessary for laser action. The properties of the SLD lie midway between those of the laser and the LED. Boeck and Amann, [28], demonstrated that the small signal modulation capacity of SLDs could be extended up to 1GHz before cutoff. LEDs typically operate at much lower bandwidths than this, being limited by a reduction in output power associated with high modulation rates, [29]. This, together with a significantly narrower spectral width and a smaller beamwidth than the LED make the

SLD a useful component in optical fibre systems. The interest generated by the SLD has lead to a number of computer models to be developed, [30,31,32].

The advances made in manufacturing low loss optical fibres have introduced the need to extend the technology of optical sources to longer wavelengths where the attenuation is lowest. The technique of modified chemical vapour deposition has been used to produce silica based glass fibres with losses as low as 0.47dB/km at 1.3μ, [33], and 0.2dB/km at 1.55μ, [34]. This has resulted in the production of good quality lasers and SLDs constructed from the quaternary material, InGaAsP , grown on InP substrates.

1.4 Object of this thesis.

The main object of this thesis is to investigate the properties of the superluminescent diode. This is achieved by:-

1) Measuring the light/current characteristics, spectral distribution, far-intensity 'angular' pattern and polarisation effects of a number of SLDs.

2) Developing a compehensive theoretical model of the SLD.

3) Comparing the experimental and theoretical results.

4) Using the theoretical model to achieve an understanding of the internal workings of the SLD and to suggest ways to improve it's output characteristics.

1.5 Outline of this thesis.

To predict the spectral properties of an SLD it is necessary to have an accurate representation of the stimulated and spontaneous emission distributions with both wavelength and carrier density. The stimulated and spontaneous emission distributions are

derived from the basic semiconductor bandstructure in chapter 2. The analysis begins by considering transitions between a single energy level in each of the conduction and valence bands. This is then extended to the semiconductor bandstructure as a whole by incorporating all of the energy levels in the form of the electron density of states. The difference between the stimulated and spontaneous emission properties of undoped and heavily doped semiconductors is discussed in detail. Particular attention is given to the 'bandtails' that occur in the density of states functions and the different k-selection rules displayed in the transition probability. The 'gain model' used to obtain the spontaneous and stimulated emission curves used in the SLD model is described and a number of results presented and discussed.

The propogation of the optical fields in the active layer of the double heterostructure are described in chapter 3. In the direction perpendicular to the plane of the junction the optical fields spread significantly into the surrounding layers. This means that only part of the optical field can interact with the injected carriers that are almost totally confined to the active layer. It is therefore of particular importance to calculate the fraction of the optical fields remaining in the active region; this fraction is referred to as the confinement factor. The SLD emits partially polarised light so that it is necessary to calculate both the TE and TM confinement factors. This is done by treating the double heterostructure as a symmetrical dielectric slab waveguide. A general discussion is also given of the waveguiding in the lateral direction. This is more complicated since two mechanisms, an antiguiding effect and a guiding effect, due to the optical gain, both produced by the injected carrier profile, compete with each

other to result in net guiding.

The SLD model, [35], is formulated in chapter 4 in such a way that it yields results for the light/current characteristics, spectral distribution, far-intensity angular distribution and polarisation characteristics. The equations that provide the basis of this model are obtained by enforcing the physical requirements of photon and charge conservation within the active layer of the double heterostructure. The model assumes a waveguide modal intensity pattern in the direction perpendicular to the plane of the junction and scalar plane wave (ray optics) propogation in the plane of the junction. The photon conservation equations are solved subject to the boundary conditions provided by the reflectivities at each end of the device. The procedure is highly non-linear because the photon density depends on the optical gain it experiences along the length of the device which in turn depends on the photon density.

A description of the experimental techniques used to measure the SLD's light/current characteristics, spectral distribution and far-intensity angular distribution is given in chapter 5. Measurements on several SLDs made from two seperate semiconductor wafers. A comparison is made with the computed results obtained from the theoretical model of the SLD described in chapter 4.

The theoretical model of the SLD is used to describe, and explain, the SLD's output characteristics in chapter 6. This is done by tracing the growth and decay of the forward and reverse travelling photon fluxes along the length of the device. In discussing the SLDs spectral characteristics the wavelength dependence of gain saturation recieves special attention. A number of methods for increasing the SLDs output power are investigated.

The polarisation characteristics of the SLD are investigated in chapter 7. The techniques used for measuring the polarisation dependent light/current characteristics and their spectral dependence are described in detail. A comparison is made with the theoretical predictions of the SLD model developed in chapter 4.

References.

1) 'A stripe-geometry double-heterostructure amplified-spontaneous-emission (superluminescent) diode', T.P.Lee, C.A.Burrus.Jr., and B.I.Miller, IEEE J. of Quant. Electron., vol.QE-9, p.820, 1973.

2) 'Dynamics of injection lasers', N.G.Basov, IEEE J. of Quant. Electron., vol.QE-4, p855.

3) 'The effect of photon lifetime on absorbtive bistability in inhomogeneously pumped lasers'. M.C.Perkins, R.F.Ormondroyd and T.E.Rozzi, Electron. Letts., vol.21, p.857, 1985.

4) 'Bistability and pulsations in semiconductor lasers with inhomogeneous current injection', C.Harder, K.Y.Lau and A.Yariv, IEEE J. of Quant. Electron., vol.QE-18, p.1351, 1982.

5) 'High-power low-divergence superradiance diode', C.S.Wang, W.H.Cheng, and C.J.Hwang, Appl. Phys. Lett., vol.41, p.587, 1982.

6) 'Lateral confinement InGaAsP superluminescent diode at 1.3μ', I.P.Kaminow, G.Eisenstein, L.W.Stutz and P.P.Dentai, IEEE J. of Quant. Electron., vol.QE-19, p.78, 1983.

7) 'Investigation of superluminescence emitted by a gallium arsenide diode', L.N.Kurbatov, S.S.Shakhidihanov, L.V.Bystrova, V.V.Krapukhin, and S.I.Kolovenkova, Sov. Phys. semicon., vol.4, p.1739, 1971.

8) ' Measurement of modal reflectivity of an antireflection coating on a superluminescent diode', I.P.Kaminow, G.Eisenstein and L.W.Stutz, IEEE J. Quant. Electron., vol.QE-19, p.493, 1983.

9) 'Computer simulation of Fabry-Perot laser amplifiers, I.Middlemast and J.Sarma, 'SILA' conference, Cardiff, 1984.

10) 'Stimulated optical radiation in ruby lasers', T.H.Maiman, Nature, vol.187, p.493, 1960.

11) 'Stimulated infrared emission from trivalent uranium', P.P.Sorokin and M.J.Stevenson, Phys.Rev.Lett. vol.5, p.577, 1960.

12) 'Population inversion in continuous optical maser oscillation in a gas discharge containing a He-Ne mixture', A.Javan, W.B.Bennet.Jr, and D.R.Herriot, Phys. Rev. Lett., vol.6, p.106, 1961.

13) J.I.Nishizanar and Y.Watanabe, Japanese patent, April 1957. Also Electronics, p.117, December 1961.

14) N.G.Basov, B.M.Vul and Y.M.Popov, Sov.Phys, JETP.13, p.1320,1961.

15) P.Agrain (1958), reported in Proc.Conf.Quantum Electronics, Paris, 1963, p.1762.

16) 'Laser conditions in semiconductors', M.G.A.Bernard and G.Duraffourg, Phys.Status Solidi, vol.1, p.699, 1961.

17) ' Interband transitions and maser action', W.P.Dumke, Phys.Rev. vol.127, p.1559, 1962.

18) 'Coherent light emission from GaAs junctions', R.N.Hall, G.E.Fenner, J.D.Kingsley, T.J.Soltys and R.O.Carlson, Phys. Rev. Lett., vol.9, p.366, 1962.

19) 'Stimulated emission of radiation from GaAs p-n junction', M.I.Nathan, W.P.Dumke, G.Burns, P.H.Dill.Jr and G.J.Lasher, Appl. Phys. Lett., vol.1, p.62, 1962.

20) 'Semiconductor Maser of GaAs', T.M.Quist, R.H.Rediker, R.J.Keyes, W.E.Krag, B.Lax, A.L.Whorter and H.J.Zeigler, Appl. Phys. Lett., vol.1, p.91, 1962.

21) 'Injection properties of n-$Al_xGa_{1-x}As$-p-GaAs Heterojunctions', Z.I.Alferov, V.M>Andreev, V.I.Korol'kov, E.L.Portnoi and D.N.Tretyakov, Sov. Phys. Semicond., vol.2, p.843, 1969.

22) Heterostructure Injection Lasers', M.P.Panish, Proc.IEEE vol.64, p.1512, 1976.

23) 'Radiation Losses in glass optical waveguides', F.P.Kapron, D.B.Keck and R.D.Mavrer, Appl. Phys .Lett., vol.17, p.423, 1970.

24) H.Kressel and H.P.Microp, J. Appl. Phys., vol.38, p5419, 1967.

25) H.Kressel and N.E.Byer, Proc. IEEE, vol.38, p.25, 1969.

26) 'Al_2O_3 half-wave films for long-life cw lasers', I.Ladany, M.Ettenberg, H.F.Lockwood and H.Kressel, Appl. Phys. Lett., vol.30, p.87, 1977.

27) 'Small-area dh Al-Ga-As electroluminescent diode sources for optical fibre transmission lines', C.A.Burrus and B.I.Miller, Opt. commun., vol.4, p.307, 1971.

28) 'Modulation characteristics of double-heterostructure superluminescent diodes', M.C.Amann and W.Harth, Electron. Lett., vol.13, p.291, 1977.

29) 'Semiconductor lasers and heterojunction LEDs', H.Kressel and J.K.Butler, Academic Press, 1977.

30) 'On the theory of the superluminescent diode, 1. Stationary behavior', J.Boeck, M.C. Amann and B.Stegmuller.

31) 'On the theory of the superluminescent diode, 2. Small signal modulation', J.Boeck, M.C. Amann and B.Stegmuller.

32) 'Computer model of a superluminescent LED with lateral confinement', D.Marcuse and I.P.Kaminow, IEEE. J. of Quant. Electron., vol.QE-17, p.1234, 1981.

33) ' Spectral losses of low-OH-content optical fibres', M.Horiguchi and H.Osanai, Electron. Lett., vol.12, p.310, 1976.

34) 'Ultimate low-loss single-mode fibre at 1.55μ', T.Miya, Y.Teronuma, T.Hosaka, and T.Miyashita., Electron. Lett., vol.15, p.106, 1979.

35) 'A comprehensive study and characterisation of superluminescent light emitting diodes', I.Middlemast, J.Sarma and T.Kambayashi, presented at the IEEE specialist conference on light emitting diodes and photodetectors, Ottawa, Canada, 1982.

CHAPTER 2

LIGHT EMISSION PROCESSES IN SLDS AND LASERS

2.1 Introduction

In developing a model of an active waveguide such as the SLD it is essential to incorporate the local gain (stimulated emission) and spontaneous emission as functions of wavelength and inversion population if any useful spectral information is to be obtained. It has become common practice amongst laser researchers to represent the stimulated and spontaneous emission distributions by using Laurentian or parabolic distributions, [1-4], which can be written in simple analytic forms that lend themselves easily to computer modelling. These analytic forms however are only accurate over a small region near their peaks and they require an expression to take into account the movement of the peak with inversion population. This is adequate for a laser because it has a very narrow spectral line-width and its inversion population is very nearly constant with length and varies only slightly with current above threshold. An SLD however has a much broader spectrum and the inversion population varies considerably with both length and current making these analytic approximations quite inaccurate. It is therefore necessary to use more realistic stimulated and spontaneous emission distributions such as those that can be derived from the basic semiconductor band structure. Much work has been undertaken in this area, primarily by Stern, [5-9], although other models have been developed, [10,11].

In this chapter the approach used by Stern, which is well

documented in the books by Thompson, [12], and Casey and Panish, [13], is followed. The analysis begins in section (2.2) by considering transitions between a single energy level in each of the conduction and valence bands, thus reducing the problem to a simple two energy level system. This allows the relationships between absorption, stimulated emission and spontaneous emission to be expressed in terms of the Einstein coefficients. The transition probability is then discussed in section (2.3) paying particular attention to 'k-selection'. In section(2.4) the analysis is extended to the semiconductor bandstructure as a whole by incorporating all of the energy levels in the form of the electron density of states. In section (2.5) the bandtails that occur in the electron density of states when semiconductors are highly doped are considered. Finally, a description of the model used to produce the stimulated and spontaneous emission distributions used througout this project is given in section (2.6). The model is developed in such a way that the magnitude and spectral shape can be altered by changing two parameters, the bimolecular recombination coefficient and the Kane bandtailing parameter. The effect of altering these parameters is described in detail. No comparison is made with other models because this model is developed with the sole purpose of being flexible enough to use for reproducing the spectral characteristics of SLDs rather than to further the already existing theory of light emission processes. Some concluding remarks are made in section (2.7).

2.2 Transitions in a two energy level system.

2.21 The Einstein relations.

Instead of the two sharp energy levels that an atomic system posesses the available electron states in semiconductors are represented by a continuous band of states within the valence and conduction bands. For the purpose of deriving the Einstein cofficients consider a transition from a state E_1 within the valence band to a state E_2 within the conduction band, fig(2.1), resulting from the absorbtion of a photon of energy $E_2-E_1 = E_{21}$. The rate of this process depends on several factors;

1) the probability that the transition can occur, B_{12};

2) the probability that the state E_1 contains an electron, f_1;

3) the probability that the state E_2 is empty, $(1-f_2)$;

4) the density of photons of energy E_{21}, $P(E_{21})$.

The upward transition rate (r_{12}) corresponding to absorption may then be written as

$$r_{12} = B_{12}f_1(1 - f_2)P(E_{21}) \qquad (2.1)$$

where the occupation probability of E_1 is given by the Fermi-Dirac distribution for indistinguishable, identical particles with half-integral spin that obey the Pauli exclusion principle. Hence

$$f_1 = (\exp[(E_1 - F_1)/kT] + 1)^{-1} \qquad (2.2)$$

where F_1 is the quasi-Fermi level for the valence band at non-equilibrium, k is the Boltzman constant and T is the temperature. Similarly, for the conduction band,

$$f_2 = (\exp[(E_2 - F_2)/kT] + 1)^{-1} \qquad (2.3)$$

where F_2 is the quasi-Fermi level for the conduction band.

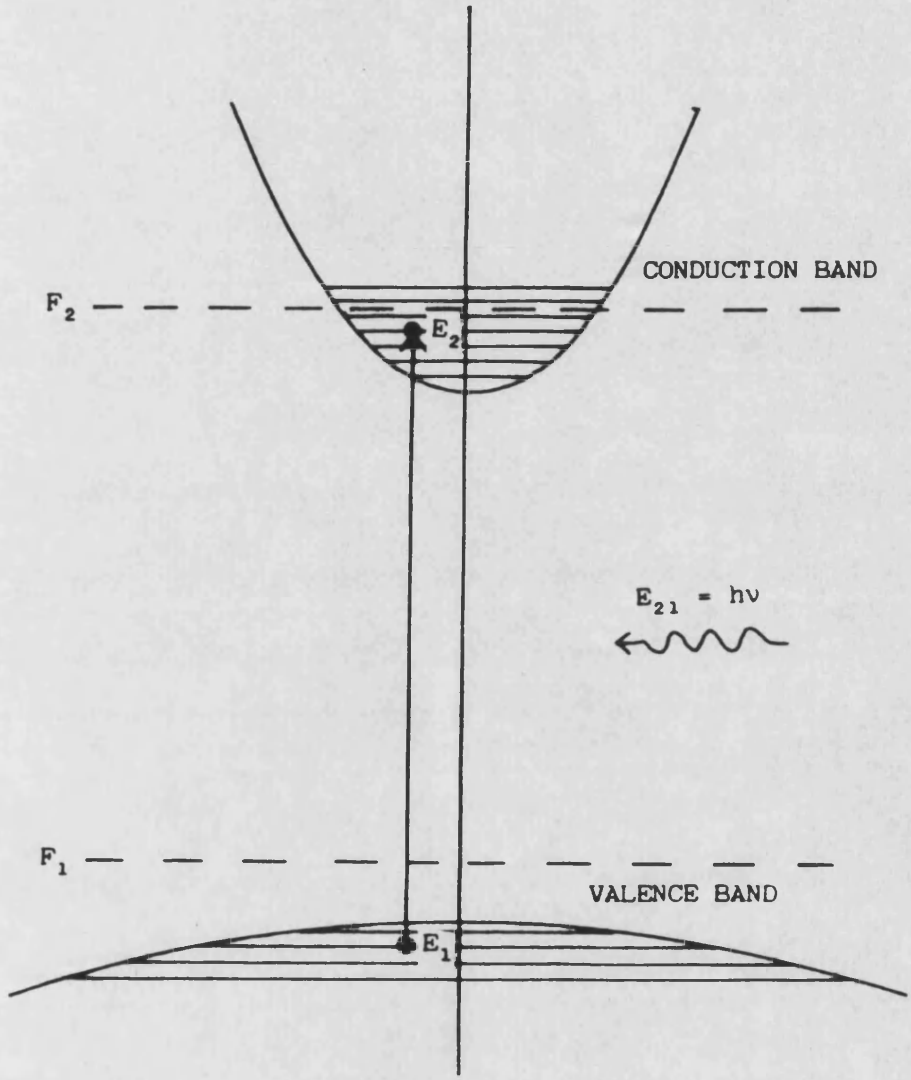

Fig(2.1) Transition of an electron from a state E_1 in the valence band to a state E_2 in the conduction band by the absorption of a photon of energy E_{21}. The quasi-fermi levels for the valence and conduction bands are represented by F_1 and F_2 respectively.

In addition to being absorbed, photons can stimulate the emission of a similar photon by the transition of an electron from the state E_2 to E_1. The downward transition rate for stimulated emission is

$$r_{21} = B_{21} f_2 (1 - f_1) P(E_{21}) \qquad (2.4)$$

where B_{21} is the transition probability, f_2 is the probability that the state E_2 is occupied and $(1-f_1)$ the probability that the state E_1 is empty.

Electrons in the state E_2 can also spontaneously return to the state E_1 without any interaction with a photon. The probability for this process is represented by A_{21} and the spontaneous emission rate is given by

$$r_{21}(spon) = A_{21} f_2 (1 - f_1) \qquad (2.5)$$

In thermal equilibrium the upward transition rate must equal the total downward transition rate,i.e

$$r_{12} = r_{21} + r_{21}(spon) \qquad (2.6)$$

and $F_1 = F_2$. On substituting equations (2.1), (2.4), and (2.5) into equation (2.6) one obtains

$$P_{21}(E) = \frac{A_{21} f_2 (1 - f_1)}{B_{12} f_1 (1 - f_2) - B_{21} f_2 (1 - f_1)} \qquad (2.7)$$

and this may be equated with the thermal photon density of energy E_{21} which is given in [12] as

$$P(E) = \frac{(8\pi/(hc)^3) n^{2\wedge} n E^2}{\exp(E/kT) - 1} = \frac{Z(E)}{\exp(E/kT) - 1} \qquad (2.8)$$

where h is Plank's constant, c is the velocity of light in free space, η is the refractive index and $\hat{\eta}$ is a group refractive index that takes account of dispersion. It then follows that

$$\frac{Z_{21}(E)}{\exp(E_{21}/kT) - 1} = \frac{A_{21}}{B_{12}\exp(E_{21}/kT) - B_{21}} \qquad (2.9)$$

which may be rewritten as

$$Z(E_{21})(B_{12}\exp(E_{21}/kT) - B_{21}) = A_{21}\exp(E_{21}/kT) - A_{21} \qquad (2.10)$$

and can then be seperated into it's temperature dependent and temperature independent terms. Equating the temperature dependent terms gives

$$Z(E_{21})B_{12}\exp(E_{21}/kT) = A_{21}\exp(E_{21}/kT) \qquad (2.11)$$

i.e,

$$A_{21} = Z(E_{21})B_{12} \qquad (2.12)$$

and equating the temperature independent terms gives

$$A_{21} = Z(E_{21})B_{21} \qquad (2.13)$$

Therefore it follows that $B_{21} = B_{12}$. Equations (2.12) and (2.13) are the Einstein relations and show that the spontaneous emission probability is related to the absorbtion and the stimulated emission probabilities.

2.22 Necessary condition for stimulated emission.

It is instructive to consider what conditions are necessary for the stimulated emission to be in excess of the absorbtion. There is in fact only one necessary condition and this was first expressed by Bernhard and Duraffourg [14]. It requires that a photon is more

likely to cause a downward transition of an electron from the conduction band to the valence band with the emission of a photon than the upward transition from the valence band to the conduction band with the absorbtion of a photon. In other words this implies that $r_{21} > r_{12}$; i.e,

$$B_{21}f_2(1 - f_1).P(E_{21}) > B_{12}f_1(1 - f_2)P(E_{21}) \qquad (2.14)$$

and as $B_{21} = B_{12}$ this reduces to

$$f_2(1 - f_1) > f_1(1 - f_2) \qquad (2.15)$$

On substitution of equations (2.2) and (2.3) into equation (2.15) the simple condition

$$F_2 - F_1 > E_2 - E_1 \qquad (2.16)$$

is obtained. Therefore the condition for net positive stimulated emission is that the seperation of the quasi-Fermi levels must exceed the photon emission energy.

2.23 The net stimulated emission rate and it's relation to the spontaneous emission rate.

A frequently used quantity is the net stimulated emission rate, $r_{21}(stim)$, which is defined as the difference between the downward transition rate, (r_{21}), and the upward transition rate, (r_{12}). Using equations (2.1) and (2.4) and the fact that $B_{21} = B_{12}$ $r_{21}(stim)$ may be expressed as

$$r_{21}(stim) = P(E_{21})B_{21}(f_2 - f_1) \qquad (2.17)$$

The spontaneous emission rate can be obtained from equations (2.5) and (2.13) and may be written as

$$r_{21}(spon) = Z(E_{21})B_{21}f_2(1 - f_1) \qquad (2.18)$$

The form of equations (2.17) and (2.18) are very similar and it is convenient to introduce two new terms

$$W_{stim}(E_{21}) = B_{21}(f_2 - f_1) \qquad (2.19)$$

and

$$W_{spon}(E_{21}) = B_{21}f_2(1 - f_1) \qquad (2.20)$$

so that the net stimulated emission and spontaneous emission rates become

$$r_{21}(stim) = P(E_{21})W_{stim}(E_{21}) \qquad (2.21)$$

and

$$r_{21}(spon) = Z(E_{21})W_{spon}(E_{21}) \qquad (2.22)$$

respectively. These expressions for $W_{stim}(E_{21})$ and $W_{spon}(E_{21})$ produce a direct relationship between the stimulated and spontaneous emission rates when they are combined together with equations (2.2) and (2.3), i.e.

$$W_{stim}(E_{21}) = W_{spon}(E_{21})(1 - \exp[\{E_{21} - (F_2 - F_1)\}/kT] \qquad (2.23)$$

Because $W_{spon}(E_{21})$ is always positive equation (2.23) is an altenative way of expressing the Bernard and Duraffourg condition, equation (2.16), showing that there is only net positive stimulated emission when $F_2-F_1 > E_{21}$. Another interesting point arising from equation (2.23) occurs when $F_2-F_1 >> E_{21}$ and it reduces to $W_{stim}(E_{21}) = W_{spon}(E_{21})$. This means that at high pumping levels the spontaneous emission rate is equal to the stimulated emission rate that would occur with one photon per mode.

2.24 The absorbtion coefficient and it's relation to the local gain.

The interaction of photons and electrons in a semiconductor may be related to a macroscopic property, the absorption coefficient, α. The net absorption rate, $r_{12}(abs)$, is defined as the difference between the upward and downward transition rates and from equations (2.1) and (2.4) may be written as

$$r_{12}(abs) = B_{21}(f_1 - f_2)P(E_{21}) = - W_{stim}(E_{21})P(E_{21}) \quad (2.24)$$

The net absorption rate is in fact the absorption probability, $B_{21}(f_1 - f_2)$, multiplied by the photon flux, $Q(E_{21})$, which is given by

$$Q(E_{21}) = P(E_{21}).v_g \quad (2.25)$$

where v_g is the group velocity of light in the dielectric medium. Since

$$v_g = \frac{\delta\omega}{\delta k} \quad (2.26)$$

where k is the propagation constant or wavevector given by $k = 2\pi/\lambda$, $\omega = 2\pi E/h$ and $\delta k = 2\pi.\frac{(n + E.\delta n/\delta E).\delta E}{hc}$ it follows that

$$v_g = \frac{2\pi.\delta E}{h\ \delta k} = \frac{c/n}{1 + (E/n)(\delta n/\delta E)} \quad (2.27)$$

Taking the dispersive term $1 + (E/n)(\delta n/\delta E)$ to be unity allows the absorption coefficient to be written as

$$\alpha(E_{21}) = -n/c.W_{stim}(E_{21}) \quad (2.28)$$

Another commonly used term in semiconductor laser work is the local gain, $g(E_{21})$, which is defined as $-\alpha(E_{21})$ and is therefore written as

$$g(E_{21}) = n/c.W_{stim}(E_{21}) \qquad (2.29)$$

It is the local gain which when modified by the appropriate confinement factor gives the 'modal gain' commonly referred to in semiconductor laser literature.

2.3 The transition probability.

The transition probability, B_{21}, used in equations (2.1) and (2.4) for the stimulated and spontaneous emission rates, is the basic quantity that determines the transition rates of electrons between the conduction and valence bands. Consideration of the interaction between electrons in the semiconductor and electromagnetic radiation requires the techniques of time dependent perturbation theory, [3]. Using this procedure the properties of the system are determined in the absence of radiation and then the alteration that occurs when radiation is present is calculated. Rather than go through the straightforward but rather lengthy derivation of the transition probability the well known result known as Fermi's Golden rule, [3], is stated

$$B_{21} = \pi/2h \; |\langle \Psi_1^*(\underline{r},t)|\, H' |\Psi_2(\underline{r},t)\rangle|^2 \qquad (2.30)$$

where $\underline{r}$ is the three dimensional spatial vector; $\Psi_1^*(\underline{r},t)$, is the complex conjugate of the wave function of the initial state; H', is the interaction Hamiltonian operator and $\Psi_2(\underline{r},t)$ is the wave function of the final state. The quantity $|\langle \Psi_1^*(\underline{r},t)|\, H' |\Psi_2(\underline{r},t)\rangle|$ is commonly called the matrix element of the interaction Hamiltonian between the initial and final states and is given by

$$|\langle \Psi_1^*(\underline{r},t)|\, H' |\Psi_2(\underline{r},t)\rangle| = \int_V \Psi_1^*(\underline{r},t) H' \Psi_2(\underline{r},t) \delta^3\underline{r} \qquad (2.31)$$

where V is the volume $= \delta^3\underline{r}$, and on reduction of the Hamiltonian

operator to the momentum operator, p, in the matrix element the transition probability becomes

$$B_{21} = \frac{q^2 h}{2m^2 \varepsilon_0 n^2 h\nu} \cdot |M|^2 \qquad (2.32)$$

where the momentum matrix element, M, is given by

$$M = |\langle \Psi_1^*(\underline{r})|\underline{p}|\Psi_2(r) \rangle| = \int_V \Psi_1^*(\underline{r})\underline{p}\Psi_2(\underline{r})\delta^3 \underline{r} \qquad (2.33)$$

Before proceeding it is worth commenting on k-selection. The conventional theory for optical transitions between the valence and conduction bands of direct energy gap semiconductors is based on the so called 'k-selection rules'. This expresses the condition that the wave vector, k_1, of the valence band and the wave vector, k_2, of the conduction band must differ by the wave vector of the photon, k, otherwise the matrix element is zero. That is the matrix element contains a delta function $\delta(k_2-k_1\pm k)$. Since p=h.k , $\delta(k_2-k_1\pm k)$ is simply an expression for the conservation of momentum of the transition. It should be noted that because the wavevector of the photon is very much smaller than that of the electron it is generally considered to be negligable so that the k-selection rule becomes $k_1 \cong k_2$. The allowed transitions are then between initial and final states of the same wavevector and are known as direct or vertical transitions. Transitions where the wavevectors are not the same must involve a phonon so that momentum is conserved. This makes the transition much less probable and explains the reason why direct bandgap semiconductors such as GaAs and InP lase and indirect bandgap materials such as AlAs and AlP do not.

General solutions of the wave equation show that in a periodic potential, such as that arising from the lattice structure,

the wavefunctions may be represented by Bloch functions. In this case the band to band matrix element, M_{bb}, obtained by averaging over all directions in space, is approximately given by [16]

$$|M_{bb}|^2 \cong \frac{m^2 E_g}{3m_c} \frac{1 + \Delta/E_g}{1 + 2/3\ \Delta/E_g} (1 - m_c/m) \qquad (2.34)$$

where m is the free electron mass, m_c is the effective mass of an electron in the conduction band, E_g is the bandgap, and Δ is the spin-orbit splitting. Inserting this into equation (2.32) for the transition probability and taking $h\nu = E_g$ gives

$$B_{21} = \frac{q^2 h}{6m_c \varepsilon_0 n^2} \frac{1 + \Delta/E_g}{1 + 2/3\ \Delta/E_g} (1 - m_c/m) \qquad (2.35)$$

In the following section the transition probability is written as a function of the initial and final energy states, $B(E_1,E_2)$. This is due to the fact that when impurities or defects are present the wavefunctions and matrix elements are modified somewhat. For low impurity concentrations the wavefunction of the lowest bound state associated with a shallow impurity level is a superposition of wavefunctions of states near the adjacent band edge. The average matrix element between this state and a state across the energy gap has a magnitude given by the hydrogenic model, [17], as

$$|M_{av}|^2 = \frac{64\pi a_*^3}{(1 + a_*^2 k_v^2)^4 V} |M_{bb}|^2 \qquad (2.36)$$

a_* is the effective Bohr radius and is given by

$$a_* = \frac{\varepsilon m a_0}{m_{eff}} = \frac{\varepsilon h^2}{m_{eff} q^2} \qquad (2.37)$$

and k_v is the wavevector of a hole state in the valence band, ε is the dielectric constant of the material and m_{eff} is the effective mass of an electron at the band edge perturbed by the impurity. Equation (2.6) may also be written as

$$|M_{av}|^2 = |M_{env}|^2 . |M_{bb}| \qquad (2.38)$$

where the modification to the band to band matrix element is considered to be an envelope matrix element, M_{env}. Fig (2.2) shows how the probability of a transition of a carrier in an impurity state near the band edge to a free carrier in the opposite band varies with the wavevector.

As the doping density is increased the spacing between orbitals of the neighbouring atoms decreases and the orbitals of the neighbouring bound carriers start to overlap. The potential wells of the individual impurities merge together and the carriers can no longer be described by simple hydrogenic wavefunctions. At a certain impurity concentration the distinction between bound and free carriers becomes vague and they broaden and merge with the adjacent band edge. The effect of such high impurity concentrations can be approximated by a rigid shift of the band edge towards the centre of the bandgap with some change in the effective mass, [18], and by a tail extending into the forbidden region which arises from the random impurity distribution, [19]. States deep in the tail arise from interactions with two or more impurity ions in a cluster. They will have appreciable matrix elements with states in the opposite band over a wider range of energy than does a simple hydrogenic level whose matrix element is given by equation (2.36). In this region the k-selection rules are relaxed. The further into the band a state is the less the perturbation of the wavefunction by the impurities. For

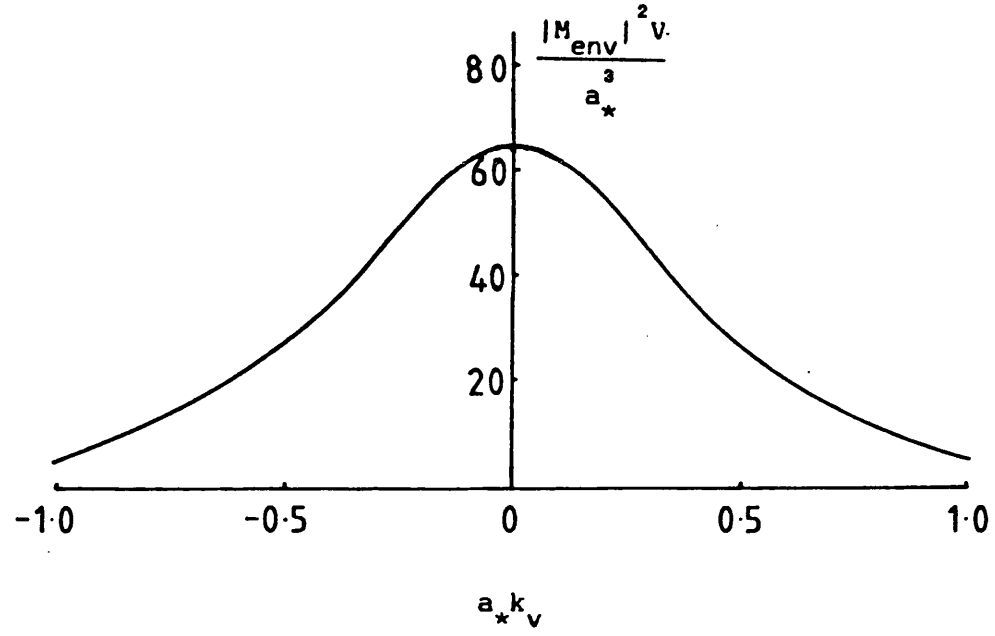

Fig(2.2) Probability of a radiative recombination between a carrier bound to an impurity and a free carrier in the opposite band as a function of the product of the wave vector k_v of the free carrier and the Bohr radius a_* of the bound state. The probability is given in terms of an envelope matrix. [12].

states well inside the band k-selection rules will again apply. Stern, [7], has made a theoretical analysis of the transition probabilities in heavily doped semiconductors using 'ad hoc' wavefunctions to represent the semi-localised electronic states. The results can be expressed in the same way as for the single bound carrier as the product of an envelope matrix element, M_{env}, with the band to band matrix element, M_{bb}. The expression for the envelope function used by Stern is somewhat over complicated and no further reference of it will be made here, the reader being referred to [6,7].

2.4 The extension of the two energy level system to the full semiconductor band system.

So far the absorption and emission rates considered in this chapter represent transitions that occur between discrete pairs of energy levels, seperated by energy, E_{21}, within the semiconductor band system. This analysis is now extended to include the various states that exist in the valence and conduction bands of the semiconductor. This is achieved by making the single-electron approximation in which each transition is considered as the change of state of a single electron. Then the density of single-electron states per unit energy describes the continuum of states in the conduction and valence bands. The spontaneous and stimulated emission rates are then obtained by summing over all possible transitions.

The density of single-electron states per unit energy for the conduction band ,ρ_c, is given by the parabolic expression, [20]

$$\rho_c = \frac{m_c(2m_cE_c)^{1/2}}{\pi^2h^3} \qquad (2.39)$$

where the energy of the electron, E_c, is

$$E_c = \frac{h^2 k^2}{2m_c} \tag{2.40}$$

with respect to the bottom of the conduction band, fig(2.1),and m_c is the effective mass of the electron in the conduction band. A similar expression is obtained for the density of states, ρ_v, in the valence band.

$$\rho_v = \frac{m_v[2m_v(-E_g - E_v)]^{1/2}}{\pi^2 h^3} \tag{2.41}$$

where the energy of the hole, E_v, is given by

$$-(E_v + E_g) = \frac{h^2 k^2}{2m_c} \tag{2.42}$$

and is measured with respect to the same zero. E_g is the bandgap and m_v is the effective mass of the hole in the valence band.

When considering transitions over a large number of states in the conduction and valence bands the transition probability is dependant on the degree of k-selection involved. Strong k-selection limits the number of states that participate in transitions and it is necessary to consider the conduction and valence band density of states simultaneously. This is achieved by using a reduced density of states of the form [12]

$$\rho_{red}(E) = \frac{1}{2}\left[\frac{1}{\rho_c} + \frac{1}{\rho_v}\right]^{-1} \tag{2.43}$$

Using this expression the upward transition rate, equation (2.1) becomes

$$r_{12} = B_{12} f_v (1 - f_c) \rho_{red}(E) P(E) \tag{2.44}$$

and the downward transition rate,equation (2.4), becomes

$$r_{21} = B_{21} f_c (1 - f_v) \rho_{red}(E) P(E) \qquad (2.45)$$

The spontaneous transition rate, equation (2.6) can also be rewritten as

$$r_{21}(spon) = B_{21} f_c (1 - f_v) \rho_{red}(E) Z(E) \qquad (2.46)$$

The transition probability per unit spread of energy in the conduction band and for volume, V, can be expressed as $B(E_c,E).\rho_c(E_c).V$. Note that the transition probability, $B(E_c,E)$, is dependent on the initial and final energy values and normally includes a V^{-1} term so that the volume terms cancel.

The net rate of stimulated transitions at photon energy, E, is obtained by integrating over E_c the difference between downward and upward transitions and is given by

$$R_{stim}(E) = P(E) \int_{-\infty}^{\infty} B(E_c,E) V \rho_c(E_c) \rho_v(E_c - E) . \cdot (f_c - f_v)(1 + \rho_v/\rho_c)^{-1} \delta E_c \qquad (2.47)$$

A similar expression for the spontaneous transition rate can also be obtained

$$R_{spon}(E) = Z(E) \int_{-\infty}^{\infty} B_{12}(E_c,E) V \rho_c(E_c) \rho_v(E_c - E) . \cdot f_c (1 - f_v)(1 + \rho_v/\rho_c)^{-1} \delta E_c \qquad (2.48)$$

It is now worth considering what happens to the spontaneous and stimulated emission rates when k-selection rules do not apply. Under these conditions it is possible to integrate over the conduction and valence bands independently and the spontaneous and stimulated emission rates may be written as

$$R_{spon}(E) = Z(E) \int_{-\infty}^{\infty} B(E_c,E)V\rho_c(E_c)\rho_v(E_c - E)f_c(1 - f_v)\delta E_c \quad (2.49)$$

and

$$R_{stim}(E) = P(E) \int_{-\infty}^{\infty} B(E_c,E)V\rho_c(E_c)\rho_v(E_c - E)(f_c - f_v)\delta E_c \quad (2.50)$$

respectively. The total spontaneous emission is obtained by integrating equation (2.49) over the full energy range with respect to E,

$$R_{spon}(total) = \int_{a}^{\infty} Z(E) \int_{-b}^{\infty} B(E_c,E)V\rho_c(E_c)\rho_v(E_c - E) .f_c(1 - f_v)\delta E_c\delta E \quad (2.51)$$

where the integration limits, a and b, are chosen so that the integrations terminate within the forbidden band. Changing the variable of integration this becomes

$$R_{spon}(total) = \int_{-\infty}^{-b-a} \int_{-b}^{\infty} Z(E_c - E_v)B(E_c,E_v)V\rho_c(E_c)\rho_v(E_v) .f_c(1 - f_v)\delta E_c\delta E_v \quad (2.52)$$

which is a particularly useful form as it contains the two composite terms $\rho_c(E_c).f_c.dE_c$ and $\rho_v(E_v)(1-f_v)dE_v$ which represent increments δn in electron concentration and δp in hole concenration respectively. Now by making the constant matrix element approximation so that $B(E_c,E_v)$ is a constant and assuming that $Z(E_c-E_v)$ is approximately constant over the limits of integration then the resulting integration gives

$$R_{spon}(total) = B_r np \quad (2.53)$$

where B_r is a constant. This is the well known result for bimolecular recombination, hence B_r is commonly referred to as the

bimolecular recombination rate.

2.5 The concentration dependent density of states.

When the doping concentrations in a semiconductor are high the density of electronic states in the conduction and valence bands are modified and the usual representation of localised impurity levels seperated from the band edges cannot be used. Instead the random distribution of charged impurities in the crystal result in potential fluctuations which produce tails on the conduction and valence band density of states. The effect of such potential fluctuations was first treated by Kane, [19]. In his analysis the carriers are assumed to have sufficiently low kinetic energy to permit them to follow fluctuations in the potential created by the ionised impurities. For Gaussian potential energy fluctuations, whose root mean square is designated V_{rms}, the conduction band density of states for an n-type semiconductor takes the form, [19]

$$\rho_c = \frac{m_c(2m_c n_c)^{1/2}}{\pi^2 \eta^3} . y(E_c/n_c) \qquad (2.55)$$

This expression has the same form as the parabolic density of states with the $(E_c^{1/2})$ term in equation (2.39) replaced by $n_c^{1/2} . y(E_c/n_c)$ where n_c is given by

$$n_c = (2)^{1/2} . V_{rms} \qquad (2.56)$$

and the Kane function, y, is

$$y(x) = \pi^{-1/2} \int_{-\infty}^{x} (x - z)^{1/2} \exp(-z^2) \delta z \qquad (2.57)$$

The variation in the Kane function with x is shown in fig (2.3).It

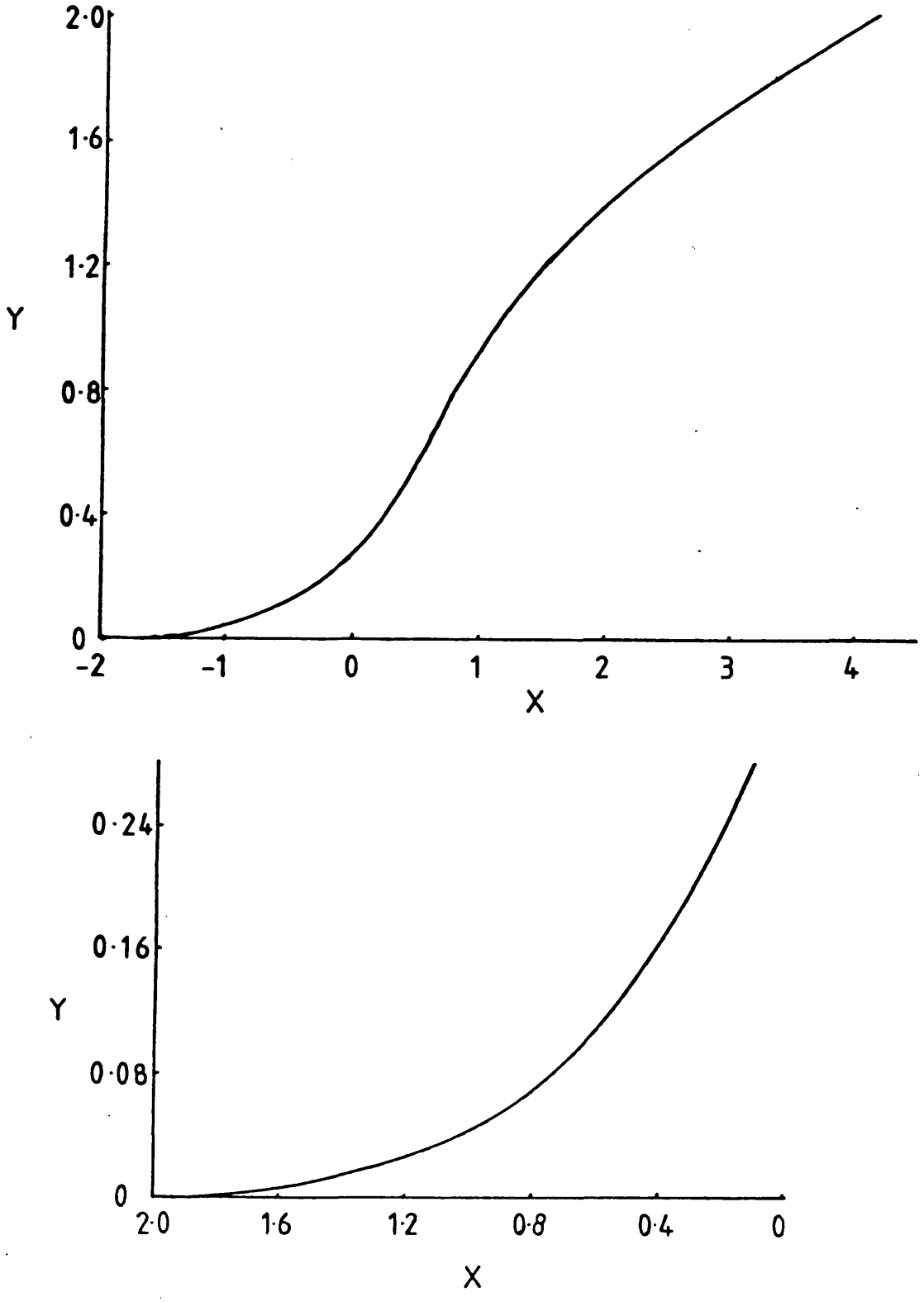

Fig(2.3) Variation of the Kane function, y, with x. [19].

can be seen that ρ_c varies as $E_c^{1/2}$ at high energies and that at low energies it approaches the Gaussian form $\exp(-E_c^2/\eta_c^2)$. The band tailing parameter, η_c, gives a convenient measure of the depth of the tail. This procedure is, of course, equally applicable to the valence band.

In the Kane model the potential fluctuations arise from the Coulomb potentials of N_d^+ ionised donors and N_a^- ionised acceptors per unit volume which are randomly distributed on the lattice sites. The root mean square voltage fluctuation, V_{rms}, that determines η_c is then given by

$$V_{rms} = \frac{q^2}{4\pi\varepsilon}.[2\pi(N_d^+ + N_a^-)L_s]^{1/2} \qquad (2.58)$$

where q is the electronic charge, ε the permittivity and L_s is the screening length given by, [24]

$$L_s = \left|\frac{q^2}{\varepsilon\varepsilon_0} \cdot \frac{\delta n}{\delta F}\right|^{1/2} \qquad (2.59)$$

where $\delta N/\delta F$ is the rate of change of the carrier concentration with the Fermi energy, F. From equation (2.59) it can be seen that L_s depends on the carrier concentration and it therefore also depends on the shape of the density of states. Consequently, it follows that a self consistent solution is necessary to determine L_s and ρ_c.

The density of states obtained by Kane overestimates the length of the tail by making no allowance for electron or hole tunnelling through potential barriers and not taking a proper account of the kinetic energy of localisation. Halperin and Lax,[21] used a 'minimum counting' technique which takes account of the kinetic energy of localisation thereby producing smaller bandtails. These results, however, were numerical and over a limited region within the

tail. Hwang, [22], compared the results of Kane and Halperin and Lax producing a model of the density of states by interpolating between the Halperin and Lax results and the parabolic band, fig (2.4). Stern, [8], uses a similar approach in his model except that he approximates the density of states of the Kane form to the Halperin and Lax results in the bandtail.

In all of these models the effective mass that is used is somewhat questionable because it appears that no theory for bandtails has taken into account the detailed structure of the energy states. Instead the bands are assumed to be isotropic and parobolic. Stern, [7], has, in one of his models attempted to account for the non-parabolicity of the conduction band by replacing the effective mass at the bottom of the band by a slightly larger value of approximately 10% or less. The light hole band's effective mass was also increased by a similar ammount.

2.6 k-selection, Kane bantail model of spontaneous and simulated emission.

There are two main features involved in calculating the spontaneous and stimulated recombination rates; the shape of the conduction and valence band density of states and the transition probability. In pure semiconductors parabolic bands may be assumed and the transition probability is governed by the k-selection rules. In heavily doped semiconductors the parabolic band structure is perturbed and 'tails' exist in the otherwise parabolic density of states. The transition probability is also altered in heavily doped semiconductors. There are regions deep within the bandtails where k-selection rules do not hold and regions well into the parabolic band where they do. This latter case, which is the most common in laser

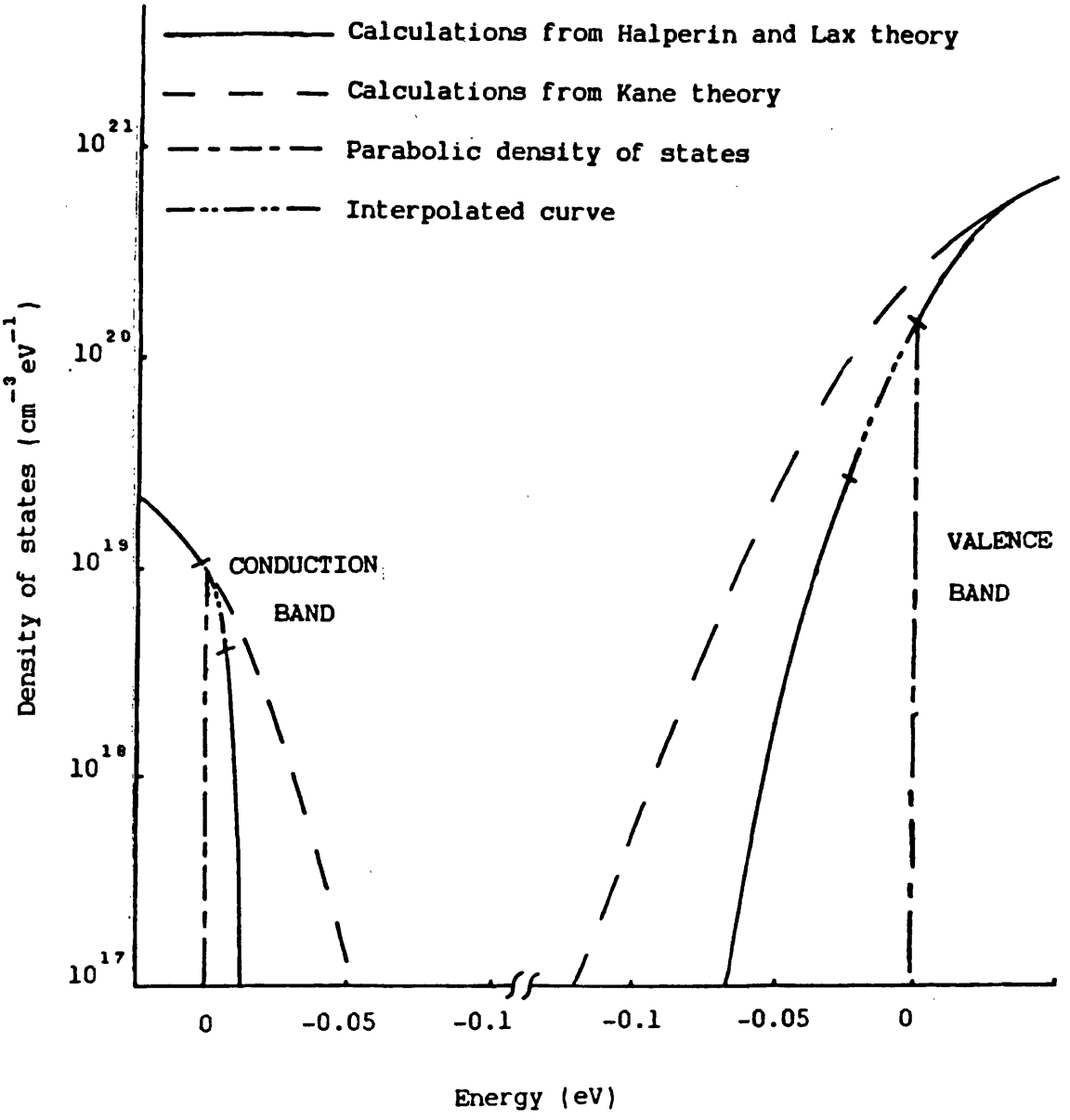

Fig(2.4) Comparison of the density of states in the bandtails of GaAs obtained from the Kane model and the Halperin and Lax model. Curves apply for $N_a = 6 \times 10^{18} cm^{-3}$ and $N_d = 3 \times 10^{18} cm^{-3}$ at a temperature of 300K and with an injection level required to give a gain of $100 cm^{-1}$. [22].

materials, is extremely complicated and simifying approximations are usually made. These amount to either assuming that k-selection rules apply throughout the band or that they do not. Which of these approximations one makes does not appear to be too critical, Hwang, [22], having shown that the length and shape of the bandtail states are the most important factors governing the spontaneous and stimulated emission distributions, a fact that also shows up in the work of Goebel, [23]

The model, [24], that is adopted here assumes bandtail states in the form used by Kane, [19], and k-selection rules. The choice of this combination was made because the active layers of our SLDs are only moderately doped so that it seemed appropriate to use some characteristics of both the pure and heavily doped semiconductor models. The constant matrix approximation is also made so that the transition probability becomes independent of the initial and final energy states, simplifying the computation considerably. Both the light and heavy hole valence bands are accounted for in the model by summing over both bands.

The whole process therefore involves solving equations (2.47) and (2.48) for the spontaneous and stimulated emission rates that apply when k-selection rules are assumed together with Kane's form for the density of states, equation (2.55). The constant matrix element approximation implies that the transition probability in equations (2.47) and (2.48) is a constant and can be removed from the integrals. This constant is the bimolecular recombination rate and it can be calculated using equations (2.32) and (2.36). However it is convenient to keep it as a variable parameter in the model so that the magnitude of the spontaneous and stimulated emission distributions can be altered. Likewise, the bandtailing parameter,

η_c, in equation (2.55), is also kept as a variable allowing the length of the bandtails to be altered providing a certain ammount of control over the shape of the spontaneous and stimulated emission distributions. A further approximation, which is made purely from the point of view of speeding the computation of the SLD model described in chapter(4), is to assume that the integral over energy of the spontaneous emission distribution gives the form of the bimolecular recombination equation, equation(2.53). This is of course not strictly valid when k-selection rules are assumed because of the reduced density of states term in equation(2.47); however, when the integrated value for the spontaneous emission is plotted against the product of the electon and hole concentrations, fig(2.5), it can be approximated to a straight line to within 10%. The gradient of the curve also gives the bimolecular recombination constant, B_r. As the bimolecular recombination constant is widely quoted in the literature and because it is directly proportional to the transition probability its value will be quoted rather than that of the transition probability when the spontaneous and stimulated emission distributions are scaled.

A range of spontaneous emission distributions for various bimolecular recombination constants and bandtailing parameters are shown in figs(2.6-2.10). The most striking feature of these graphs is the way in which the spontaneous emission distribution extends over a much larger energy range than the local gain. In fact, the peak of the spontaneous emission distribution coincides with a region of high absorption. The implication of this is that only a small part of the spontaneous emission experiences gain and contributes to the amplified spontaneous emission spectra of superluminescent diodes. It can be seen from figs(2.6-2.8) that B_r has a large effect on the

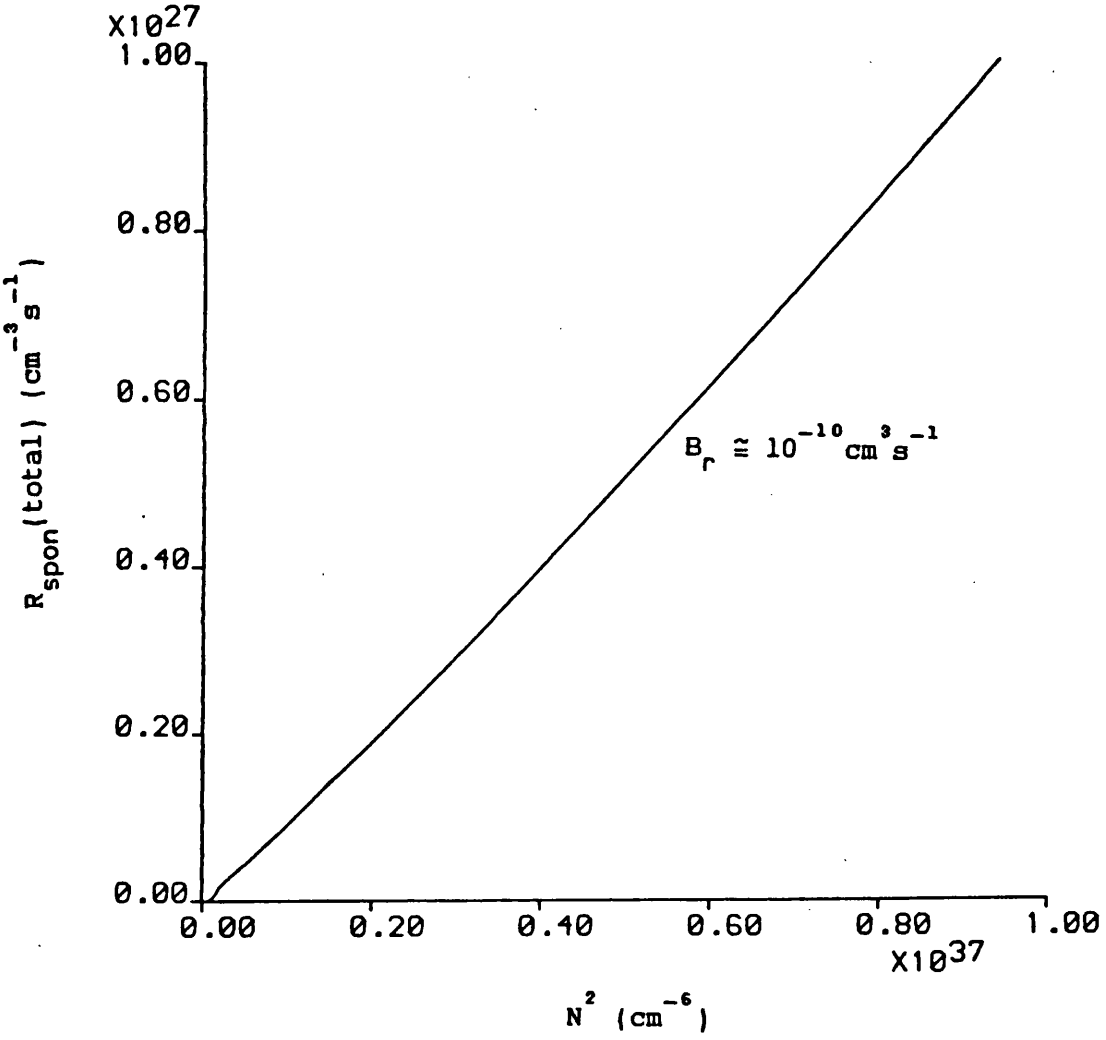

Fig(2.5) Total spontaneous emission rate plotted as a function of the inversion population squared. The gradient gives an approximate value for the bimolecular recombination rate.

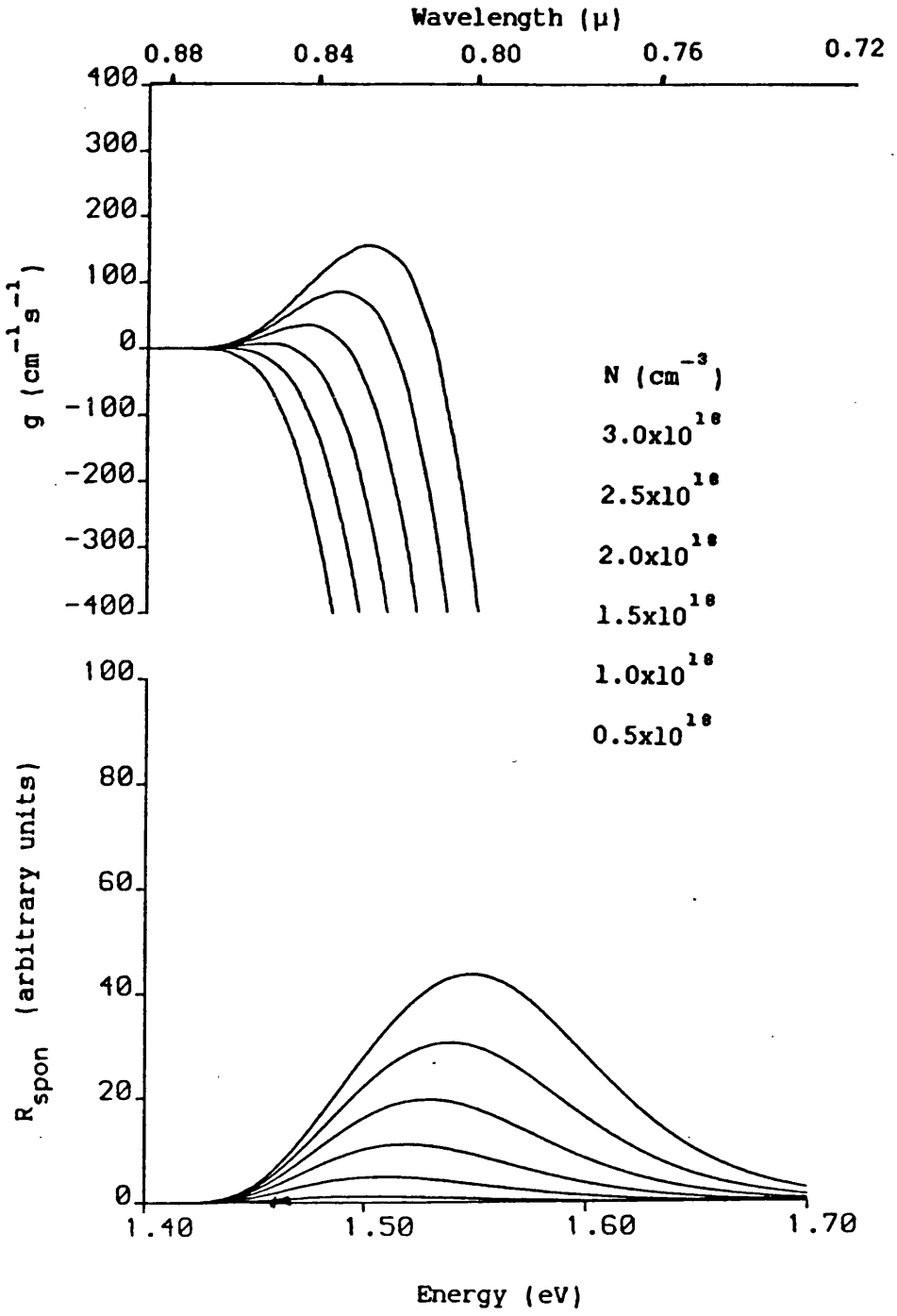

Fig(2.6) Local gain, g, (top) and spontaneous emission rate, R_{spon}, (bottom) v energy for various values of inversion population. $B_r = 0.6 \times 10^{-10} cm^3 s^{-1}$ and $n_c = 0.6$ eV.

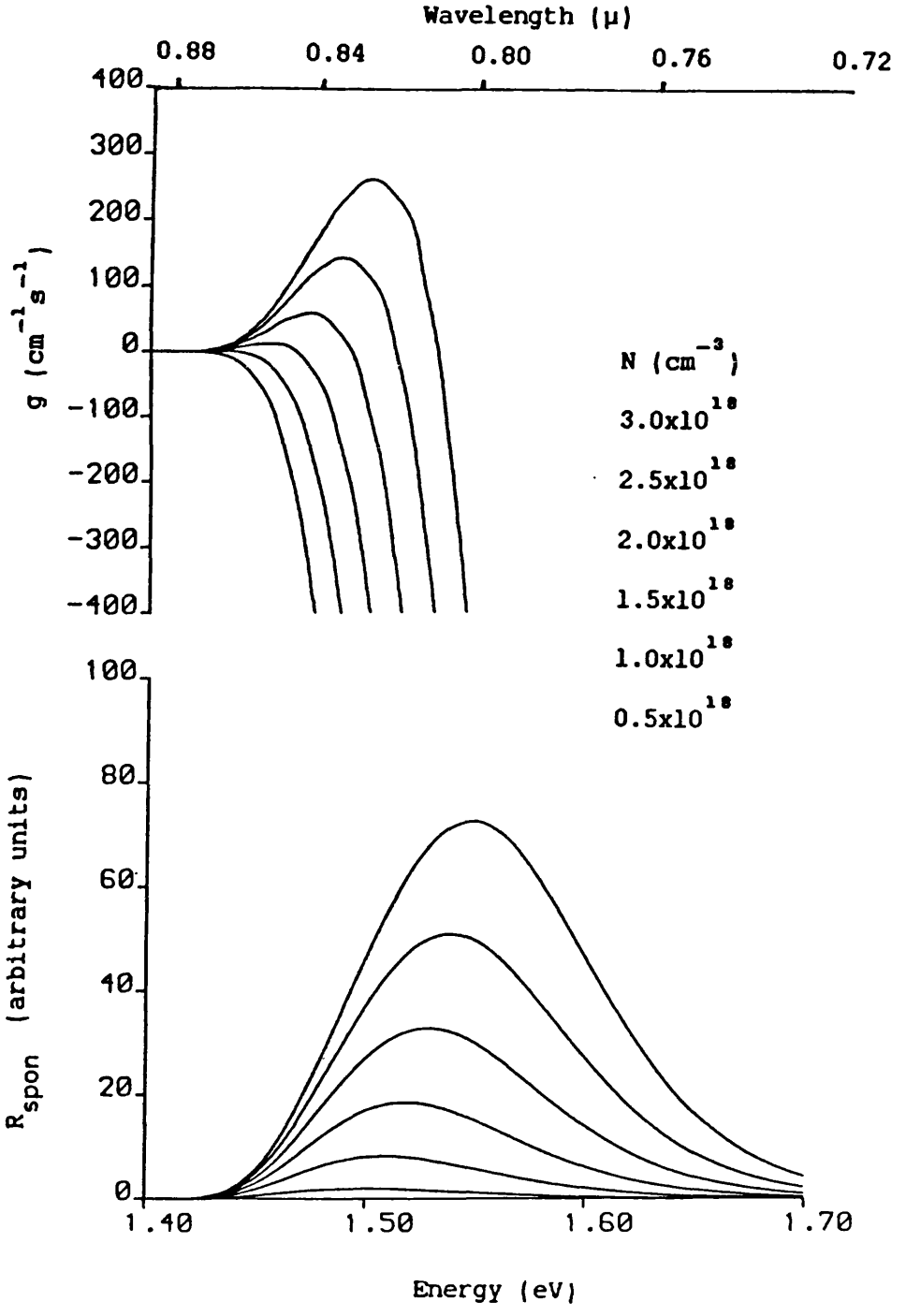

Fig(2.7) Local gain, g, (top) and spontaneous emission rate, R_{spon}, (bottom) v energy for various values of inversion population. $B_r = 1.0 \times 10^{-10}$ cm^3 s^{-1} and $\eta_c = 0.6$ eV.

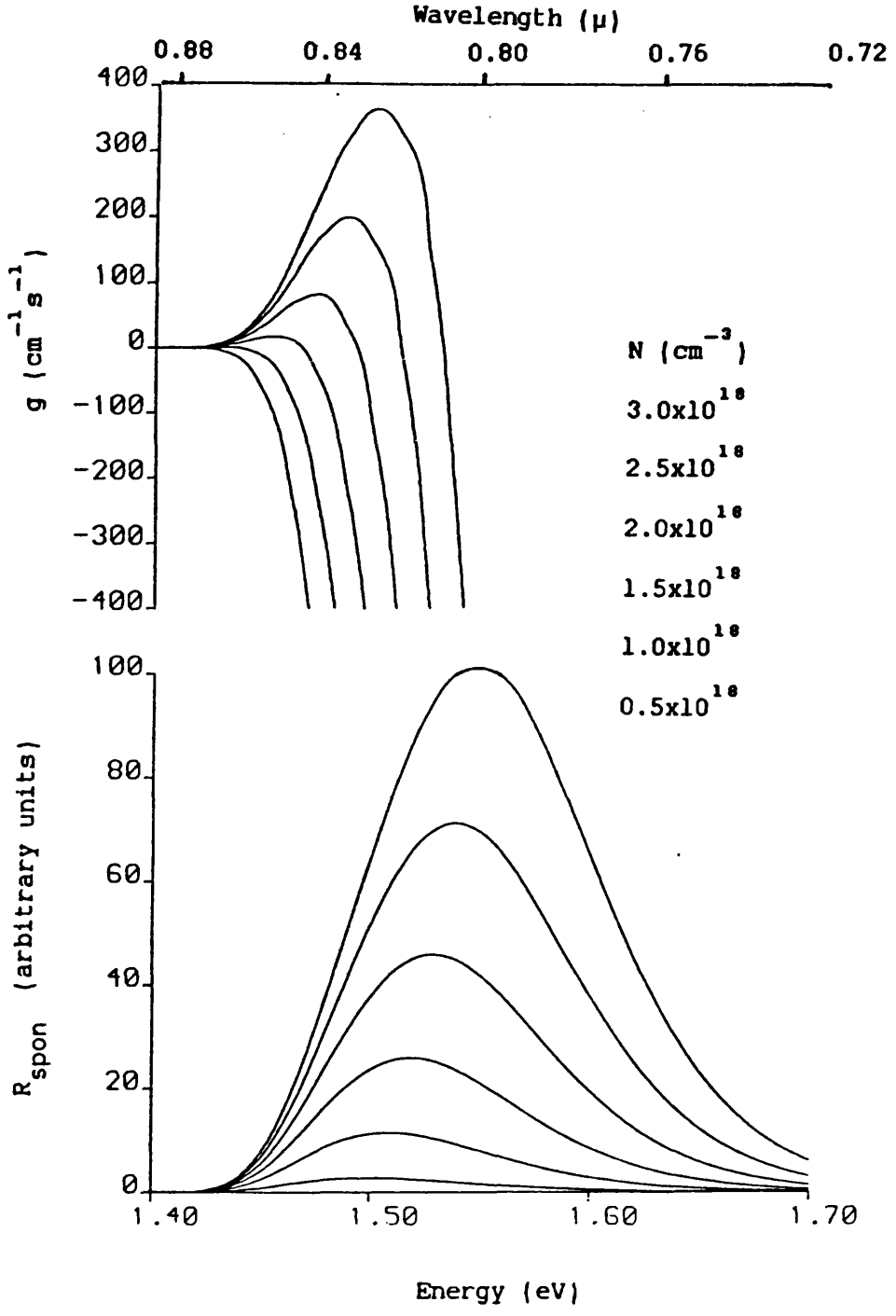

Fig(2.8) Local gain, g, (top) and spontaneous emission rate, R_{spon}, (bottom) v energy for various values of inversion population. $B_r = 1.4 \times 10^{-10}$ cm^3 s^{-1} and $n_c = 0.6$ eV.

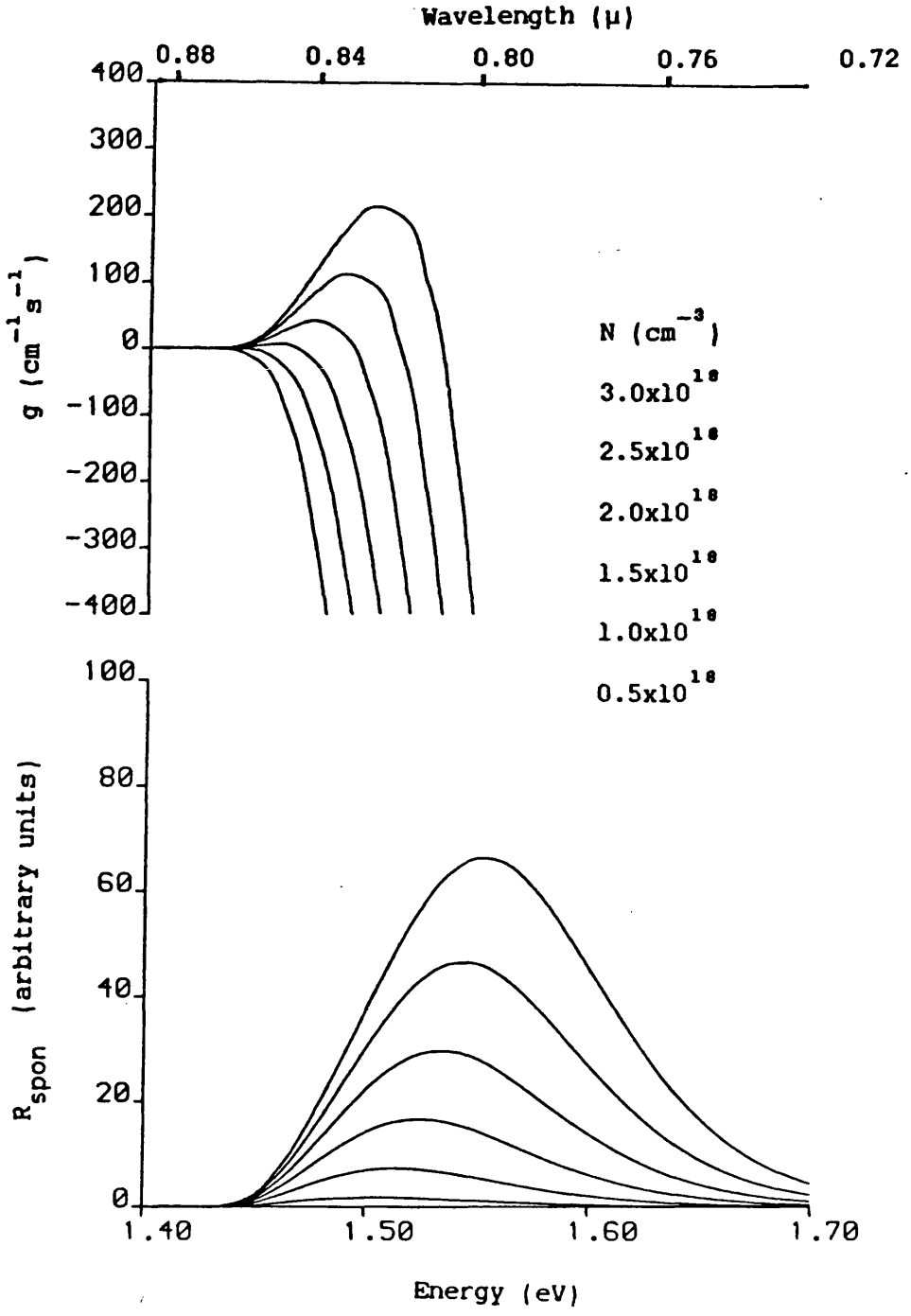

Fig(2.9) Local gain, g, (top) and spontaneous emission rate, R_{spon}, (bottom) v energy for various values of inversion population. $B_r = 1.0 \times 10^{-10}$ cm^3 s^{-1} and $\eta_c = 0.4$ eV.

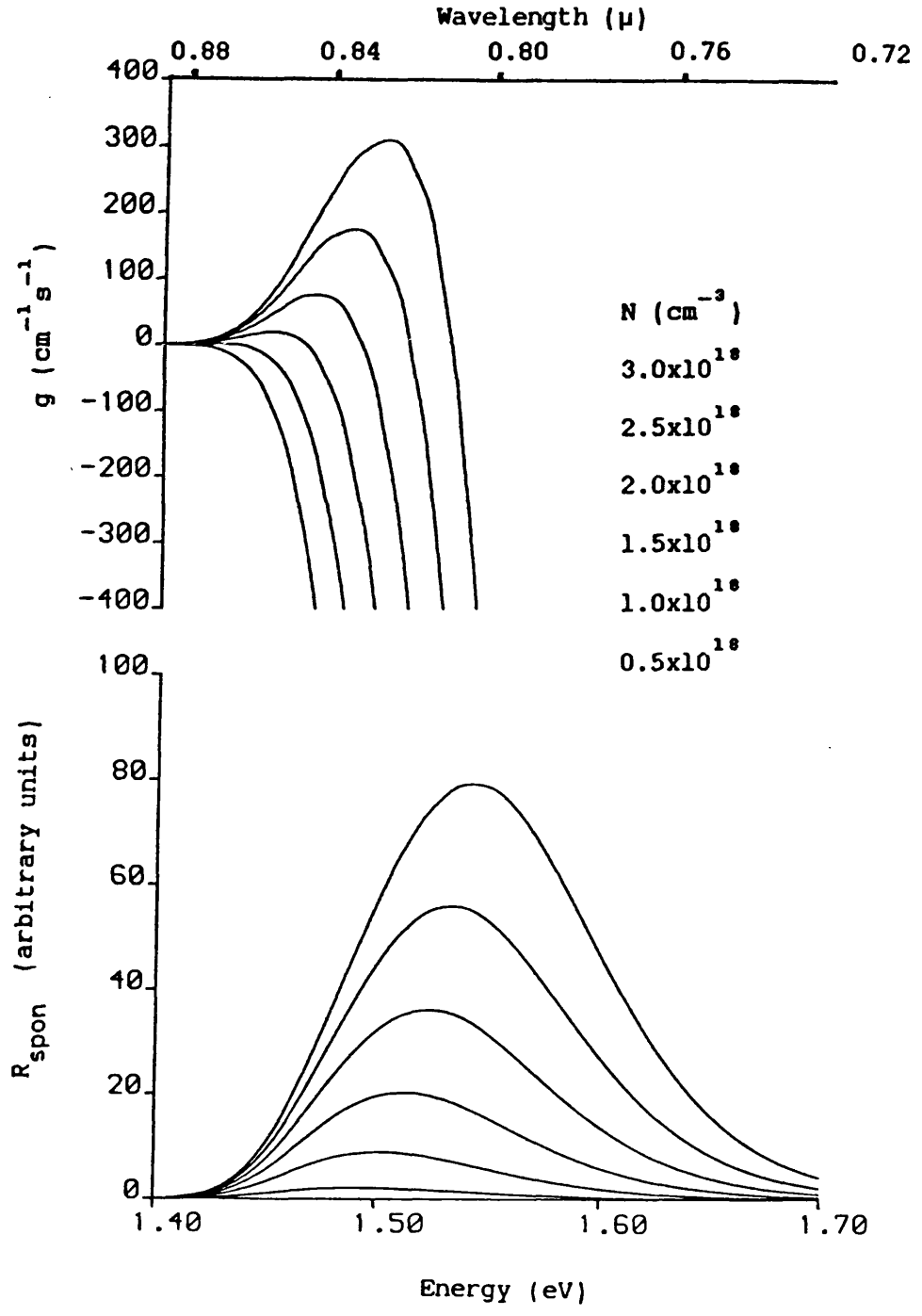

Fig(2.10) Local gain, g, (top) and spontaneous emission rate, R_{spon}, (bottom) v energy for various values of inversion population. $B_r = 0.6 \times 10^{-10}$ cm^3 s^{-1} and $\eta_c = 0.8$ eV.

magnitude of the gain and spontaneous emission distributions while leaving their shapes relatively unchanged. This is in complete contrast to the bandtailing parameter, η_c, which alters the complete shape of the gain and spontaneous emission distributions, figs(2.7,2.9 and 2.10). Note that η_c also alters the magnitude of the gain and spontaneous emission distributions, however, its effect is much less than that of altering B_r.

2.7 Concluding remarks.

A detailed description of light emission processes has been given in sections(2.2-2.5) culminating in the development of a simple but realistic model of the spontaneous and stimulated emission distributions as detailed in section(2.6). The model assumes k-selection rules and uses Kane bandtails. The constant matrix element approximation is used and it is assumed that the spontaneous emission rate takes on the form of the bimolecular recombination equation. These approximations are made because the model is specificaly designed to give a certain ammount of control over the magnitude and spectral shape of the spontaneous and stimulated emission distributions. The magnitude of the spontaneous and stimulated emission distributions is dominated by the bimolecular recombination rate and their spectral shape is governed by the bandtailing parameter. The test of the model was done by including the spontaneous and stimulated emission distributions in the SLD model outlined in chapter (4) and comparing it with experimental measurements in chapter (5).

References.

1) 'Analysis of spontaneous emission effects on spectra and L vs I characteristics of diode lasers', W.Streifer, D.R.Scifres and R.D.Burnham, Jap. J. of Appl. Phys., vol.21, No.5, p.L282, 1982.

2) 'Spectral behaviour and linewidth of (GaAl)As-GaAs double-heterostructure lasers at room temperature with stripe geometry configuration', S.Iida, K.Takata and Y.Unno, IEEE J. of Quant. Electron., vol.QE-9, no.2, 1973.

3) 'Longitudinal mode competition in semiconductor lasers (rate equations revisited)', M.J.Adams and M.Osinski, IEE Proc., Vol.129, pt.1, No.6, p.271, 1982.

4) 'Transversal modes in spectral dynamics of the semiconductor laser', J.Buus and M.Danielsen, IEEE J.Quant.Electron, Vol QE-13, No.8, p.669, 1977.

5) 'Spontaneous and stimulated recombination in semiconductors', G.Lasher and F.Stern, Phys.Rev., vol.133, p.A553, 1964.

6) 'Band-tail model for optical absorption and for the mobility edge in amorphous silicon', F.Stern, Phys.Rev., Vol.3, p.2636, 1971.

7) ' Concentration dependent absorbtion and spontaneous emission of heavily doped GaAs, H.C.Casey,Jr and F.Stern, J.Appl.Phys., Vol.47, No.2, p.631, 1976.

8) 'Gain-current relation for GaAs lasers with n-type and undoped active layers', F.Stern, IEEE.J.Quant.Electron., QE-9, p290, 1973.

9) 'Calculated spectral dependence of gain in excited GaAs', F.Stern, J.Appl.Phys., Vol.47, No.12, p.5382, 1976.

10) 'Approximate calculation of the spectral function for the stimulated recombination radiation in semiconductors', F.Maranelli, Solid State Electronics, Vol.8, p.939, 1965.

11) 'Properties of spontaneous emission in GaAs junction lasers. II

Temperature dependence of threshold current and excitation dependence of superradiance spectra', C.J.Hwang, Phys.Rev.B, vol.2, no.10, p.4126, 1970.

12) 'Physics of semiconductor laser devices', G.H.B.Thompson, John Wiley and Sons,Ltd.

13) 'Heterostructure lasers', H.C.Casey,Jr. and M.B.Panish, Academic Press, 1978.

14) 'Laser conditions in semiconductors', M.G.A.Bernhard and G.Duraffourg, Phys.Status Solidi., Vol.1, p.699, 1961.

15) 'Basic Quantum Mechanics', R.L.White, McGraw-hill, New York, 1966.

16) 'Band structure of Indium Antimonide', E.O.Kane, J.Phys.Chem.Solids,Vol.1, p.249, 1957.

17) 'Optical absorption and recombination radiation in semiconductors due to transitions between hydrogen-like acceptor impurity levels', D.M.Eagles, J.Phys.Chem.Solids, Vol.16, p.76, 1960.

18) 'Theory of the band structure of very degenerate semiconductors', P.A.Wolff, Phys.Rev., Vol.126, p.405, 1962.

19) 'Thomas-Fermi approach to impure semiconductor band structure', E.O.Kane Phys.Rev. Vol.131, p.79 and p.1532, 1963.

20) 'Semicondutors', R.A.Smith, Cambridge University Press, London, 1959, p.22.

21) 'Impurity-band tails in the high density limit. 1. Minimum counting methods', B.I.Halperin and M.Lax, Phys.Rev, vol.148, no.2, p.722, 1966.

22) 'Properties of Spontaneous Emission in GaAs junction lasers. 1. Densities of states in the active regions', C.J.Hwang, Phys.Rev.B, vol2, no10, p.4117, 1970.

23) 'Wavelength dependence of gain saturation in GaAs Lasers',

E.O.Goebel, O.Hildebrand and K.Lohnert, IEEE J. of Quant. Electron., vol.QE-13, p.848, 1977.

24) Computer model developed by W.J.Liddell, University of Bath.

CHAPTER 3

WAVE PROPAGATION IN SLD AND LASER STRUCTURES

3.1 Introduction.

The main purpose of this chapter is to describe how the optical fields that exist in the active layer of DH semiconductor SLDs, or lasers, propagate. In the direction perpendicular to the junction these fields spread significantly outside of the active layer and into the adjacent passive layers. This is in complete contrast to the almost total carrier confinement to the active layer that the heterostructure provides. It is therefore of particular importance to be able to calculate the fraction of the optical fields that remain inside the active layer and are able to interact with the carriers.

The analysis of wave propagation in the direction perpendicular to the junction begins by considering the double heterostructure as a symmetrical dielectric slab waveguide. The main approximation involved in this approach is to assume that the layers immediately adjacent to the active layer are optically infinite. This is a good approximation because the passive layers are specifically designed to be thick enough for the optical fields to decay sufficiently in that distance. The solutions of Maxwell's equations in a dielectric slab waveguide give rise to two sets of modes, transverse electric, TE, and transverse magnetic, TM, which are orthogonal. In lasers the TE modes are so dominant above threshold that it is common practice to neglect the TM modes and calculate only the confinement of the TE modes to the active layer, TE confinement

factor. The polarisation selectivity of lasers stems from the facet reflectivities for the TE modes being considerably greater than that for the TM modes. Consequently when the laser's threshold condition is reached only the TE modes resonate. SLD's have quite different polarisation characteristics to lasers because the optical feedback is surpressed. Both TE and TM fields are therefore present in comparable amounts, so that it is necessary to calculate both the TE and TM confinement factors.

In conventional stripe geometry lasers and SLDs the optical fields are also confined in the lateral direction even though the variation of the refractive index is slight. There are two competing mechanisms at work; an antiguiding effect produced by the injected carriers and a guiding effect due to the optical gain. When the gain rather than the refractive index influences the field distribution the fields are said to be 'gain-guided. The lateral guiding direction is of particular importance in narrow stripe lasers where it has been shown to be the cause of kinks in the light/current characteristics and also to produce spatial instabilities, [2-5]. These problems have lead to the development of laser and SLD structures which have a built in two-dimensional waveguide to provide real index guiding in the lateral direction as well as in the direction perpendicular to the junction, [6,7]. The real index guiding in the lateral direction leads to increased stability and higher output powers in single mode operation. In wide stripe devices that have no inbuilt real index guiding, such as the SLDs considered in this project, it has become common practice to assume that there are sufficient modes propagating to allow a plane wave, ray optics, approach to be used in the lateral direction, [8,9].

The mode analysis begins, in section (3.2), with the statement of Maxwell's equations and the derivation of the wave equation. The procedure for solving the symmetrical slab waveguide problem is then outlined in section (3.3). It is shown that a cut-off frequency exists for higher order modes for a given wavelength, active layer thickness, and refractive indices of the active and passive layers. This provides a design criteria for the maximum active layer thickness of DH SLDs and lasers for the propagation of only the fundamental TE and TM modes. The analysis then proceeds to the calculation of the confinement factors for the fundamental TE and TM modes which is described in detail in section (3.4). For completeness, a discussion of the lateral waveguiding mechanisms are given in section (3.5). Finally some concluding remarks are made in section (3.6)

3.2 The wave equation.

The wave equation provides a natural and logical starting point for the analysis of wave propagation in heterostructures. To derive the wave equation it is first necessary to state Maxwell's equations. These are the fundamental equations of electromagnetic theory and are

$$\nabla \times \underline{E} = - \frac{\delta \underline{B}}{\delta t} \qquad (3.1)$$

$$\nabla \times \underline{H} = \underline{J} + \frac{\delta \underline{D}}{\delta t} \qquad (3.2)$$

$$\nabla \cdot \underline{D} = \rho \qquad (3.3)$$

$$\nabla \cdot \underline{B} = 0 \qquad (3.4)$$

where $\underline{E}$ is the electric field vector, $\underline{B}$ is the magnetic flux density vector, $\underline{H}$ is the magnetic field vector, $\underline{J}$ is the current density vector, $\underline{D}$ is the electric flux density vector, and ρ is the charge density. When the field quantities are small in amplitude, as in the case considered here, a linear relationship exists between the various field quantities through the constitutive relations which are

$$\underline{D} = \varepsilon \cdot \underline{E} \tag{3.5}$$

$$\underline{B} = \mu \cdot \underline{H} \tag{3.6}$$

$$\underline{J} = \sigma \cdot \underline{E} \tag{3.7}$$

where ε is the dielectric constant, μ is the magnetic permiability and σ is the conductivity. Using the constitutive relations equations (3.1) and (3.2) may be rewritten as

$$\nabla \times \underline{E} = -\frac{\delta \underline{B}}{\delta t} = -\frac{\mu \delta \underline{H}}{\delta t} \tag{3.8}$$

$$\nabla \times \underline{H} = \underline{J} + \frac{\delta \underline{D}}{\delta t} = \sigma \underline{E} + \frac{\varepsilon \delta \underline{E}}{\delta t} \tag{3.9}$$

respectively.

The wave equation for the electromagnetic field is obtained as follows:

$$\nabla \times \nabla \times \underline{E} = -\frac{\mu \delta (\nabla \times \underline{H})}{\delta t} \tag{3.10}$$

from the vector identity

$$\nabla \times \nabla \times \underline{E} = \nabla (\nabla \cdot \underline{E}) - \nabla^2 \underline{E} \tag{3.11}$$

and equation(3.9), obtain

$$\nabla(\nabla \cdot \underline{E}) - \nabla^2 \underline{E} = -\mu\sigma\frac{\delta \underline{E}}{\delta t} - \mu\varepsilon\frac{\delta^2 \underline{E}}{\delta t^2} \qquad (3.12)$$

where ∇^2 is the laplacian operator given by

$$\nabla^2 = \frac{\delta^2}{\delta x^2} + \frac{\delta^2}{\delta y^2} + \frac{\delta^2}{\delta z^2} \qquad (3.13)$$

From equations (3.3) and (3.5), when the charge density is zero,

$$\nabla \cdot \underline{D} = \nabla \cdot \varepsilon\underline{E} = 0$$

i.e $$\nabla \cdot \varepsilon\underline{E} = \underline{E} \cdot \nabla\varepsilon + \varepsilon\nabla \cdot \underline{E} = 0$$

and therefore

$$\nabla \cdot \underline{E} = -(\underline{E}/\varepsilon) \cdot \nabla\varepsilon \qquad (3.14)$$

Equation (3.12) then reduces to the general wave equation

$$\nabla^2 \underline{E} + \nabla\{(\underline{E}/\varepsilon) \cdot \nabla\varepsilon\} = \mu\varepsilon\frac{\delta^2 \underline{E}}{\delta t^2} + \mu\sigma\frac{\delta \underline{E}}{\delta t} \qquad (3.15)$$

In a homogeneous medium $\nabla\varepsilon \equiv 0$, or if $\underline{E}$ is perpendicular to $\nabla\varepsilon$,then from equation (3.14)

$\nabla \cdot \underline{E} = 0$. Whence

$$\nabla^2 \underline{E} = \mu\varepsilon\frac{\delta^2 \underline{E}}{\delta t^2} + \mu\sigma\frac{\delta \underline{E}}{\delta t} \qquad (3.16)$$

Furthermore if $\sigma = 0$ the familiar wave equation results

$$\nabla^2 \underline{E} = \mu\varepsilon\frac{\delta^2 \underline{E}}{\delta t^2} \qquad (3.17)$$

Equation(3.17) can be rewritten as

$$\nabla^2 \underline{E} = \frac{1}{v^2} \frac{\delta^2 \underline{E}}{\delta t^2} \qquad (3.18)$$

where $v = 1/\sqrt{(\varepsilon\mu_0)}$ and has the physical dimensions of being the velocity of light in the medium. Taking $\exp(j\omega t)$ time dependence gives

$$\nabla^2 \underline{E} = \frac{\omega^2 \underline{E}}{v^2} = k^2 \underline{E} \qquad (3.19)$$

where ω is the angular frequency, ($= 2\pi\nu$) and k is the propagtion constant in the unbounded region. In a region of refractive index, n, the wave equation is

$$\nabla^2 \underline{E} = k_0^2 n^2 \underline{E} \qquad (3.20)$$

where $k^2 = k_0^2 n^2$; k_0 being the free space propagation constant.

3.3 The symmetrical slab waveguide.

The analsis of the symmetrical slab waveguide proceeds as follows. Consider a lossless dielectric slab of thickness d in the vertical 'y' direction and of infinite extent in the 'x' and 'z' directions and having a refractive index, n_1, fig(3.1). It is embedded in an infinite medium characterised by the refractive index, n_2. Solutions of Maxwell's equations having an invariant field shape along 'y' and 'z' are sought.

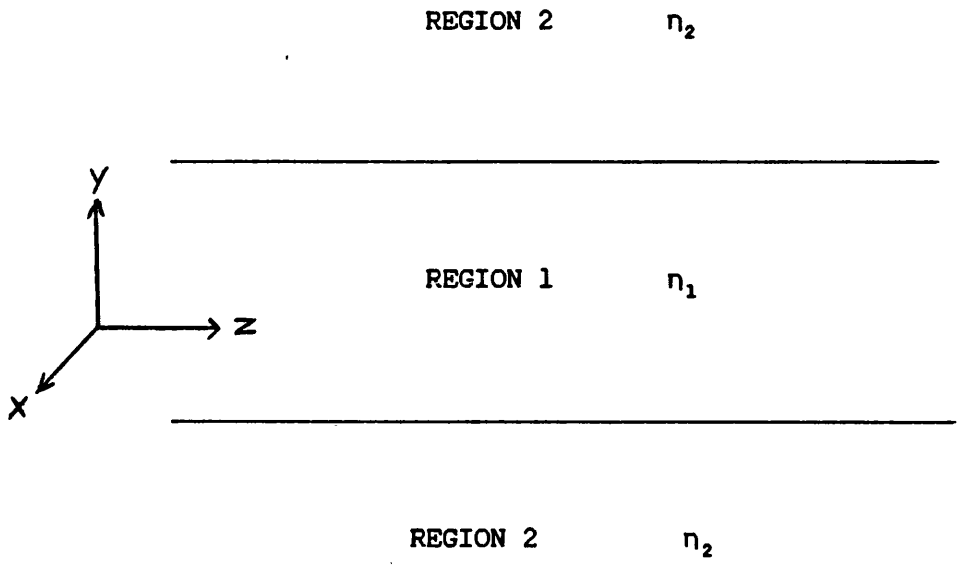

Fig(3.1) Schematic diagram of a symmetrical slab waveguide.

It is well known that $(TE)_y$ and $(TM)_y$ polarised field distributions can be independently supported by this waveguide. Solutions of the wave equations for both cases are given below.

3.31 TE modes.

For TE waves, $E_y = 0$ by definition and as the waveguide is infinite in extent in the 'x' direction $\delta/\delta x = 0$. Equations (3.8) and (3.9) give $H_x = E_z = 0$; i.e. TE waves have non-zero components E_x, H_y and H_z. Since a lossless slab is being considered $\sigma = 0$ and equation (3.17) may be written as

$$\frac{\delta^2 E_x}{\delta y^2} + \frac{\delta^2 E_x}{\delta z^2} = \mu\varepsilon\frac{\delta^2 E_x}{\delta t^2} \qquad (3.21)$$

or in the form of equation (3.20) as

$$\frac{\delta^2 E_x}{\delta y^2} + (n^2 k_0^2 - \beta^2)E_x = 0 \qquad (3.22)$$

where the t and z variation of the field is

$$E_x(y,z,t) = E_x(y).\exp j(\omega t - \beta z) \qquad (3.23)$$

In the following analysis the exponential factor is surpressed. A solution of equation (3.22) in the waveguide, region 1 in fig (3.1), is given by

$$E_x(y) = A.\cos(k_1 y) + B.\sin(k_1 y) \qquad (3.24)$$

where

$$k_1^2 = n_1^2.k_0^2 - \beta^2 \qquad (3.25)$$

As pointed out by Marcuse, [10], the analysis is simplified by considering the even and odd solutions seperately so that only the case $y > 0$ needs to be considered. Within the guide for $|y| < d/2$ the even mode is given by equation (3.24) as

$$E_x = A.\cos(k_1|y|) \qquad (3.26)$$

The H_z component of the magnetic field can be found from equation (3.8) which gives

$$\frac{-\delta E_x}{\delta y} = -j\omega\mu H_z \qquad (3.27)$$

or

$$H_z = -\frac{k_1}{j\omega\mu}.A.\sin(k_1|y|) \qquad (3.28)$$

Outside of the waveguide, region 2 in fig(3.1), the field must decay in order to produce modes that are bound to the slab waveguide. Therefore outside of the guide, for $|y| > d/2$, the E_x component is given by

$$E_x = C.\exp(-k_2(|y|-d/2)) \qquad (3.29)$$

but as E_x is continuous at the interface, $|y| = d/2$, it follows that

$$E_x = A.\cos(k_1 d/2).\exp(-k_2(|y|-d/2)) \qquad (3.30)$$

where

$$k_2^2 = \beta^2 - n_2^2.k_0^2 \qquad (3.31)$$

The H_z component of the magnetic field in region 2 is obtained from equation (3.27)

$$H_z = \frac{-k_2.A.\cos(k_1 d/2).\exp(-k_2(y-d/2))}{j\omega\mu} \qquad (3.32)$$

The eigenvalue equation is obtained from the boundary condition at $|y| = d/2$ that H_z is continuous. Then equations (3.28) and (3.32) combine to yield

$$\tan(k_1.d/2) = k_2/k_1 \qquad (3.33)$$

which may be rewritten as

$$u.\tan(u) = w \qquad (3.34)$$

where $u = k_1.d/2$ and $w = k_2.d/2$

Using a similar analysis the eigenvalue equation for the odd modes may be obtained. In region 1

$$E_x = B.\sin(k_1 y) \tag{3.35}$$

$$H_x = -\frac{k_1}{j\omega\mu}.B.\cos(k_1 y) \tag{3.36}$$

and in region 2

$$E_x = B.\sin(k_1 d/2).\exp(-k_2(y-d/2)) \tag{3.37}$$

$$H_x = -\frac{k_2}{j\omega\mu}.B.\sin(k_1 d/2).\exp(-k_2(y-d/2)) \tag{3.38}$$

and the resulting eigenvalue equation is

$$u.\cot(u) = -w \tag{3.39}$$

A further relationship between u and w can be found involving the effective frequency of the waveguide. This quantity depends on the different refractive indices of the two regions and the waveguide thickness and is found by combining equations (3.25) and (3.31) to eliminate β giving

$$k_1^2 + k_2^2 = (n_1^2 - n_2^2).k_0^2 \tag{3.40}$$

which can be normalised by multiplying both sides of the equation by (d/2) to give

$$u^2 + w^2 = v^2 \tag{3.41}$$

where

$$v = \frac{2\pi}{\lambda_0}.\frac{d}{2}.\sqrt{(n_1^2 - n_2^2)} \tag{3.42}$$

Either graphical or numerical techniques are necessary to find solutions of the eigenvalue equations, (3.31), (3.34) and (3.39)

since they are transcendental. The graphical method of obtaining solutions as given , e.g., in Collin, [11] and shown here in figs (3.2) and (3.3), provide a useful insight into the eigenvalue equations. When plotting w against u the dispersion relation (3.41) is represented by a circle of radius v centred at the origin. The graphs of u.tan(u) and u.cot(u) have the form of modified tan and cot curves respectively. Solutions of the eigenvalue equations representing confined 'surface' modes occur when the curves intersect the 'dispersion circles' in the first quadrant. Note that for a given wavelength the active layer thickness and the refractive indices of the two regions must be assigned. Solutions exist with $w < 0$ and these represent modes excited within the guide that have fields with intensity increasing exponentially away from the interface. These are known as 'improper' modes. The surface modes are usually numbered so that the lowest even mode, with u between 0 and $\pi/2$, is number 0, the first odd mode is number 1, the second even mode is number 2, etc.

From the graphs, figs (3.2) and (3.3), it is noticable that for all values of v there is a solution for an even mode, but if v is less than $\pi/2$ the lowest odd mode is cut off. This fact, plus a knowledge of the refractive indices permits a value for d to be calculated below which only the fundamental TE mode will propagate. This condition can be expressed as

$$v^2 = (\pi/2)^2 \qquad (3.43)$$

so that

$$d = \frac{\lambda_0}{2\sqrt{(n_1^2 - n_2^2)}} \qquad (3.44)$$

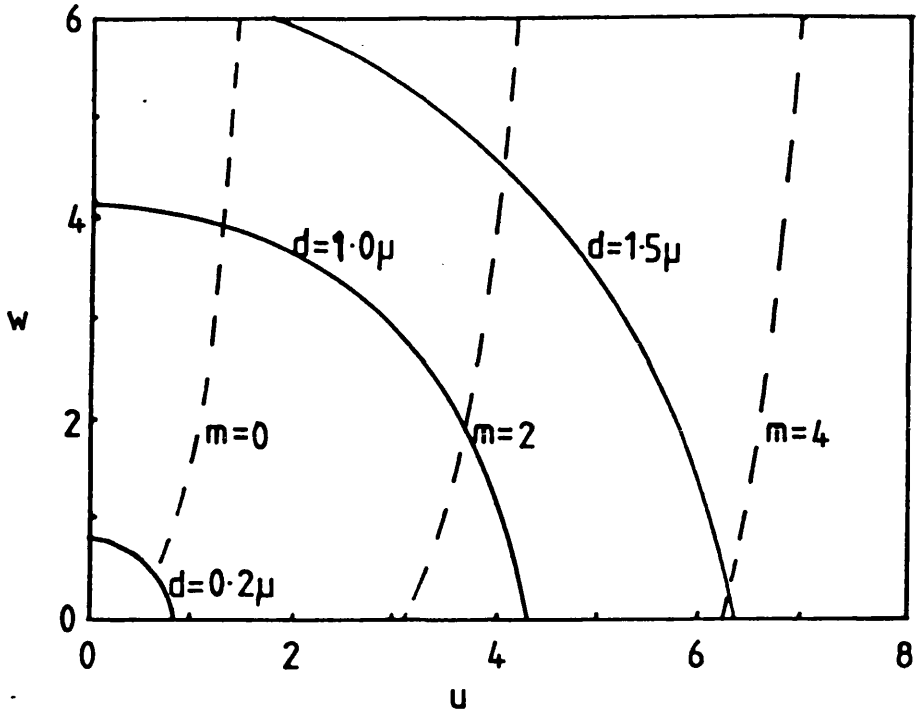

Fig(3.2) Graphical solution of the eigenvalue equation (3.34) for the even TE modes in a symmetrical slab waveguide.

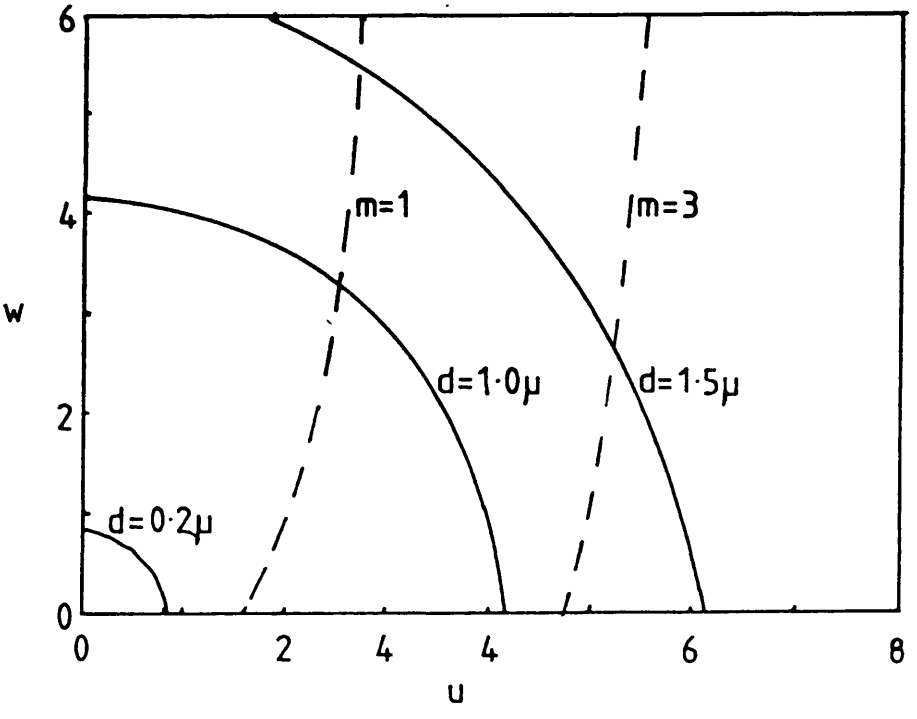

Fig(3.3) Graphical solution of the eigenvalue equation (3.39) for the odd TE modes in a symmetrical slab waveguide.

This expression is not only valid for the fundamental TE mode but also for the fundamental TM mode as it is derived from the dispersion relation for the material. It is instructive to consider some typical values for the GaAs/GaAlAs DH material that typical SLDs are made from. Taking $n_1 = 3.55$, $n_2 = 3.38$ and a minimum wavelength for the spectrum of $\lambda_0 = 0.82\mu$, gives a thickness for the active layer of 0.38μ below which only the fundamental TE and TM modes will propagate.

3.32 TM modes.

For TM modes $H_y = 0$ by definition, and as $\delta/\delta x = 0$ equations (3.8) and (3.9) give $E_x = H_z = 0$, i.e TM waves have non-zero components H_x, E_y and E_z. In the same manner as for TE waves, the wave equation for TM waves may be written as

$$\frac{\delta^2 H_x}{\delta y^2} + (n^2 k_0^2 - \beta^2)H_x = 0 \qquad (3.45)$$

and following a similar analysis as previously used for TE modes the eigenvalue equation for even TM modes is

$$u.\tan(u) = n_1^2/n_2^2.w \qquad (3.46)$$

and for odd TM modes is

$$u.\cot(u) = -n_1^2/n_2^2.w \qquad (3.47)$$

The obvious difference between the eigenvalue equations for TE and TM modes is the extra term n_1^2/n_2^2 in the TM equations. This extra term arises because $D_y = \varepsilon E_y$ is continuous at $|y| = d$, and therefore $\varepsilon_1 E_{y_1} = \varepsilon_2 E_{y_2}$. The TE mode has $E_y = 0$ hence the difference between the TE and TM modes.

3.4 Confinement factor.

In semiconductor lasers and SLDs the DH structure provides not only optical confinement, as described by the slab waveguide, but also carrier confinement. The carrier confinement can be assumed to be total for typical active layer thicknesses and AlGaAs compositional differences between the active and passive layers. This, however, is not the case for optical confinement where a significant portion of the optical fields spread into the passive layers and therefore cannot interact with the carriers. It is therefore necessary to calculate the fraction of the optical fields that remain inside the active layer. This fraction is known as the confinement factor, Γ and is defined as the power that remains in the active layer divided by the total power, i.e

$$\Gamma = \frac{1/2 \int_{-d/2}^{d/2} (\underline{E} \times \underline{H}^*)\delta\underline{a}}{1/2 \int_{-\infty}^{\infty} (\underline{E} \times \underline{H}^*)\delta\underline{a}} \qquad (3.48)$$

where $d\underline{a} = \hat{u}_z.\delta x.\delta y = \hat{u}_z.1.\delta x$ since the slab waveguide is uniform along x. For symmetric slab waveguides the above equation may be written as

$$\Gamma = \frac{\int_{0}^{d/2} (E \times H^*)\delta y}{\int_{0}^{d/2} (E \times H^*)\delta y + \int_{d/2}^{\infty} (E \times H^*)\delta y} \qquad (3.49)$$

The confinement factor for each propagating mode, is in general, different from that of other modes.

3.41 Confinement factor for the fundamental TE mode.

In the case of TE modes, where the field components $E_z = E_y = H_x = 0$, the expression for the confinement factor, equation (3.49), reduces to

$$\Gamma_{TE} = \left[1 + \frac{\int_{d/2}^{\infty} (E_x H_y^*)\delta y}{\int_{0}^{d/2} (E_x H_y^*)\delta y} \right]^{-1} \qquad (3.50)$$

Then by substituting for E_x from equations (3.30) and (3.37) in the active and passive layers respectively, and obtaining H_y from equation (3.8), as was done for H_z in equation (3.28) the expression becomes

$$\Gamma_{TE} = \left[1 + \frac{\int_{d/2}^{\infty} \cos^2(k_1 d/2).\exp(-2k_2(y - d/2))\delta y}{\int_{0}^{d/2} \cos^2(k_1 y)\delta y} \right]^{-1} \qquad (3.51)$$

The two integrals can be evaluated seperately to give

$$\int_{0}^{d/2} \cos^2(k_1 y)\delta y = 1/2(d/2 + 1/k_1.\sin(k\, d/2).\cos(k_1 d/2)) \qquad (3.52)$$

and

$$\int_{0}^{d/2} \cos^2(k_1 d/2).\exp(-2k_2(y - d/2))\delta y = \frac{\cos^2(k_1 d/2))}{2k_2} \qquad (3.53)$$

which combine to give the confinement factor for the fundamental TE mode as

$$\Gamma_{TE} = \left[1 + \frac{k_2(d/2 + 1/k_1.\sin(k_1 d/2).\cos(k_1 d/2))}{\cos^2(k_1 d/2)} \right]^{-1} \qquad (3.54)$$

An analytic approximation for the confinement factor for the fundamental TE mode which is accurate to 1.5% has been derived by Botez, [12], fig (3.4). This may be written as

$$\Gamma_{TE} = \frac{4v^2}{2 + 4v^2} \qquad (3.55)$$

where v is given by equation (3.42). In fig(3.4) a comparison of Botez's approximation with numerical results show how the TE confinement factor varies with the active layer thickness, d, for a number of refractive indices differences between the active and passive layers.

4.42 Confinement factor for the fundamental TM mode.

For TM modes the field components $E_x = H_z = H_y = 0$ and equation (3.50) for the confinement factor becomes

$$\Gamma_{TM} = \left[1 + \frac{\int_{d/2}^{\infty} (H_x E_y^*)\delta y}{\int_{0}^{d/2} (H_x E_y^*)\delta y} \right]^{-1} \qquad (3.56)$$

and using a similar analysis to that used for the TE confinement factor

$$\Gamma_{TM} = \left[1 + \frac{k_2(d/2 + 1/k_1.\sin(k_1 d/2).\cos(k_1 d/2))}{n_1^2/n_2^2.\cos^2(k_1 d/2)} \right]^{-1} \qquad (3.57)$$

is obtained. The only difference between the confinement factor for the TE and TM modes is the extra term, n_1^2/n_2^2, that arises in the

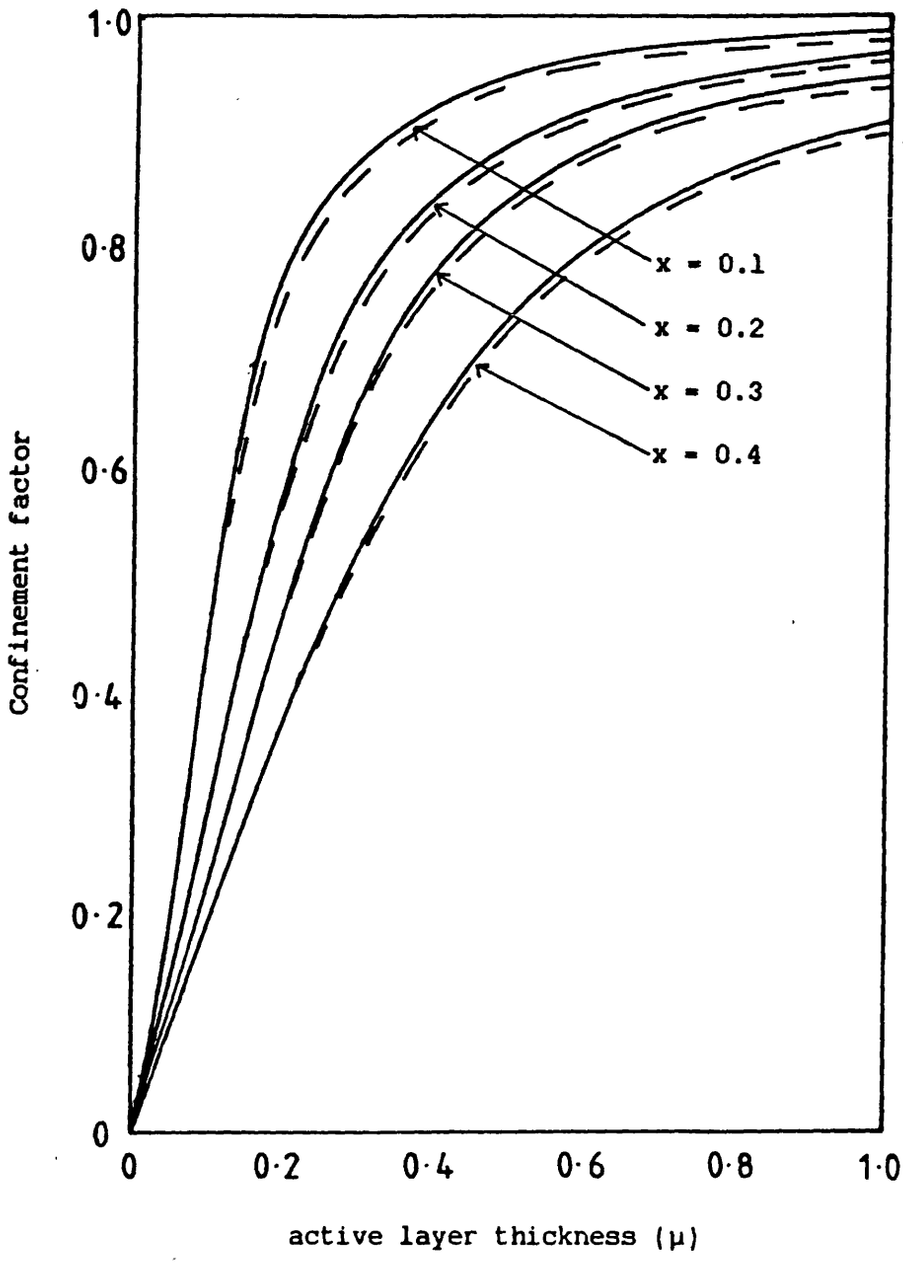

Fig(3.4) Comparison of numerically calculated curves for the confinement factor for the fundamental TE mode (solid lines) and Botez's approximation (dashed lines), [12]. The curves correspond to various aluminium contents (x) of a GaAs-$Al_xGa_{1-x}As$ double heterostructure.

denominator of the TM confinement factor.

Botez has also offered an analytic approximation to the confinement factor for the TM fundamental mode of the symmetrical dielectric slab, [13],

$$\Gamma_{TM} = \frac{2m^{4}v^{2}}{1 + 2m^{4}v^{2}} \qquad (3.58)$$

where v is given by equation (3.42) and

$$m = n_2/n_1 \qquad (3.59)$$

3.5 Gain Guiding.

It is now generally accepted that the dielectric properties of the active region are altered by the presence of injected carriers and the associated optical gain. Studies by various workers, [14-16], indicate that the real part of the dielectric constant may become lower beneath the stripe than in the passive region and the guiding mechanism is due to the optical gain. The distribution of injected carriers is therefore the dominant factor in determining the spread of light in the lateral direction.

Apart from providing gain the injected carriers produce a reduction in the refractive index in two seperate ways, [17]. First, there is the direct free-carrier interaction with the optical wave, the so-called plasma effect, the magnitude of which is proportional to the concentration of the injected carriers. Secondly, there is the band-to-band interaction with the injected carriers which accompanies the gain process and whose magnitude is related, by the Kramers-Kroenic relations, to the total dispersion of the gain spectrum, [18]. A comprehensive study of both these effects has been made by

Thompson, [19], who shows that these effects reduce the real part of the complex dielectric constant in an approximately linear relationship with the inversion population. This has been experimentally confirmed by Selway et al, [20]. The local gain also varies with the carrier density, however it is a positive function so that any increase in gain under the stripe is accompanied by a decrease in the refractive index.

The standard dielectric waveguide analysis is capable of dealing with such a situation because the optical gain can equally well be described in terms of an imaginary component of the dielectric constant. This form has been used by Schlosser, [14], for abrubt 'gain guiding' and by Cook and Nash, [15], and Hakki, [21], for continuosly distributed stripe waveguides. It has also been used by Unger, [22], in his treatment of the 'gain guiding' situation perpendicular to the junction in homostructure lasers. The analysis is in fact a two-dimensional problem because the dielectric constant variations cannot be written as a sum of independent x and y variations. As an approximation, seperation of the field variation in the x and y directions, by writing the field as a product of a purely y dependent and a purely x dependent function, allows the x direction to be treated independently. In [23,24] it was suggested to describe the x variation of the dielectric constant by a parabola. This makes it possible to express the x variation of the field by Hermite-Gaussian functions. This treatment has been extended to complex dielectric constants, [15,25], in order to account for gain variations. Apart from the parabola some other profiles allow analytical solution of the field problem, [21,26]. One of the problems with this type of method is that the stripe width of the device dictates which profile is best to use. An alternative and more

versatile method of solving this two-dimensional field problem is to use the 'effective dielectric constant (EDC) method', originally developed by Tulios and Knox, [27], to reduce it to one dimension. The EDC method has been successfully used to analyse a number of lossless passive dielectric waveguides and components, [28,29], and is particularly suited to the study of waveguiding in stripe-geometry DH lasers, [30].

Application of the EDC method makes it possible to replace the actual structure by a hypothetical homogeneous structure that is infinitely long in the x direction. Matching the tangential components of the electric and magnetic field at each interface allows the effective dielectric constant to be defined. The structure can then be replaced by another hypothetical homogeneous structure that is infinitely long in the y direction having the values of the effective refractive indices found earlier in the appropriate vertical layers. The field problem in the x direction is then solved as if it were a slab waveguide.

3.6 Concluding Remarks

The guiding mechanisms in lasers and SLDs has been discussed. In particular the double heterostructure that provides the guidance in the plane perpendicular to the junction has been treated by the symmetric slab model. It has been shown that only the fundamental TE and TM modes propogate if the active layer is thin enough. This provides a design parameter for lasers and SLDs. The analysis leads to expressions for the confinement factors of the fundamental TE and TM modes that are essential for modelling the polarisation characteristics of SLDs, see chapter(7). For completeness a general discussion of the guiding mechanisms in the

lateral direction is given however; it is worth stating again that the SLDs considered in this project are wide stripe devices that can be assumed to support enough lateral modes to make a plane wave 'ray optics' analysis a valid approximation in the lateral direction.

References.

1) ' Heterostructure lasers, Part A: Fundamental principles', H.C.Casey, Jr. and M.B.Panish, Academic press, 1978.

2) 'Lateral transverse mode instability and its stabilisation in stripe geometry lasers', R.Lang, IEEE J. Quant. Electron., vol.QE-15, p718, 1979.

3) 'Control of mode behaviour in semiconductor lasers', S.Wang, C.Chen, A.Liao and L.Figueroa, IEEE J. Quant. Electron., vol.QE-17, p.453, 1981.

4) 'Intrinsic pulsation in stripe-geometry DH semiconductor lasers', C.Z.Guo and K.G.Wang, IEEE J. Quant. Electron., vol.QE-18, p.1728, 1982.

5) 'Lateral mode behaviour in narrow stripe lasers', P.M.Asbeck, D.A.Cammack, J.J.Daniele and V.Klebanoff, IEEE J. Quant. Electron., vol.QE-15, p727, 1979.

6) 'GaAs-GaAlAs buried-heterostructure injection lasers', T.Tsukada, J. Appl. Phys., vol.45, p4899, 1974.

7) 'Transverse-junction stripe-geometry double heterostructure lasers with very low threhold current', H.Namizaki, H.Kan, M.Ishii, and A.Ito, J. Appl. Phys., vol.45, p2785, 1974.

8) 'A stripe-geometry double heterostructure amplified spontaneous emission (superluminescent) diode', T.P.LEE, C.A.Burrus, Jr., and B.I.Miller, IEEE J. of Quantum Electron., vol. QE-9, p820, 1973.

9) 'AlGaAs/GaAs double-heterostructure superluminescent diodes for optical transmission systems', J.Boeck and M.C.Amann, Frequenz, vol.33, p278, 1979.

10) 'Light transmission optics', D.Marcuse, p.305, Van Nostrand Reinhold, 1972.

11) 'Field theory of guided waves, R.E.Collin, p.470, McGraw-hill, 1960.

12) 'Analytic approximation of the radiation confinement factor for the TE_0 mode of a double-heterojunction laser', D.Botez, IEEE. J. of Quant. Electron., vol.QE-14, p.230, 1978.

13) 'Near and far-field analytic approximations for the fundamental mode in symmetric waveguide dh lasers', D.Botez, RCA Review, vol.39, p.577, 1978.

14) 'Gain-induced modes in planar structures', W.O.Schlosser, Bell Syst .Tech. J., vol.52, p.887, 1973.

15) 'Gain-induced guiding and astigmatic output beam of GaAs lasers', D.D.Cook and F.R.Nash, J. Appl. Phys., vol.46, p.1660, 1975.

16) 'Waveguiding in a stripe-geometry junction laser', T.L.Paoli, IEEE J. of Quant. Electron., vol.QE-13, p.662, 1977.

17) 'Physics of semiconductor laser devices', G.H.B.Thompson, John Wiley and Sons, 1980.

18) 'Electrodynamics of Continuous Media', L.D.Landau and E.M.Lifshitz, Permagon Press, 1960.

19) 'A theory for filimentation in semiconductor lasers including the dependence of dielectric constant on injected carrier density', G.H.B.Thompson, Opto-electronics, vol.4, p.257, 1972.

20) 'Measurement of the effect of injected carriers on the p-n refractive index step in single heterostructure diode lasers', P.R.Selway, G.H.B.Thomson, G.D.Henshall, and J.E.A.Whiteway, Electron.Lett., vol.10, p.453, 1974.

21) 'Striped GaAs lasers: mode size and efficiency', W.Hakki, J.Appl.Phys. vol.46, p.2723, 1975.

22) 'Modes in a semiconductor laser', K.Unger, Annalen der Physik, vol.19, p.64, 1979.

23) 'Proton-bombarded formation of stripe-geometry heterostructure lasers for 300K cw operation', J.C.Dyment, L.A.D'Asaro, J.C.North, B.I.Miller, and J.E.Ripper, Proc.IEEE, vol.60, p.726, 1969.

24) 'Resonant modes of GaAs junction lasers', T.H.Zachos and J.E.Ripper, IEEE J.Quantum.Electron., vol.QE-5, p29, 1969.

25) 'Mode guidence parallel to the junction plane of double-heterostructure GaAs lasers', F.R.Nash, J.Appl.Phys., vol.44, p.4696, 1969.

26) 'Analysis of gain induced waveguiding in stripe geometry diode lasers', W.Streifer, D.R.Scifres, R.D.Burnham, IEEE J.Quant.Electron., vol.QE-14, p.418, 1978.

27) 'Image line integrated circuits for applications at millimeter wavelengths', P.P.Toulios and R.M.Knox, U.S.Army Electronics Command, Final Report, Rept. No. ECOM-73-0217-F, 1974.

28) 'Inverted strip dielectric waveguide for millimeter wave integrated circuits', T.Itoh, IEEE Trans. Microwave Theory Tech., vol.MTT-24, p.821, 1976.

29) 'Two-dimensional analysis of the GaAs double hetero stripe-geometry laser', T.Rozzi, T.Itoh, and L.Grun, Radio Science, vol.12, p.543, 1977.

30) Heterostructure lasers, Part A: Fundamental Principles', Chap.2, Academic Press, 1978.

CHAPTER 4

A COMPREHENSIVE MODEL OF THE SUPERLUMINESCENT DIODE

4.1 Introduction

The SLD structure, fig (1.1a), proposed by Lee et al, [1], has been investigated by a number of authors, [e.g 2,3,4,5]. Simple analytic approximations for the light/current characteristics and the beamwidth (far-field angular distribution) in the plane of the junction were offered in [1]. To obtain the analytic expressions the inversion population was assumed to be constant along the length of the stripe contact. A very simplistic normalised frequency distribution was used in [2] to obtain the spectral half-width variation with current and stripe length. In this analysis the inversion population was also assumed to be constant along the stripe length. Subsequent publications, [3,4,5] have included the longitudinal variation of the inversion population. In [5] Marcuse not only obtains the light/current characteristics, previously puplished in [3,4], but also the far-intensity angular distribution. Unlike the previous analyses, [1,2,3,4], Marcuse's model assumes lateral confinement for the photons (i.e real index guiding) and pays particular attention to the efficiency of coupling power from such a device to an optical fibre. The degree of polarisation has been measured for SLDs, [1,6], however no attempt has been made to include it in a theoretical model. It has been the the aim of our research to develop a theoretical model for SLDs which includes all of the above mentioned characteristics.

The formulation of the model is kept very general so that it yields results for light/current characteristics, spectral distribution, far-intensity 'angular' distribution and polarisation while maintaining the longitudinal dependency of the inversion population. A new feature that is essential to the model is the use of a one dimensional (longitudinal) formulation which, however, still yields the angular distribution of the photon density in the lateral direction. Of course, this entails some approximations which slightly limits the accuracy with which the model predicts the angular distribution of the actual device, but the computational simplicity of this approach is particularly attractive. The spectral distribution is obtained by the inclusion of a wavelength dependency of the local gain and the spontaneous emission. These distributions are calculated from the basic semiconductor band structure as outlined in section (3.6). It is necessary to have a realistic representation of these quantities because, unlike semiconductor lasers, there is no sharp lasing linewidth but rather a broad spectra which, however, does narrow quite considerably with increasing current and/or stripe length.

A general description of the principles involved in developing the SLD model are given in section(4.2). This is followed by the actual formulation of the one-dimensional (longitudinal) photon and charge conservation equations in sections(4.3) and (4.4) respectively. It is these equations together with the boundary conditions, described in section(4.5), that form the basis of the model. The numerical procedure for solving these equations subject to the appropriate boundary conditions is outlined in section(4.6). The chapter ends with a brief summary of the SLD model in section(4.7).

4.2 General description of the SLD model.

The SLD structure, fig (1.1a), that is considered in this model is constructed of double-heterostructure material that provides not only carrier confinement to the active layer but also acts as a slab dielectric waveguide to the electromagnetic (optical) radiation, fig(4.1a). It was shown in section (3.31) that the typical thickness ($\cong$ 0.3μ) of the active layer and the refractive index difference ($\Delta n/n \cong 5\%$) between the active and cladding layers allows only one set of bound modes, the fundamental TE and TM, for a symmetric slab waveguide, to propagate along the active layer. The confinement factor for these modes can be obtained by either, solving the symmetric slab waveguide problem outlined in section (3.4) and using equations (3.54) and (3.57), or more easily by utilising the approximations of Botez [7,8], equations (3.55) and (3.58). The gain of each mode is then effectively obtained by multiplying the local gain, derived in section (2.6), with it's corresponding confinement factor. In the plane of the active layer, however, scalar plane wave (ray optics) propagation is considered.

It is assumed that the spontaneous emission is radiated isotropically, such that the fraction

$$\delta_s = 2\phi_c \delta\theta \qquad (4.1)$$

is directed into the angular range $2\phi_c$ in the direction perpendicular to the junction ('y' direction), fig(4.1a), and into the angular range $\delta\theta$ in the plane of the junction, fig(4.1b). ϕ_c is the critical angle for total internal reflection and is defined as

$$\phi_c = \cos^{-1}(n_2/n_1) \qquad (4.2)$$

where n_1 and n_2 are the refractive indices of the active and passive

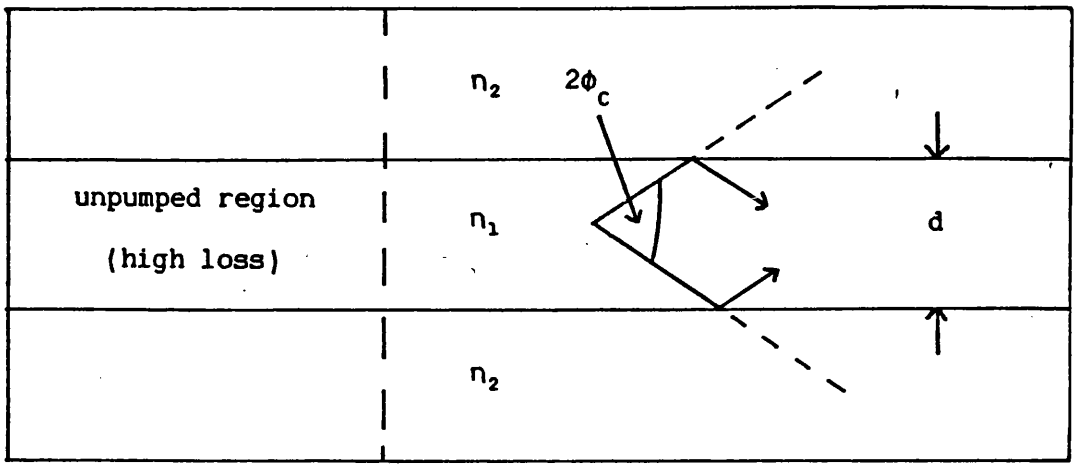

a) side view

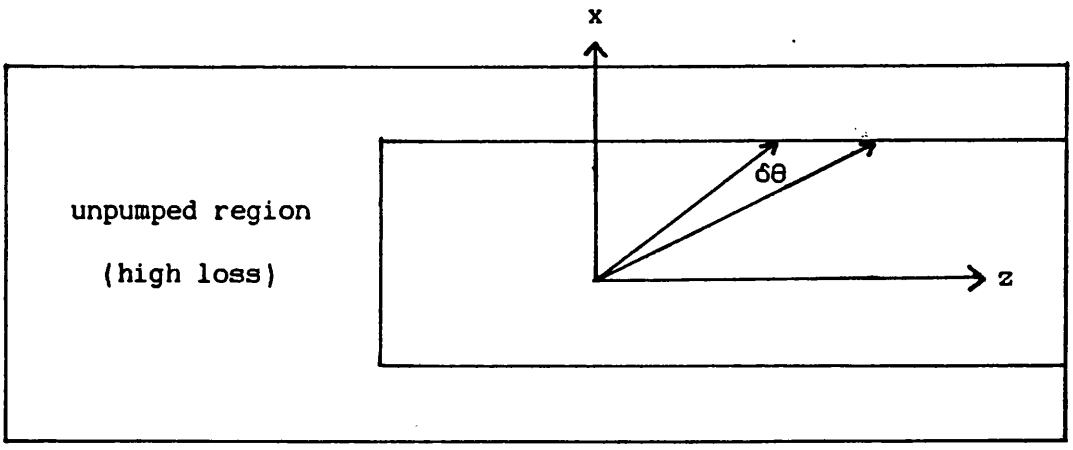

b)top view

Fig(4.1) Schematic diagram of the active layer of an SLD:
a) side view, b)top view.

layers respectively, fig(4.1a).

The equations that are used to formulate the SLD model are obtained by enforcing the physical requirements of photon and charge carrier conservation. The charge carrier conservation equation is developed by including terms for the electrical pumping, stimulated emission and spontaneous emission. The photon conservation equations, in particular include the angular distribution of the photons in the plane of the active layer. This particular feature is included in such a manner that the final form is still a one dimensional equation. The formulation assumes steady state conditions, $\delta/\delta t = 0$, and plane waves (ray optics) in the (x,z) plane of the junction.

4.3 The photon conservation equation.

Let plane waves of 'type-k' propagating in any arbitrary direction in the plane of the active layer be represented by a photon density $P_k(u,v)$, fig (4.2), where u is the direction of propagation of the plane wave with velocity c. Here and henceforth 'type-k' indicates any property of the photon which is necessary in applying the concept of the corresponding stimulated gain, $G_k(N)$, to the wave, e.g wavelength, polarisation etc. The use of the transverse co-ordinate 'v' in $P_k(u,v)$ is meant to indicate approximately plane waves having intensities dependent on 'v' but not coherently related. The conservation of 'type-k' photons propagating in the direction 'u', fig(4.2), can be represented by the equation

$$c.\frac{\delta P_k(u,v)}{\delta u} = G_k(N).P_k(u,v) + \delta_{sk}.R_{spon}(\lambda,N) \qquad (4.3)$$

where $N = N(u,v)$. This is simply a stationary form of the travelling wave rate equation so often referred to in the literature, eg [9,10].

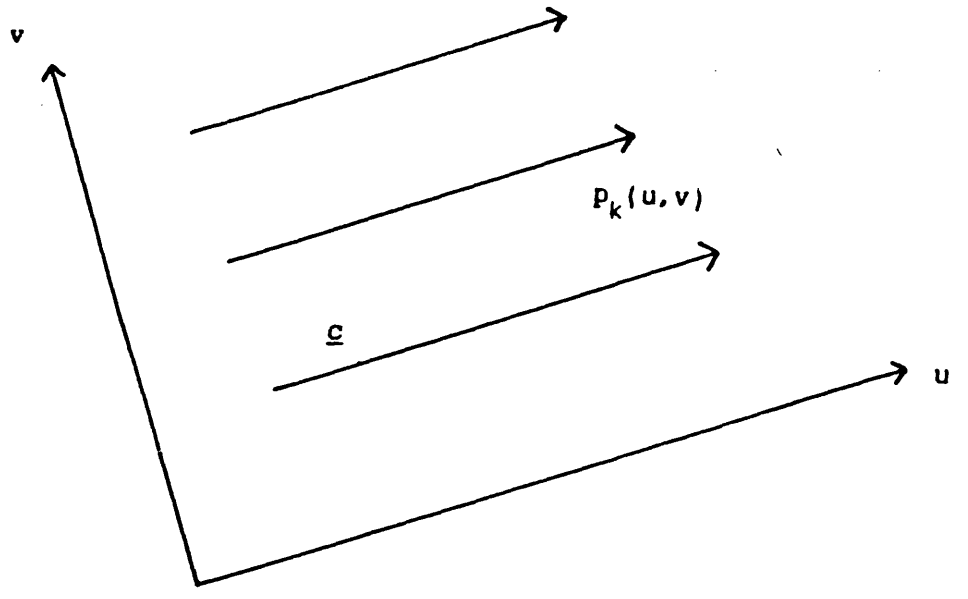

Fig(4.2) Photons propagating in an arbitrary direction 'u' with velocity '$\underline{c}$'

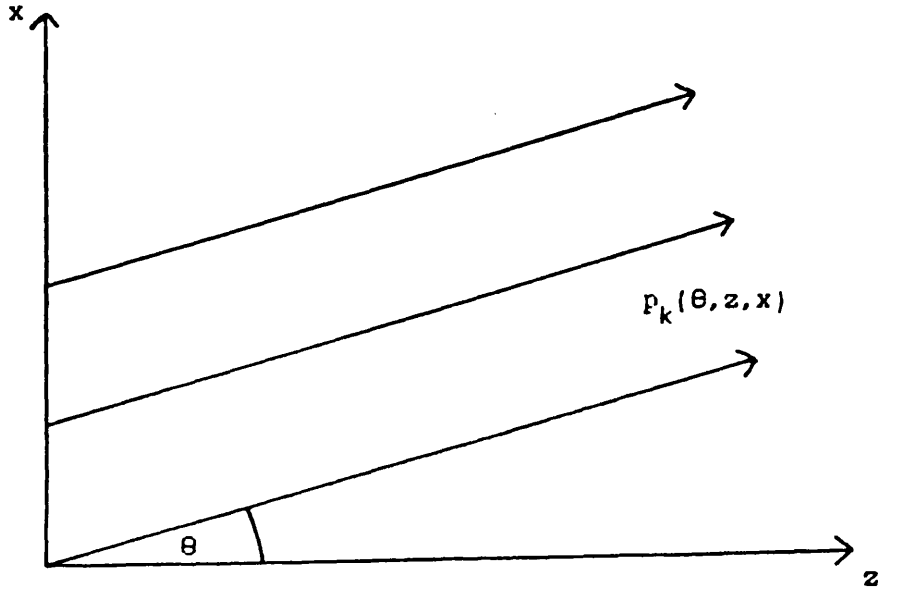

Fig(4.3) Photons propagating in an arbitrary direction 'u' in an x,z coordinate system.

The spontaneous emission term in equation (4.3) consists of two terms; δ_{sk}, which represents the fraction of spontaneous emission propagating in direction 'u', and $R_{spon}(\lambda,N)$ which indicates the wavelength distribution of the photons at an inversion population N. Note that to keep the analysis general the suffix k is added to δ_s to indicate the ammount of spontaneous emission that is emitted into each of the polarisations, which is not necessarily equal, [11,12]. The modal gain, G(N) is explicitly related to the local gain g(N) by

$$G_k(N) = \Gamma_k[g_k(N) - F_c(2N + p_1)] - [1 - \Gamma_k]F_c p_2 \qquad (4.4)$$

,[13], where F_c is the free carrier absorption constant ,Γ_k is the confinement factor and p_1 and p_2 are the doping densities of the active and passive layers respectively.

Since rays of different angles with respect to the normal to the output facet are required for the far-intensity angular distribution it is most convenient to use the independent variables 'z' and 'x ', fig (4.3). The density of 'type-k' photons can then be written more explicitly as $p_k(\theta,\lambda,z,x)$, where 'k' now represents the polarisation only. It is convenient and also common practice to refer to waves as being incident on or reflected from the facets. Thus the angular range is restricted to $-\pi/2 \leq \theta \leq \pi/2$ by specifically refering to forward travelling waves 'f ' or reverse travelling waves 'r'. Hence $p_k(\theta,\lambda,z,x)$, $0 \leq \theta \leq 2\pi$ is equivalent to using $p_{fk}(\theta,\lambda,z,x)$ and $p_{rk}(\theta,\lambda,z,x)$, $-\pi/2 \leq \theta \leq \pi/2$, all angles being with respect to the positive directed z-axis. Thus for example, a forward travelling wave at an angle '+θ' provides a reverse travelling wave at an angle '-θ' upon reflection from a facet. The two dimensional photon flux, Q, associated with these photon densities are

$$Q_{fk}(\theta,\lambda,z,x) = c_\theta p_{fk}(\theta,\lambda,z,x) \qquad (4.5)$$

and

$$Q_{rk}(\theta,\lambda,z,x) = -c_\theta p_{rk}(\theta,\lambda,z,x) \qquad (4.6)$$

where $c_\theta = \hat{u}_z.c.\cos(\theta) + \hat{u}_x.c.\sin(\theta)$, c = constant, the speed of light in the medium, $\hat{u}_z$ and $\hat{u}_x$ are unit vectors along 'z' and 'x' respectively. Applying the two dimensional, (x,z), divergence on Q and equating this to the net photons generated under steady state conditions yields the equations in 'z' and 'x' corresponding to equation (4.3) as

$$c.\sin(\theta)\frac{\delta p_{fk}(\theta,\lambda,z,x)}{\delta x} + c.\cos(\theta)\frac{\delta p_{fk}(\theta,\lambda,z,x)}{\delta z} = G_k(\lambda,N).p_{fk}(\theta,\lambda,z,x) + \delta_{sk}R_{spon}(\lambda,N) \qquad (4.7)$$

and

$$c.\sin(\theta)\frac{\delta p_{rk}(\theta,\lambda,z,x)}{\delta x} + c.\cos(\theta)\frac{\delta p_{rk}(\theta,\lambda,z,x)}{\delta z} = -[G_k(\lambda,N).p_{rk}(\theta,\lambda,z,x) + \delta_{sk}R_{spon}(\lambda,N)] \qquad (4.8)$$

where $N = N(z,x)$ and $-\pi/2 \leq \theta \leq \pi/2$.

The photon conservation equations , stated above, take into account photons travelling in any direction at any point in the active layer. To solve these equations in this form would require an excessive amount of computation time. It is, however, possible to reduce the two-dimensional photon conservation equations into a one-dimensional form, which still maintains the angular dependence in the lateral direction. To do this it is necessary to make some simplifying approximations. It is assumed that the current injecting stripe contact produces a rectangular shaped pumped region in the

active layer, fig(4.4). This approximmation amounts to neglecting current spreading effects and diffusion as being negligible and is certainly reasonable for wide striped SLDs. The boundaries of the rectangular region are $0 \leq x \leq w$ and $0 \leq z \leq L$ with the output facet being at $z = L$. It is assumed in the model that outside the rectangular region, in the active layer, the material is infinitely absorbing to all the radiation and that within the rectangular region the inversion population, 'N', and hence the modal gain, $G_k(\lambda,N)$, are constant across the width, w, i.e

$$N(z,x) = \begin{cases} N(z) & , \ 0 \leq x \leq w \ , \ 0 \leq z \leq L \\ 0 & , \quad \text{elsewhere} \end{cases}$$

and (4.9)

$$G_k(\lambda,N) = \begin{cases} G_k(\lambda,N) & , \ 0 \leq x \leq w \ , \ 0 \leq z \leq L \\ 0 & , \quad \text{elsewhere} \end{cases}$$

From here-on this will be refered to as the 'hard edge' model.

The boundary conditions of the 'hard edge' model provide the basis for the reduction of the two-dimensional photon equations into the one-dimensional form required. It is evident from fig (4.4) that,say, forward travelling waves at an angle '+θ' to the z-axis will only remain totaly within the pumped region up to $z = L$ if they originate within the region defined by

$$0 \leq x \leq h_\theta(z), \quad \begin{cases} \text{for } 0 \leq z \leq L & \text{when } 0 \leq \theta \leq \theta_f \\ \text{for } z \geq (L - w.\cot|\theta|) & \text{when } \theta \geq \theta_f \end{cases}$$

where $h_\theta(z) = [w - (L - z)\tan(\theta)$ and $\theta_f = \tan^{-1}(w/L)$. Note that

$h_\theta = 0$ for $z \leq (L - w.\cot|\theta|)$ when $\theta \leq \theta_f$.

It is the appropriate sum of all such rays that will contribute to the far-intensity angular distribution at an angle '+θ' to the z-axis. It therefore seems most suitable to attempt to reduce the two-

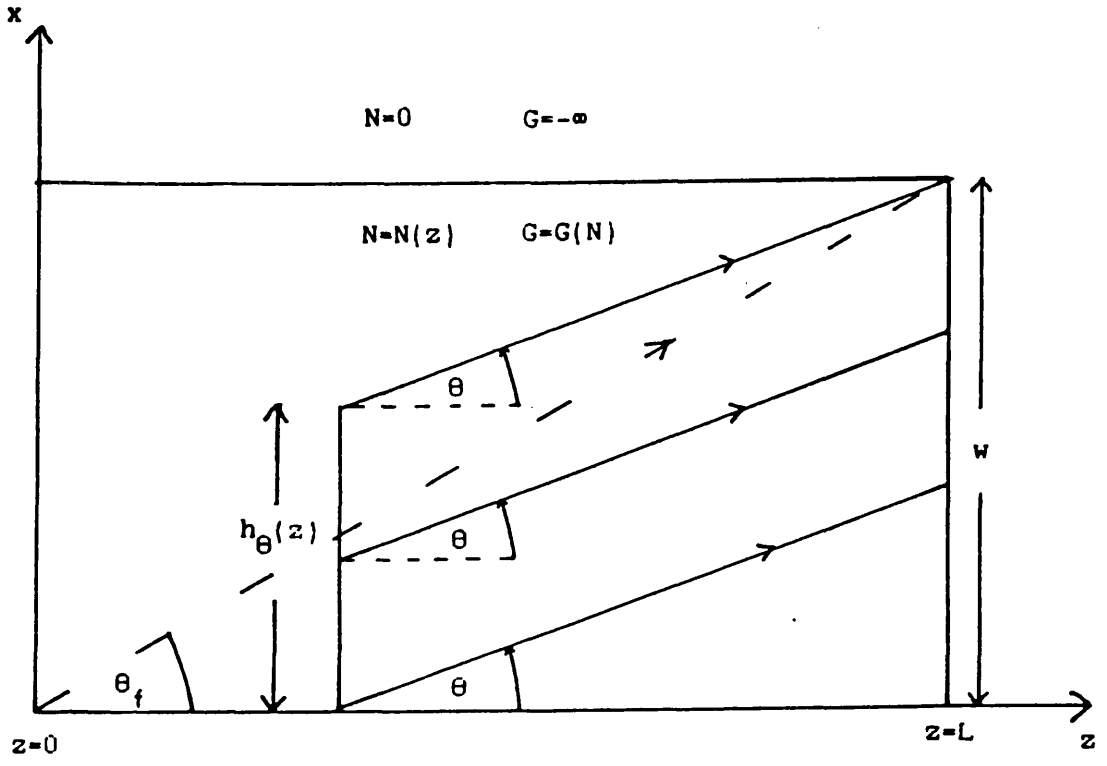

Fig(4.4) Schematic diagram of the pumped region of the SLD showing rays that remain totally within its boundaries up to z=L. This provides the basis for the definition of the average photon density.

dimensional problem into one dimension by defining an average photon density for $\theta \geq 0$ as

$$P_{fk}(\theta,\lambda,z) = \frac{1}{w}\int_0^{h_\theta(z)} \delta x.p_{fk}(\theta,\lambda,z,x) \qquad (4.10)$$

Differentiating equation (4.10) with respect to z yields

$$\frac{\delta P_{fk}(\theta,\lambda,z)}{\delta z} = \frac{1}{w}\int_0^{h_\theta(z)} \delta x.\frac{\delta p_{fk}(\theta,\lambda,z,x)}{\delta z} + \frac{\delta h_\theta(z)}{\delta z}.p_{fk}(\theta,\lambda,z,h_\theta(z)) \qquad (4.11)$$

On multiplying throughout by $c.\cos(\theta)$ and noting that $\delta h_\theta(z)/\delta z = \tan(\theta)$ the above equation becomes

$$\frac{c.\cos(\theta)}{w}\int_0^{h_\theta(z)} \delta x.\frac{\delta p_{fk}(\theta,\lambda,z,x)}{\delta z} = c.\cos(\theta).\frac{\delta P_{fk}(\theta,\lambda,z)}{\delta z} - \frac{c.\sin(\theta)}{w}.p_{fk}(\theta,\lambda,z,h_\theta(z)) \qquad (4.12)$$

and also

$$\frac{c.\sin(\theta)}{w}\int_0^{h_\theta(z)} \delta x.\frac{\delta p_{fk}(\theta,\lambda,z,x)}{\delta x} = \frac{c.\sin(\theta)}{w}.[p_{fk}(\theta,\lambda,z,h_\theta(z)) - p_{fk}(\theta,\lambda,z,0)] \qquad (4.13)$$

Applying the integral $\frac{1}{w}\int_0^{h_\theta(z)} \delta x$ to the left hand side, LHS, of equation (4.7) gives

$$LHS = c.\cos(\theta).\frac{\delta P_{fk}(\theta,\lambda,z)}{\delta z} - \frac{c.\sin(\theta)}{w}.p_{fk}(\theta,\lambda,z,0) \qquad (4.14)$$

$$= c.\cos(\theta).\frac{\delta P_{fk}(\theta,\lambda,z)}{\delta z}$$

which is obviously true for $\theta = 0$ but is also valid for $\theta > 0$ since $p_{fk}(\theta,\lambda,z,0) = 0$, because of the assumption in the model that no photons are generated outside the rectangular pumped region.

The same integral is then applied to the right hand side, RHS, of equation (4.7) and bearing in mind that the model assumes constancy of 'N' and 'G' in the region $0 \leq x \leq w$ it follows that

$$RHS = G_k(\lambda,N).P_{fk}(\theta,\lambda,z) + \frac{h_\theta(z)}{w}.\delta_{sk}R_{spon}(\lambda,N) \qquad (4.15)$$

therefore combining equations (4.14) and (4.15) gives the required one-dimensional form for the photon conservation equation

$$c.\cos(\theta).\frac{\delta P_{fk}(\theta,\lambda,z)}{\delta z} = G_k(\lambda,N).P_{fk}(\theta,\lambda,z) \qquad (4.16)$$

$$+ \left[1 - \frac{(L - z)}{w}.\tan|\theta|\right] \delta_{sk}R_{spon}(\lambda,N)$$

which is valid for $0 \leq |\theta| \leq \theta_f$ when $0 \leq z \leq L$

and for $|\theta| \geq \theta_f$ when $z \geq (L - w.\cot|\theta|)$

Note that $P_{fk}(\theta,\lambda,z) = 0$ for $|\theta| \geq \theta_f$ when $z \geq (L - w.\cot|\theta|$

The use of '$|\theta|$' in equation (4.16) is because the same form of equation is obtained for the corresponding '$-\theta$' rays. It is only necessary to solve equation (4.16) explicitly for $P_{fk}(\theta,\lambda,z)$, for $\theta > 0$ as the symmetry of the rectangular pumped region means that $P_{fk}(\theta,\lambda,z)$, for $\theta < 0$ is equal to that for $\theta > 0$, appendix (A1) and follows from recognising the symmetry of the photon density about $x = w/2$.

From equation (4.8) and by using similar definitions as was used for the average photon density for forward travelling waves, the reverse travelling waves are formulated by the equation

$$c.\cos(\theta).\frac{\delta P_{rk}(\theta,\lambda,z)}{\delta z} = -\{ G_k(\lambda,N).P_{rk}(\theta,\lambda,z) + [1 - \frac{z.\tan|\theta|}{w}]\ \delta_{sk}R_{spon}(\lambda,N) \} \qquad (4.17)$$

which is valid for $0 \leq |\theta| \leq \theta_f$ when $0 \leq z \leq L$

and for $|\theta| \geq \theta_f$ when $z \geq w.\cot|\theta|$

Note that $P_{rk}(\theta,\lambda,z) = 0$ for $|\theta| \geq \theta_f$ when $z \geq w.\cot|\theta|$

As with equation (4.16) equation (4.17) applies to $\theta \geq 0$ and $\theta \leq 0$ rays.

4.4 The charge carrier conservation equation.

In the theory of electric current flow, the equation of continuity expresses the condition that there is no accumulation of charge in a conducting medium. Semiconductors have different properties to conductors in that there is not only current flow to be considered but also the recombination of electron/hole pairs. The recombination processes can be divided into two types, radiative recombination, which result in the production of photons, and non-radiative recombination which does not. Radiative recombination can also be divided into two types, spontaneous and stimulated recombination. A more complete description of the radiative recombination processes is found in chapter (2).

The charge conservation equation is developed by including three terms, electric pumping, stimulated recombination and

spontaneous recombination, and may be written as

$$\frac{J_0}{qd} = \int_0^{\infty} \delta\lambda \sum_k \Gamma_k g(\lambda,N) \int_{-\pi/2}^{\pi/2} \delta\theta \, [p_{fk}(\theta,\lambda,z,x) + p_{rf}(\theta,\lambda,z,x)] + \frac{\int_0^{\infty} \delta\lambda . R_{spon}(\lambda,N)}{\eta_{eff}} \qquad (4.18)$$

where q is the charge on an electron, d is the active layer thickness and J_0 is the current density. There are a number of approximations involved in formulating this equation. Steady state conditions are assumed; equation (4.18) is, in fact, a stationary form of the charge carrier rate equation given in [9,10]. The current density is assumed to be constant throughout the rectangular striped region and to remain so throughout the different layers of the double-heterostructure material. This amounts to neglecting current spreading and the diffusion of carriers. It is also assumed that the current density is evenly distributed throughout the active layer thickness so that at the top of the active layer $J = J_0$ and at the bottom of the active layer $J = 0$, thus the carrier confinement to the active layer is total. The modal gain, '$G_k(N)$', given in equation (4.4) reduces to $\Gamma_k g(\lambda,N)$ in equation (4.18) because free carrier absorption does not give rise to band to band transition. Non-radiative transitions are taken into account by including η_{eff}, the radiative recombination coefficient, in the spontaneous emission term of equation(4.18). η_{eff} is defined by the equation

$$\eta_{eff} = \frac{R_{spon}}{R_{spon} + R_{nr}} \qquad (4.19)$$

where R_{nr} is the non-radiative recombination rate.

Equation (4.18) is in terms of the two-dimensional, (z,x),

photon densities, $p_{fk}(\theta,\lambda,z,x)$ and $p_{rk}(\theta,\lambda,z,x)$, and there is no averaging process that would permit this equation to be converted exactly into an equation in terms of the one-dimensional photon densities, $P_{fk}(\theta,\lambda,z)$ and $P_{rk}(\theta,\lambda,z)$. As the $\theta = 0$ rays have the largest photon density and therefore the largest effect on the inversion population, any averaging should at least be correct for these rays. Thus, equation (4.18) may be averaged by integrating both sides with $\frac{1}{w}\int_0^w \delta x$. Note that the integral only applies to $p_{rk}(\theta,\lambda,z,x)$ as all the other quantities in the equation are assumed independent of 'x' and hence remain unchanged by the integration. If $p_{fk}(\theta,\lambda,z,x)$ and $p_{rk}(\theta,\lambda,z,x)$ can be assumed to be approximately constant across 'x', and this is very nearly so for $|\theta| \ll \tan^{-1}(w/z)$ for forward travelling photons, and $|\theta| \ll \tan^{-1}(w/L-z)$, then for p_{fk} it follows from equation (4.10) that

$$\frac{1}{w}\int_0^w \delta x.p_{fk}(\theta,\lambda,z,x) \cong \frac{w}{h_\theta(z)}.P_{fk}(\theta,\lambda,z) = \frac{w.P_{fk}(\theta,\lambda,z)}{w - (L - z)\tan|\theta|} \qquad (4.19)$$

Similarly for reverse travelling photons

$$\frac{1}{w}\int_0^w \delta x.p_{fk}(\theta,\lambda,z,x) = \frac{w.P_{fk}(\theta,\lambda,z)}{w - (L - z)\tan|\theta|} \qquad (4.20)$$

Since equations(4.19) and (4.20) reduce to $P_{fk}(\theta,\lambda,z)$ and $P_{rk}(\theta,\lambda,z)$ for $\theta = 0$ and the averaging process used in deriving equations(4.19) and (4.20) is only strictly accurate when $\theta = 0$ it was decided to use $\frac{1}{w}\int_0^w \delta x.p_k(\theta,\lambda,z,x) \cong P_k(\theta,\lambda,z)$ in equation(4.18).

Next, remembering that $P_k(\theta,\lambda,z) = P_k(-\theta,\lambda,z)$ equation (4.18) may be

rewritten as

$$\frac{J_0}{qd} = \int_0^{\infty} \delta\lambda \sum_k \Gamma_k g(\lambda,N) \int_0^{\pi/2} \delta\theta\, 2[P_{fk}(\theta,\lambda,z) + P_{rf}(\theta,\lambda,z)] + \int_0^{\infty} \delta\lambda . \frac{R_{spon}(\lambda,N)}{\eta_{eff}} \qquad (4.21)$$

Finally this equation can be further simplified by making the approximation that

$$\int_0^{\infty} \delta\lambda . R_{spon}(\lambda,N) = B_r N^2 \qquad (4.22)$$

where B_r is the bimolecular recombination rate, section(3.6). Thus equation(4.21) becomes

$$\frac{J_0}{qd} = \int_0^{\infty} \delta\lambda \sum_k \Gamma_k g(\lambda,N) \int_0^{\pi/2} \delta\theta\, 2[P_{fk}(\theta,\lambda,z) + P_{rf}(\theta,\lambda,z)] + \frac{B_r N^2}{\eta_{eff}} \qquad (4.23)$$

The bimolecular recombination form for the total spontaneous emission is used to save excessive computation.

4.5 The boundary conditions.

The photon densities, $p_{fk}(\theta,\lambda,z,x)$ and $p_{rk}(\theta,\lambda,z,x)$, are in general, reflected from the facets at z = L and z = 0 respectively, fig(4.5). The resulting boundary conditions may be written as

$$p_{rk}(-\theta,\lambda,z=L,x) = R_k(|\theta|,\lambda,z=L).p_{fk}(\theta,\lambda,z=L,x) \qquad (4.24)$$

and

$$p_{fk}(-\theta,\lambda,z=0,x) = R_k(|\theta|,\lambda,z=0).p_{rk}(\theta,\lambda,z=0,x) \qquad (4.25)$$

where the facet reflectivities, R, are kept as general as possible by

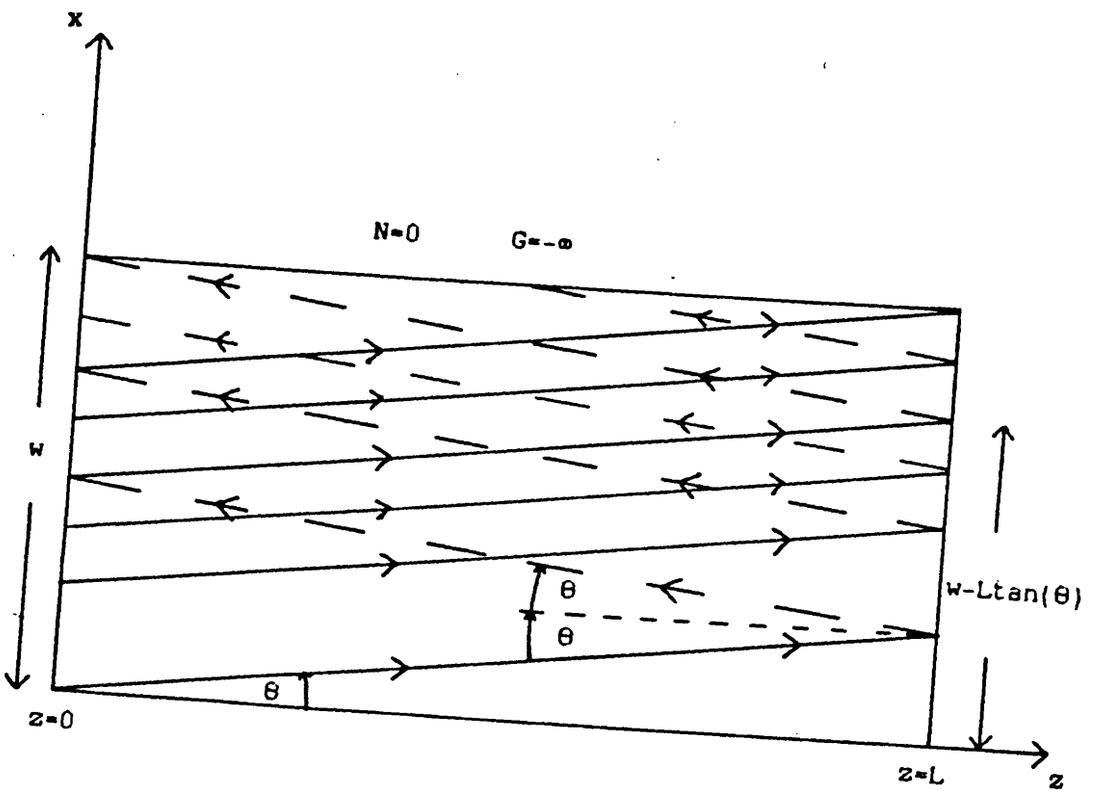

Fig(4.5) Schematic diagram of the active region of the SLD showing rays that are reflected from the front facet and remain totally within its boundaries up to z=0.

allowing for the possibility of wavelength and polarisation dependencies. It is convenient to use the notation

$$R_{kf}(|\theta|,\lambda) = R_k(|\theta|,\lambda,z=L) \quad \text{and} \quad R_{kb}(|\theta|,\lambda) = R_k(|\theta|,\lambda,z=L)$$

for the front and back facet reflectivities, respectively.

It can be seen from fig(4.5) that reflected rays only remain totally within the confines of the SLDs boundaries if they strike the facet within the region w-Ltan(θ). It is therefore necessary to average these rays over the whole width of the facet, w. This is done by applying the definition for the average photon density, equation (4.10), to equation (4.25) producing

$$P_{fk}(-\theta,\lambda,0) = \frac{1}{w}\int_0^{h_1} \delta x.p_{fk}(\theta,\lambda,0,x) = \frac{R_{kb}(|\theta|,\lambda)}{w}\int_0^{h_1} \delta x.p_{rk}(\theta,\lambda,0,x) \qquad (4.26)$$

where h_1 = w-Ltan(θ). Equation (4.26) may be rewritten as

$$P_{fk}(-\theta,\lambda,0) = \frac{R_{kb}(|\theta|,\lambda)}{w}\left[\int_0^{w} \delta x.p_{rk}(\theta,\lambda,0,x) - \int_0^{Ltan(\theta)} \delta x.p_{rk}(\theta,\lambda,0,x)\right] \qquad (4.27)$$

But note that

$$P_{rk}(-\theta,\lambda,0) = \frac{1}{w}\int_0^{w} \delta x.p_{rk}(\theta,\lambda,0,x) \qquad (4.28)$$

and if $p_{rk}(\theta,\lambda,0,x)$ can be taken to be almost independent of 'x', fig(4.6), then $p_{rk}(\theta,\lambda,0,x) \cong P_{rk}(\theta,\lambda,x)$ and on this basis

$$P_{fk}(-\theta,\lambda,0) \cong R_{kb}(|\theta|,\lambda).\left(1 - \frac{Ltan|\theta|}{w}\right).P_{fk}(\theta,\lambda,0) \qquad (4.29)$$

Now remembering that $P_k(\theta,\lambda,z) = P_k(-\theta,\lambda,z)$, from the symmetry of the

structure, equation (4.29) may be written as

$$P_{fk}(\theta,\lambda,0) = R_{kba}(|\theta|,\lambda).P_{rk}(\theta,\lambda,0) \qquad (4.30)$$

where the appropriate averaged reflectivity, (R_{kba}), is approximately

$$R_{kba}(|\theta|,\lambda) \cong (1 - \frac{L\tan|\theta|}{w}).R_{kb}(|\theta|,\lambda) \qquad (4.31)$$

Similarly the averaged front facet reflectivity is

$$R_{kfa}(|\theta|,\lambda) \cong (1 - \frac{L\tan|\theta|}{w}).R_{kf}(|\theta|,\lambda) \qquad (4.32)$$

and the boundary condition, equation(4.24) may be rewritten as

$$P_{rk}(\theta,\lambda,L) = R_{kfa}(|\theta|,\lambda).P_{fk}(\theta,\lambda,L) \qquad (4.33)$$

The assumption that $p_{rk}(\theta,\lambda,0,x)$ and $p_{fk}(\theta,\lambda,L,x)$ are almost independent of 'x' is a very good approximation for small 'θ', fig(4.6) i.e $|\theta| << \theta_f$ ($=\tan^{-1}(w/L)$), and since it is these rays that contribute the major part of the total photon density, the average reflectivities of equations(4.31) and (4.32) are the most suitable to use for a one-dimensional formulation.

For the SLD structure shown in fig (1.1a) the current injecting stripe contact extends all the way up to the front cleaved facet at z = L, the output facet, so that $R_{kf}(|\theta|,\lambda)$ is the typical reflectivity, $\cong 0.3$, for the active layer semiconductor, GaAs, to air interface. Note that for a more complete analysis the polarisation, 'k', see chapter(7), wavelength or angular dependencies may be included in R_{kf}. The 'back facet' reflectivity for the SLD, $R_{kb}(|\theta|,\lambda,0)$, is taken to be zero because the current injecting stripe contact, ending at z = 0, is far removed from any (real) cleaved back facet of the semiconductor chip. Consequently the

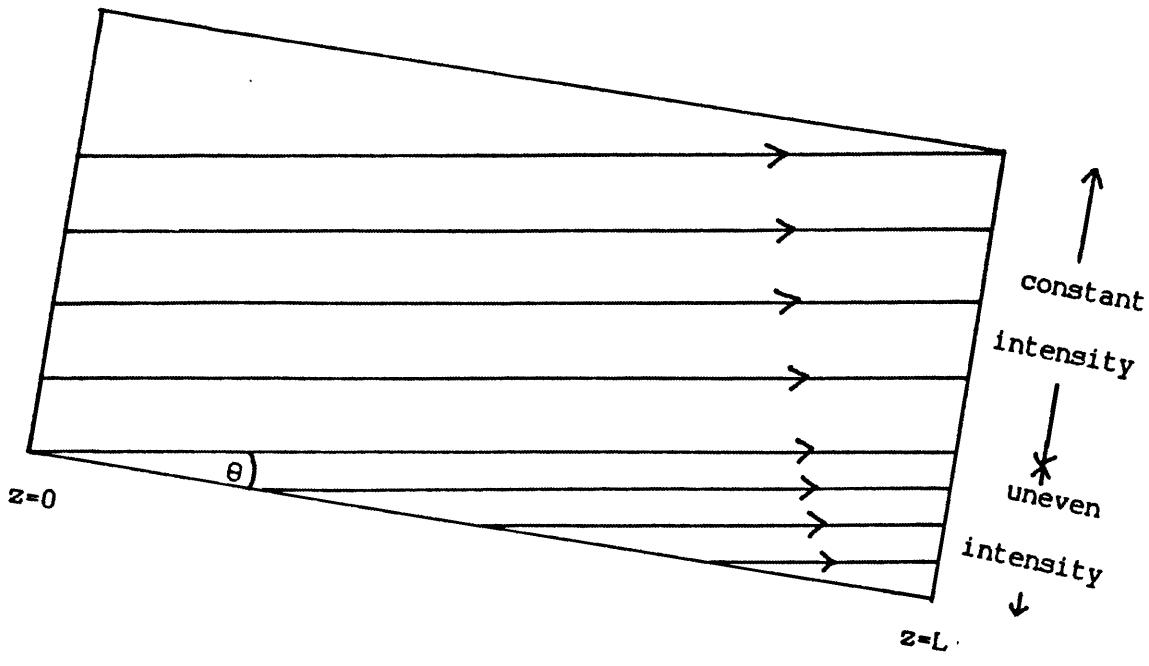

Fig(4.6) Schematic diagram of the active region of the SLD showing the intensity distribution of rays at the front facet.

reverse travelling photons of density $P_{rk}(|\theta|,\lambda,0)$ are totally 'lost' in the infinitely absorbing region of the active layer. However this model does allow for any specified value of $R_{kb}(|\theta|,\lambda)$ and therefore can be used to model the device structure of Wang et al, [6], where the stripe contact extends to both cleaved facets and anti-reflection coatings are used to suppress the 'lasing' feedback.

4.6 Numerical Method.

The numerical computation involves solving the set of first order ordinary differential equations, (4.16) and (4.17), for the photon densities, P_f and P_b, but which are coupled via the charge carrier conservation equation, (4.23). The photon densities must also satisfy the boundary conditions, equations (4.30) and (4.33), due to the facet reflectivities at the two ends, $z = 0$ and $z = L$, of the SLD.

Since the differential equations are of first order a step-by-step method of solving the equations is used. The boundary conditions at the two ends provide the test, after each 'run' along the length of the device, to decide whether a further iteration is necessary to attain the desired accuracy of solution. At a first glance it seems sensible to solve for both P_f and P_b at each longitudinal point, z, in a run irrespective of the stepping direction. This is obviously convenient because both P_f and P_b are required at each longitudinal point to calculate the inversion population. Problems can occur with this method, however, because the gain at certain wavelengths can change from positive to negative and the forward and reverse runs produce different photon distributions along the length. This error is avoided by solving only for P_f when stepping in the forward direction and P_b when stepping in the backward direction. Of course this then entails storing the values of

P_f and P_b at each longitudinal point so that their values are available for solving the carrier conservation equation, and adds considerably to the ammount of storage required when running the program.

The carrier conservation equation, (4.23), relating the inversion population to the photon densities, is not a simple function of N and is therefore solved iteratively by a 'step-halving' routine at each longitudinal point. The convergence of this method, for obtaining N at each point, is extremely fast because the starting value (zeroth iteration) is the solution at the previous longitudinal point in that run. This is especially true at low current densities where the inversion population varies little with longitudinal position.

The spontaneous emission and stimulated gain distributions, as functions of the inversion population, N, and wavelength, λ, are required in the course of self consistently solving the carrier conservation and photon conservation equations. These distributions are calculated numerically from quite involved equations derived from semiconductor physics, chapter(3), and for computational efficiency the two distributions are stored as data for forty values of λ and twenty values of N. The required values of spontaneous emission and stimulated gain, for any value of λ and N, are then obtained by using a cubic interpolation between the nearest stored points. It is worth noting that for any particular 'run' of the computer program the wavelength values are constant so that only a one dimensional interpolation in N is necessary to obtain the required values of spontaneous emission and stimulated gain.

In general, when running the program, a solution was found to be acceptable if the photon density in each wavelength slot, at

the front facet, changed by less than 0.1% from one iteration to the next. Tests were done at higher accuracies but the change in the photon densities was found to be insignificant. Tests were also done to ensure that, if the boundary condition at the front facet was satisfied, the photon density distributions along the length of the device in each wavelength slot remained unchanged for successive iterations. The accuracy for solving the inversion population at each individual point along the length was 0.05%. No significant change in the photon densities were found by increasing this accuracy. In the process of solving the first order differential equations, (4.16) and (4.17) for the photon densities, P_f and P_b, a step length $\cong$ 10μ was used. This value was decided on as a compromise between accuracy and computation time.

Section(4.7) Concluding Remarks.

A general model of the SLD has been developed. This has been achieved by using an approximate averaging that helps to reduce the two-dimensional photon and charge conservation equations to a one-dimensional (longitudinal) formulation that is still capable of producing the far-intensity (angular) distribution in the lateral direction. Also included in this model is a detailed representation for the wavelength dependency of the local gain and spontaneous emission so that it consequently yields a realistic spectral distribution for the SLD. A further feature of this model is the inclusion of polarisation dependent parameters allowing a comprehensive investigation into the polarisation properties of the SLD to be undertaken, see chapter (7).

References.

1) "A Stripe-geometry Double-heterostructure Amplified-spontaneous-emission (Superluminescent) Diode." T.P. Lee, C.A.Burrus, B.I. Miller. IEEE Journal of Quantum Electronics, vol QE-9, p.820, 1973.

2) "Superluminescent Diode as a Light Source in Optical Fibre Systems." M.C.Amann, W.Harth. Proceedings of the "Third European Conference on Optical Communication 1977".

3) "AlGaAs/GaAs Double-heterostructure Superluminescent Diodes for Optical Transmission Systems." J.Boeck, M.C.Amann. Frequenz, vol.33, p.278, 1979.

4) "On the Theory of the Superluminescent Diode, 1. Stationary Behaviour." J.Boeck, M.C.Amann, B.Segmuller

5) "Computer Model of a Superluminescent LED with Lateral Confinement." D.Marcuse and I.P.Kaminow, IEEE J. of Quant. Electron., vol.QE-17, p.1234, 1981.

6) "High-power Low-divergence Superradiance Diode." C.S.Wang, W.H.Cheng, C.J.Hwang, W.K.Burns, and R.P.Moeller, Appl. Phys. Lett. vol.41, 1 October 1982.

7) 'Analytic approximation of the radiation confinement factor for the TE_0 mode of a double-heterojunction laser', D.Botez, IEEE. J. of Quant. Electron., vol.QE-14, p.230, 1978.

8) 'Near and far-field analytic approximations for the fundamental mode in symmetric waveguide dh lasers', D.Botez, RCA Review, vol.39, p.577, 1978.

9) 'Longitudinal mode competition in semiconductor lasers. Rate equations revisited', M.J.Adams and M.Osinski, IEE PROC., vol.129, no.6, p.271, 1982.

10) 'Semiconductor lasers and heterojunction LEDs', H.Kressel and J.K.Butler, Academic Press, 1977.

11) 'Analysis of diode laser properties', W.Striefer, D.R.Scifres and R.D.Burnham, IEEE J. Quantum Electron., vol.QE-18, p.487, 1982.

12) 'Analysis of spontaneous emission effects on spectra and L vs I characteristics of diode lasers', W.Streifer, D.R.Scifres and R.D.Burnham, Jap. J. of Appl. phys., vol.21, p.L282, 1982.

13) 'Heterojunction lasers. Part B: Materials and operating characteristics', H.C.Casey, Jr. and M.B.Panish, Academic Press, 1978.

CHAPTER 5

A COMPARISON OF THE EXPERIMENTAL AND THEORETICAL CHARACTERISTICS OF SLDS

5.1 Introduction.

The main purpose of this chapter is to compare results obtained from the theoretical model of the SLD, described in chapter(4), with experimental measurements. With that aim the light/current characteristics, spectral distribution and far-intensity angular distribution of a number of SLDs were measured. The main difficulty in making a comparison between theory and experiment is in deciding what values of semiconductor material constants to use in the model. Certain parameters such as the doping densities and the aluminium contents of the active and passive layers are supplied by the manufacturers. Other parameters such as the bimolecular recombination coefficient and the bandtailing paramter are not so easily obtained. Experimental measurements for the bimolecular recombination coeficient, B_r, range between 0.6×10^{-11} and 1.3×10^{-10} $cm^3 s^{-1}$ for GaAs, [1-3], a sizeable variation. Since accurate values of such constants are not readily available for double-heterostructure laser material an alternative method of determining their values had to be found. The method chosen involved evaluating the unknown parameters by matching the theoretical light/current and spectral characteristics to the experimental results of an arbirtrarily selected SLD. Once determined these values were subsequently kept constant and used to predict theoretically the characteristics of the other measured devices.

The measurement techniques used to obtain the light/current, spectral and far-intensity characteristics of the SLDs are described in section(5.2). The basis for the comparison between theory and experiment is outlined in section (5.3) before proceeding to the actual results in sections(5.31-5.33). A brief summary is given in section(5.4).

5.2 Experimental Measurements

The optical output power, spectral distribution and far-intensity angular distribution were measured as a function of drive current for a number of SLDs. The experimental measurements, although fairly conventional, are described in detail, not only for completeness but also because they clearly indicate the basis for the comparison between experiment and theory.

When making measurements on SLDs (or lasers) it is essential to consider temperature effects. Internal heating arises in SLDs because of their small dimensions and the large currents used to drive them. fig(5.1) illustrates the difference that occurs in the light output characteristics when a typical SLD is operated over a range of different temperatures. These curves were produced under pulsed conditions using a temperature controlled mount, [4]. Rather than design and build a temperature controlled mount for the SLDs heating effects were kept to a minimum by using fast current pulses with low repetition rates to drive the SLDs. The pulses must be narrow enough so that the heating effect does not manifest itself during the pulse and consecutive pulses must be far enough apart to allow any heat generated to dissipate before the next pulse arrives. Throughout this project pulse widths in the range of 100-200ns with a duty cycle not exceeding 0.1% were used. These values are comparable

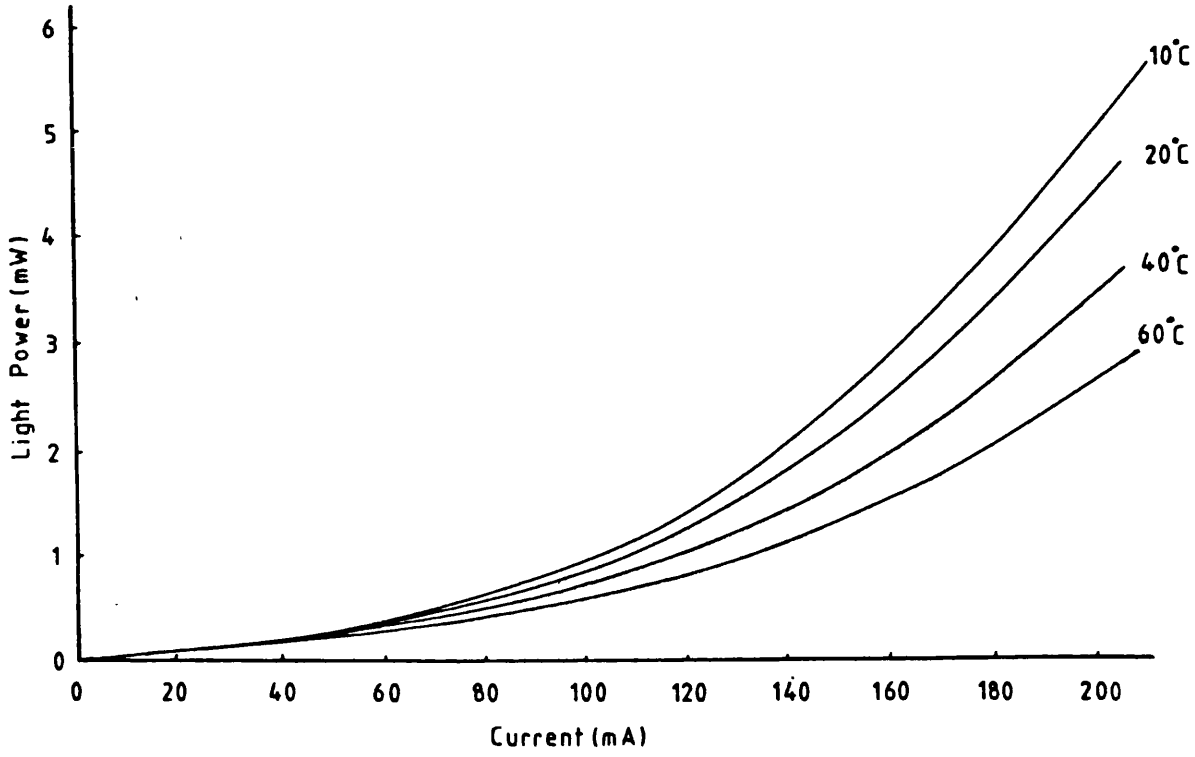

Fig(5.1) Variation of the light/current characteristics with temperature for a typical SLD.

with those quoted in the literature, [5,6].

5.21 Light/current charactristics.

The most commonly used method for measuring the total light power emitted from an SLD (or laser) is to place a large area photodiode very close to the SLD to ensure a very large collection angle. This however is not practical when using fast current pulses because large area photodiodes have slow response times. In fact the BPX65 PIN photodiode used in these experiments has an active area of only $1mm^2$ and hence an alternative method for making these measurements must be employed. This entails using the lens system shown in the schematic diagram, fig(5.2). Each item in this diagram is mounted on precision 'x,y, and z movements' to allow accurate positioning and focussing. Such mounts are essential because of the small size of the light emitting area of the SLD and the comparitively large distances between the SLD, lenses and detector. The front facet of the SLD is placed at the focal point of the 45 times magnification and 0.65 numerical aperture (x45 0.65NA) objective lens, the beam from which is then focussed down onto the detector by a x10 objective lens. The use of a high numerical aperture objective for the collection lens ensures a large collection angle. By this method a large fraction of the optical ouput from the SLD is detected by the small area, fast response, photodiode. The solid angle of collection, ϕ, is given by

$$\phi = 2.\sin^{-1}(NA/n) \qquad (5.1)$$

where n is the refractive index of the object space which in this case is air (=1) so that $\phi = 81^0$. Care must be taken to ensure that the intensity of light does not cause the photodiode to saturate. This can happen if the light is focussed down to a very small point

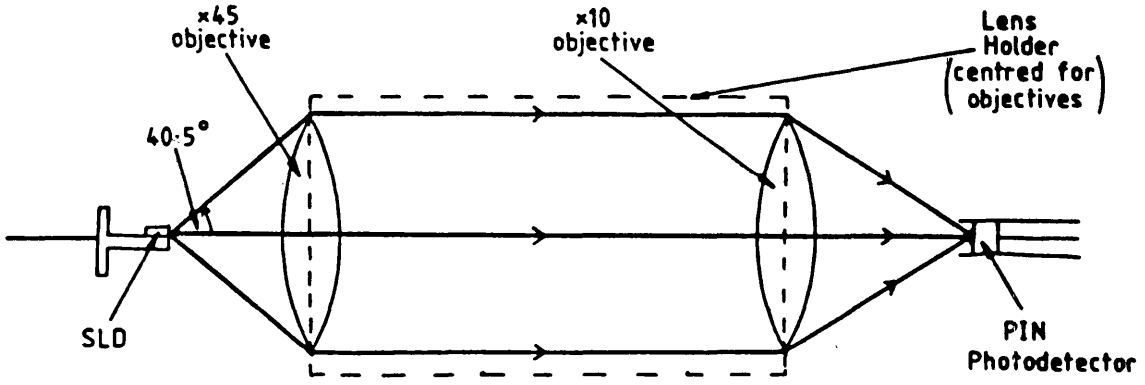

Fig(5.2) Schematic diagram of the light/current characteristic measurement system.

on the detector, and results in the output 'voltage' from the photodiode saturating. This can be corrected for by increasing the bias to the photodiode or by slightly defocussing the 'point' image on the photodiode.

5.22 Spectral distribution.

For the spectral measurements a monochromator (Spex Minimate) was placed between the two lenses, fig(5.3). In this case the x45 objective lens was used to produce the required image of the front facet at the entrance slit of the monochromator and the x10 objective to collect and focus the light from the monochromator onto the photodiode. The amount of light entering the monochromator was maximised by aligning the lateral direction of the SLD's active layer with the entrance slit. Before any measurements were made the monochromator was calibrated using a helium neon laser which radiates 'monochromatic' light at a wavelength of 632.8nm. Although the monochromator has a resolution of 1nm it was found to be sufficient to use the 2nm resolution slits since the measurements were carried out over a full range of typically 75nm. Even with this coarse resolution the light output within individual spectral slots was very small compared to the total output power, and particularly so at the extremities of the spectrum, to the extent that it was necessary to amplify the photodiode's output with a fast response pulse amplifier.

5.23 Far-intensity 'angular' distribution.

The far-intensity pattern (angular distribution in the lateral plane) was measured by a very direct method. For these measurements the small area photodiode was used not only as a fast detector but also to attain angular resolution. The small area

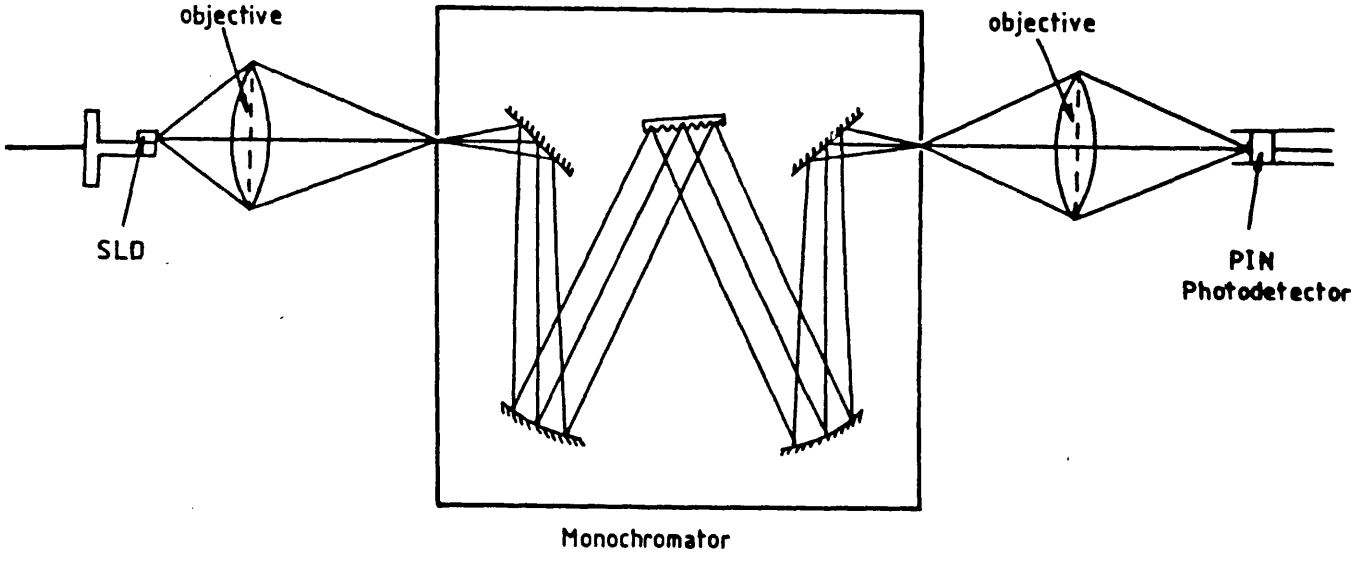

Fig(5.3) Schematic diagram of the spectral distribution measurement system.

photodiode (1mm x 1mm) was placed at a radial distance of 50mm on an arm which rotated about the output facet of the SLD. An angular resolution of about 1^0 was achieved with this arrangement, quite sufficient for these measurements. With this arrangement, however, the photodiode picks up only a very small fraction of the total emitted radiation and it was therefore necessary to improve the sensitivity of the detection system. The detection system was improved by designing a high frequency transistor amplifier for high gain and letting the amplified output be a linear ramp (integrated value) over the pulse width. Under these conditions, of course, neither the termination at the output of the amplifier nor the pulse width can be altered during a set of measurements.

5.3 Comparison of theoretical and experimental SLD characteristics.

The light output characteristics of six SLDs were measured and compared with theory. The SLDs all have different stripe contact lengths and originate from two different double heterostructure wafers. This provided the criteria for indexing them, table(5.1). The layer structure of the two wafers are almost identical, table(5.2), the only difference being that the aluminium content of the active layer of wafer (A) was measured by the device manufacturers and found to range between 6-8% across the wafer. No specific measured values were available for wafer (B).

The layer structure of the wafers provides the means of obtaining some of the necessary constants for the theoretical model. A numerical fit to experimental data for the refractive index of $Al_xGa_{1-x}As$ is given in [7] as

$$n(x) = 3.590 - 0.710.x + 0.091.x^2 \qquad (5.2)$$

TABLE(5.1)

SLD	WAFER	STRIPE		UNSTRIPED
		WIDTH(μm)	LENGTH(μm)	LENGTH(μm)
A207	A	28.0	207	171
A234	A	28.0	234	216
A291	A	28.0	291	184
A547	A	28.0	547	209
B180	B	20.8	180	207
B330	B	22.4	330	200(est)

TABLE(5.2)

LAYER	COMPOSITION	THICKNESS (μm)	DOPANT(TYPE AND DENSITY (cm^{-3})	REFRACTIVE INDEX
contact	p GaAs	1.6	1.0×10^{19} Ge	
passive	p $Ga_{0.7}Al_{0.3}As$	1.4	8.0×10^{17} Ge	3.38
active	p $Ga_{0.95}Al_{0.95}As$	0.3	4.0×10^{17} Si	3.55
passive	n $Ga_{0.7}Al_{0.3}As$	3.0	4.0×10^{17} Te	3.38
buffer	n GaAs	2.0	4.0×10^{17} Te	
substrate	n GaAs	-	1.2×10^{18} Si	

and gives the refractive indices of the active, n_1, and passive, n_2, layers as 3.55 and 3.38 respectively, table(5.2). When these values for n_1, and n_2 are inserted into equations (4.56 and 4.60) together with the active layer thickness, d = 0.3, they lead to an average value for the confinement factor, Γ = 0.74, for the fundamental mode. It should be noted that an average value is used as

no distinction is made between the TE and TM modes in this comparison.

Other parameters relating to the spontaneous and stimulated emission distributions are not so easily obtained because material properties vary from one semiconductor (DH) wafer to another and indeed, even across the same wafer. It seemed practical, therefore, to designate one of our devices as the 'master SLD' and to use it to detemine accurate values for the necessary semiconductor parameters. This was achieved by altering, within acceptable ranges, the radiative recombination constant, B_r, the band tailing parameter, η_c, and the bandgap energy, E_g, to obtain the best possible match between the theoretically computed light output characteristics and the experimental results for that particular device. It should be noted that B_r and η_c primarily alter the amplitude and the spectral width, repectively, of the spontaneous emission and stimulated gain, whereas small changes in E_g essentially shifts the whole spectral distribution. When the 'best match' is obtained for the 'master SLD' the same values for B_r and η_c are used in computing the light output characteristics of the remaining SLDs. The only parameters that remain are the stripe dimensions which vary from one device to another and the band gap energy, E_g. Small variations in the band gap energy are acceptable on the basis of the device manufacturer's measurement of the aluminium content of wafer (A) which, as mentioned above, ranges between 6-8%. If these values for the aluminium content of the active layer are substituted into the expression for E_g given in [7] for $Al_xGa_{1-x}As$ at 300K as

$$\begin{aligned} E_g &= 1.424 + 1.247.x && : 0.00 < x < 0.45 \\ E_g &= 1.424 + 1.247.x + 1.147.(x^2-0.45) && : 0.45 < x < 1.00 \end{aligned} \qquad (5.3)$$

a range of about 25meV is expected across the wafer. This range in E_g is considerably larger than the variation in E_g that is required to match the theoretical and experimental spectral characteristics for all the devices from wafer (A).

Following the above arguments the SLD A291 was chosen as the 'master SLD'. The best match between theory and experiment was obtained with $B_r = 1.0 \times 10^{-10} cm^3 s^{-1}$, $n_c = 0.024eV$, and $E_g = 1.45eV$, which results in the spontaneous emission and stimulated gain curves shown in fig (5.4). With these values thus established and taking a value of unity for the recombination efficiency, the far-intensity distribution is predicted by the model for a given stripe contact width and length. A complete list of all the parameters used in the model is compiled in table (5.3).

TABLE(5.3)

ABREV	PARAMETER	VALUE
R_f	front facet reflectivity	0.3
R_b	back facet reflectivity	0.0
B_r	bimolecular recombination constant	$1 \times 10^{-10} cm^3 s^{-1}$
F_{cc}	free carrier absorption constant	$5 \times 10^{-16} cm^2$
n_c	bandtailing parameter	0.024eV
E_g	band gap energy	1.45eV
Γ	confinement factor	0.74
p_1	active layer doping density	$4 \times 10^{17} cm^{-3}$
p_2	cladding layer doping density	$4 \times 10^{17} cm^{-3}$
n_1	active layer refractive index	3.55
n_2	cladding layer refractive index	3.38

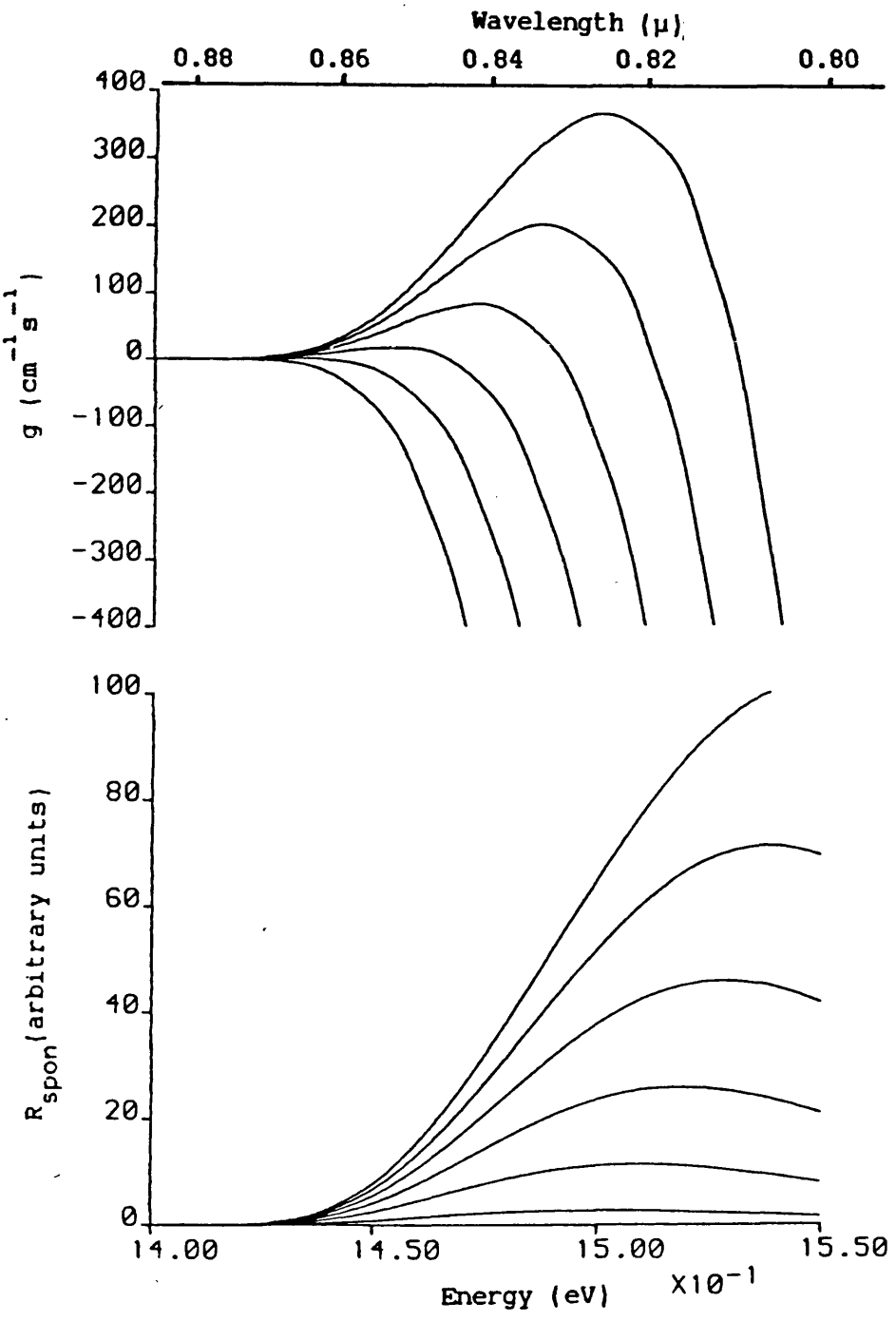

Fig(5.4) Local gain, g, (top) and spontaneous emission rate, R_{spon}, (bottom) v energy for various values of inversion population. $B_r = 1.0 \times 10^{-10}$ cm^3 s^{-1} and $\eta_c = 0.6$ eV.

5.31 Light/current characteristics.

Theoretical results for the light/current characteristics of the remaining SLDs were obtained using the same parameters in the model as were used for the 'master SLD'. Note that, althougth small changes in the bandgap are necessary to superimpose the theoretical and experimental spectra the effect of those changes on the light/current characteristics is negligible. The comparison between theoretical and experimental results for all six SLDs are shown in figs (5.5-5.7), the solid and dashed curves representing theoretical calculations and the symbols indicating experimental measurements. In these graphs the output power is normalised to mW/20μ stripe width and current density is used rather than current. This permits the increase in optical output that occurs with device length to be seen more easily. It can be seen from these graphs that three SLDs, A547, B330 and the 'master SLD', A291 show good agreement between theory and experiment, over a large range of current densities, while the remaining three devices, A207, A234, and B180 do not. This is not suprising given the accuracy and uniformity to which the double-heterojunction wafers, that devices such as SLDs and lasers are made from, can be manufactured. Other factors such as degradation and bad contacting also produce variability in the quality of devices. It is possible, however to obtain a reasonably good match between theory and experiment for SLDs A207 and B180 by altering the radiative recombination efficiency. Defects in the semiconductor causing non-radiative recombination sites would be the primary reason for having fractional values for the radiative recombination efficiency. The dashed curves in figs (5.5) and (5.7) show the results of calculations for SLDs A207 and B180 with radiative recombination

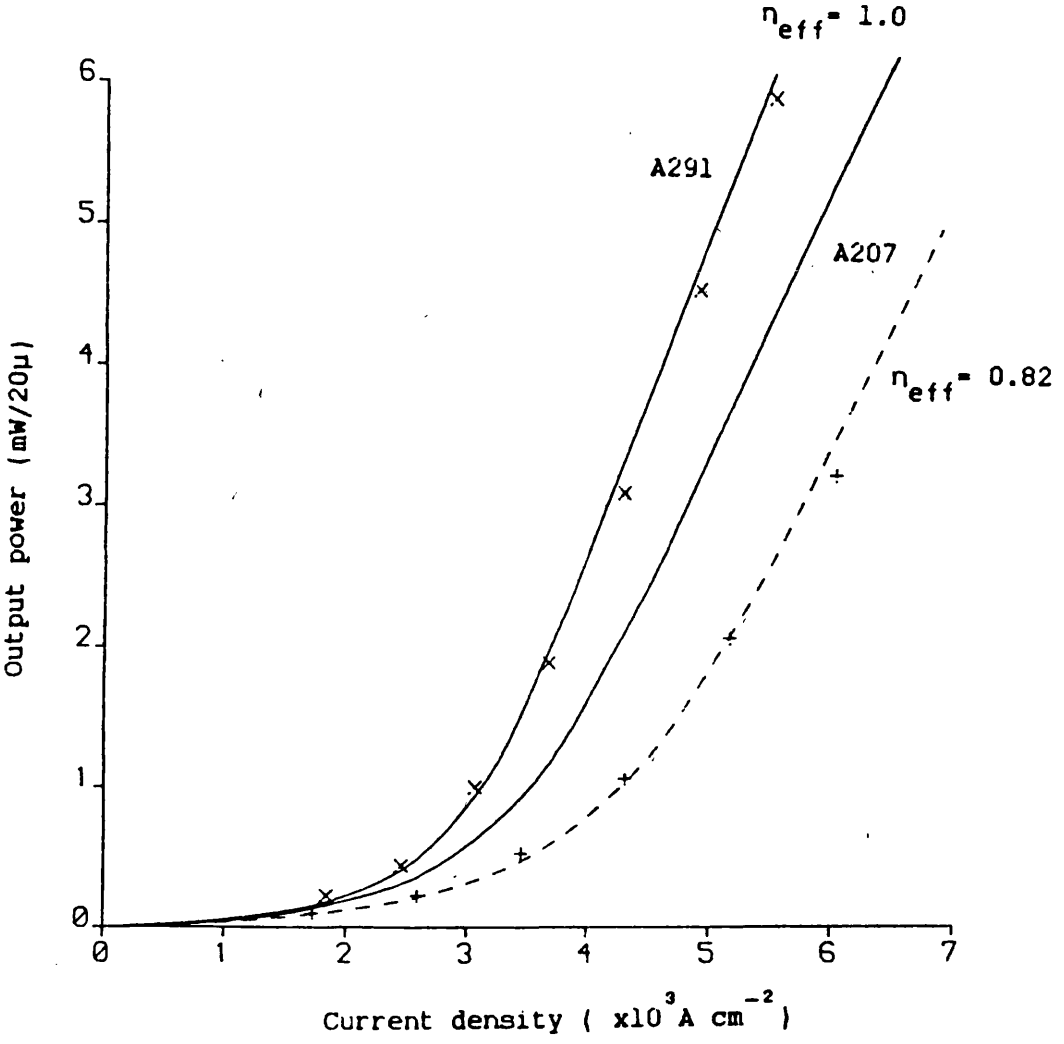

Fig(5.5) Comparison of theoretical and experimental light/current characteristics for SLDs A291 and A207.

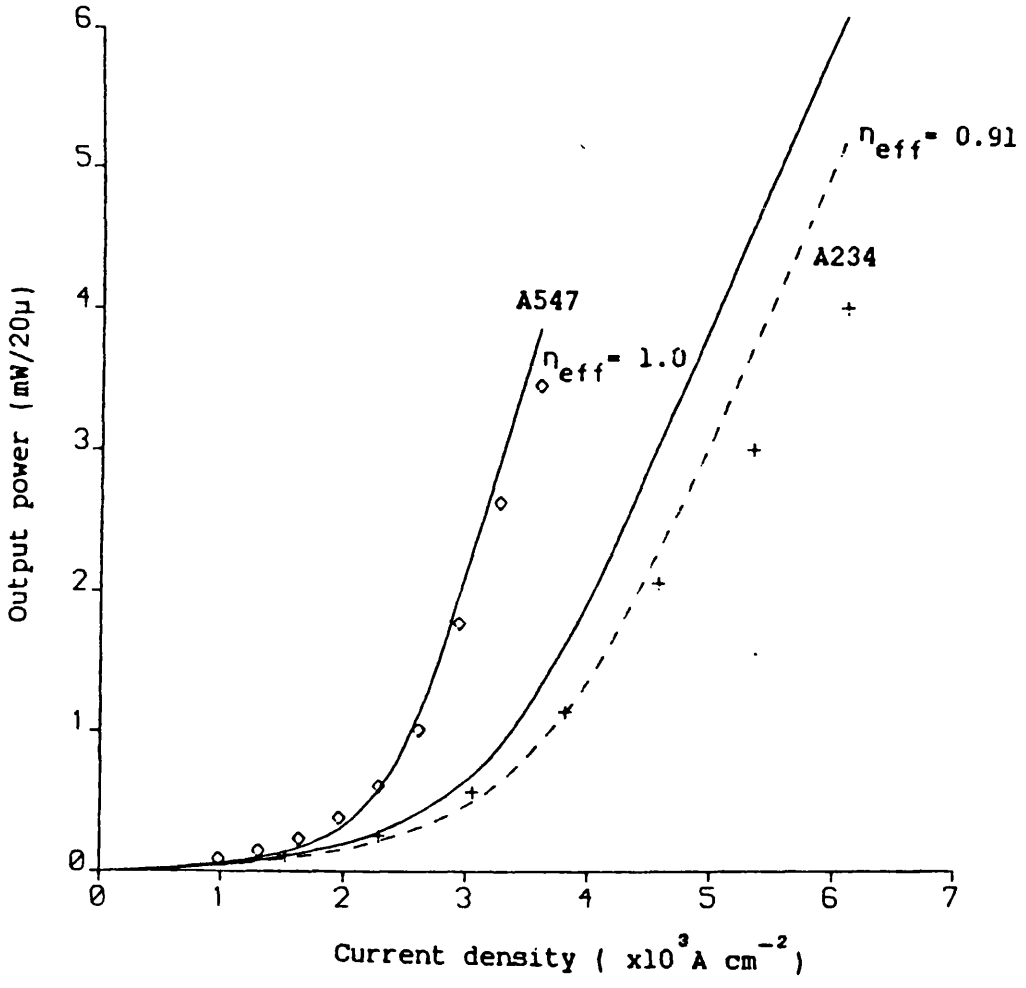

Fig(5.6) Comparison of theoretical and experimental light/current characteristics for SLDs A547 and A234.

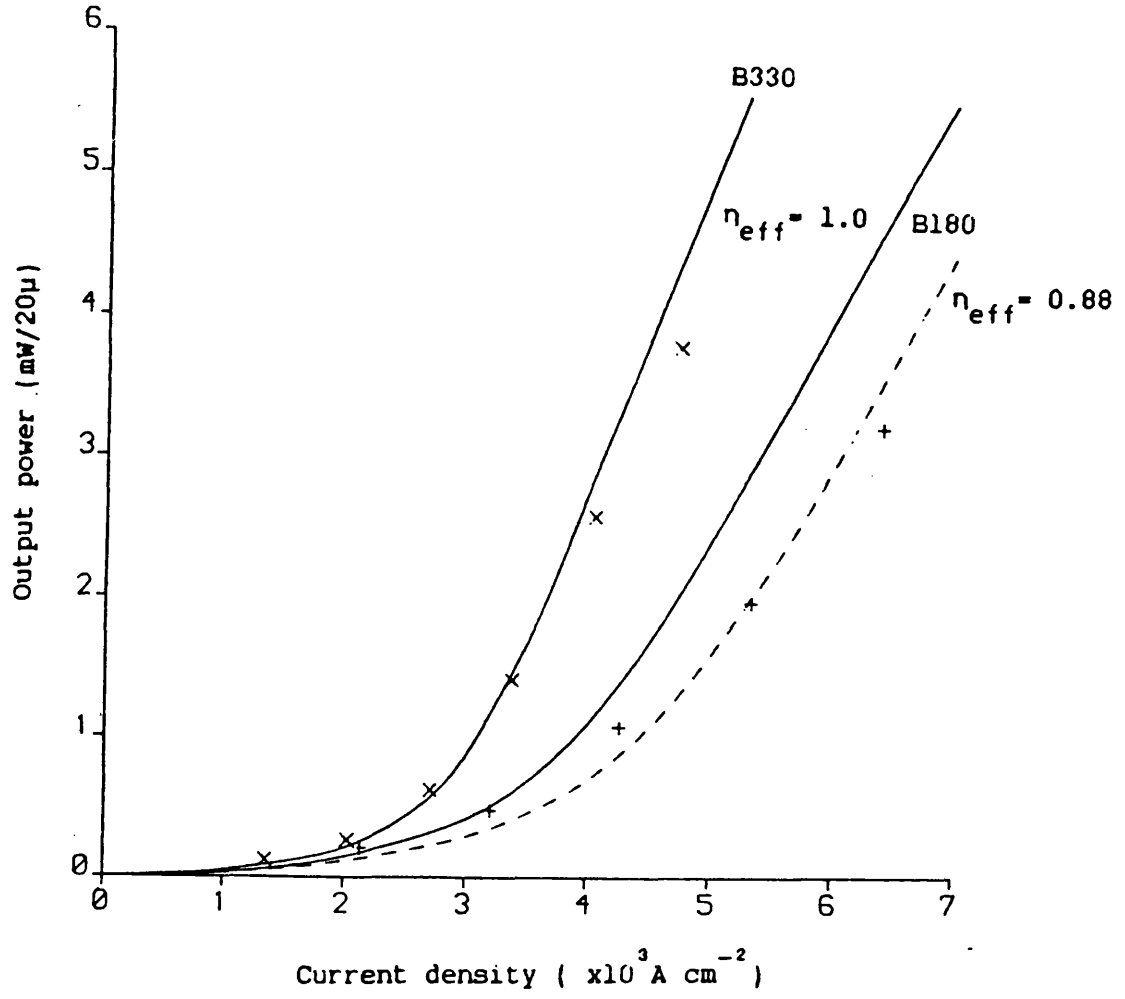

Fig(5.7) Comparison of theoretical and experimental light/current characteristics for SLDs B180 and B330.

efficiencies of 0.82 and 0.88 respectively. In the case of SLD A234, although an improved match is obtained if the recombination efficiency is reduced from 1.0 to 0.91, fig(5.6) the slopes of the curves have somewhat different trends. This would seem to indicate that some factor(s) other than just the recombination efficiency must be accounted for if a more satisfactory match between theory and experiment is to be obtained for this particular SLD. It is pertinent to point out that the far-intensity pattern observed for this SLD, fig(5.8) has a pronounced uncharacteristic double peak, at all current densities. This anomolous result could indicate facet damage explaining the difficulty in matching theory and experiment by altering the radiative recombination efficiency for this SLD.

5.32 Spectral distributions.

The theoretical and experimental spectral distributions for the SLD A291 are shown in fig(5.9). The agreement between the two sets of results are quite good but cannot be made perfect. The tendency is for the peak of the theoretical curves (solid lines) to move to higher energies at a faster rate than the peak of the experimental spectra (symbols). It is, however, believed to be the first time that such good agreement has been achieved over such a wide range of wavelengths and current densities.

The true test of the model is, of course, not it's ability to match the spectral characteristics of SLD A291, which was used to obtain the material parameters for the theoretical model, but it's ability to obtain agreement with the experimental results for the remaining SLDs. As mentioned in section(5.3) it was necessary to alter Eg in the model by small amounts to superimpose the theoretical results onto their corresponding experimental results. The actual

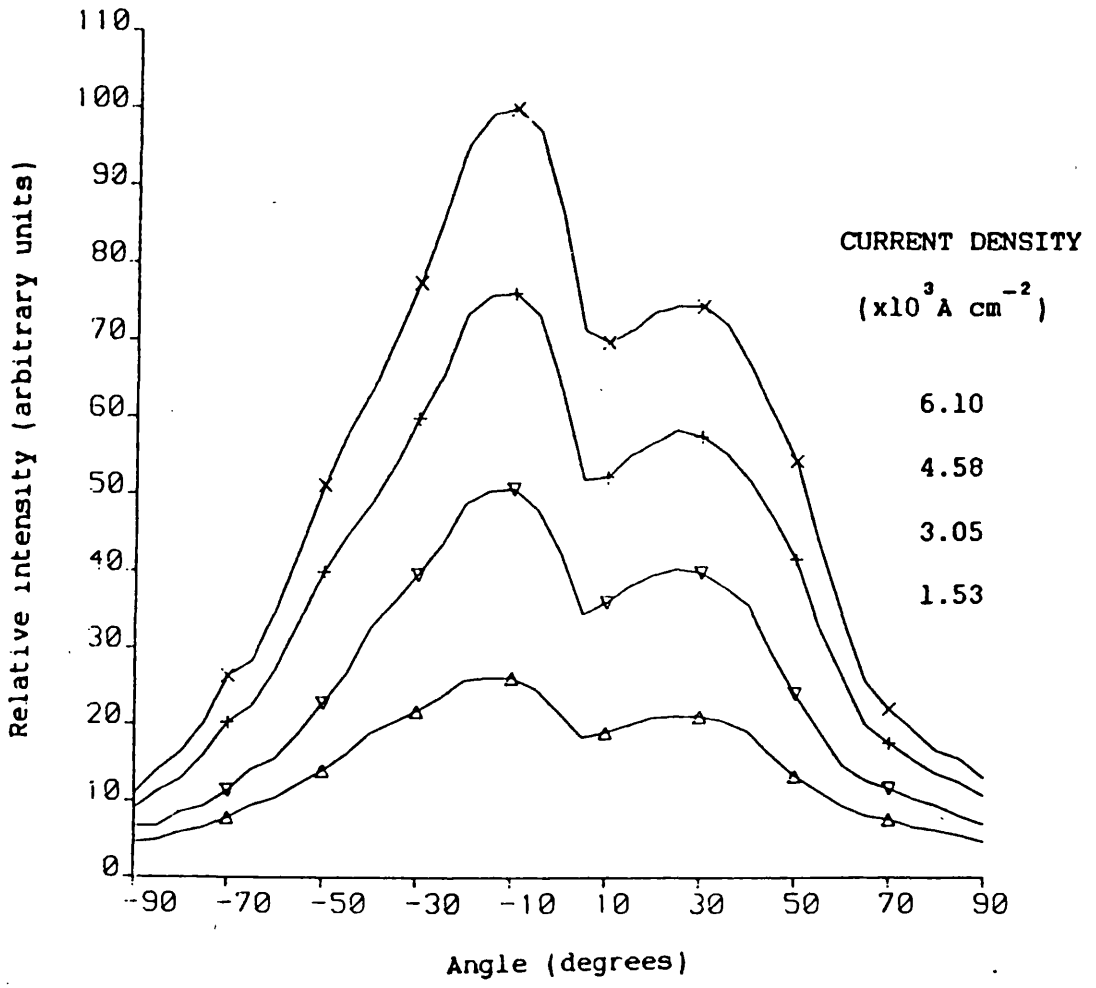

Fig(5.8) Experimental far intensity angular distribution for SLD A234 showing an unusual double peak at all current densities.

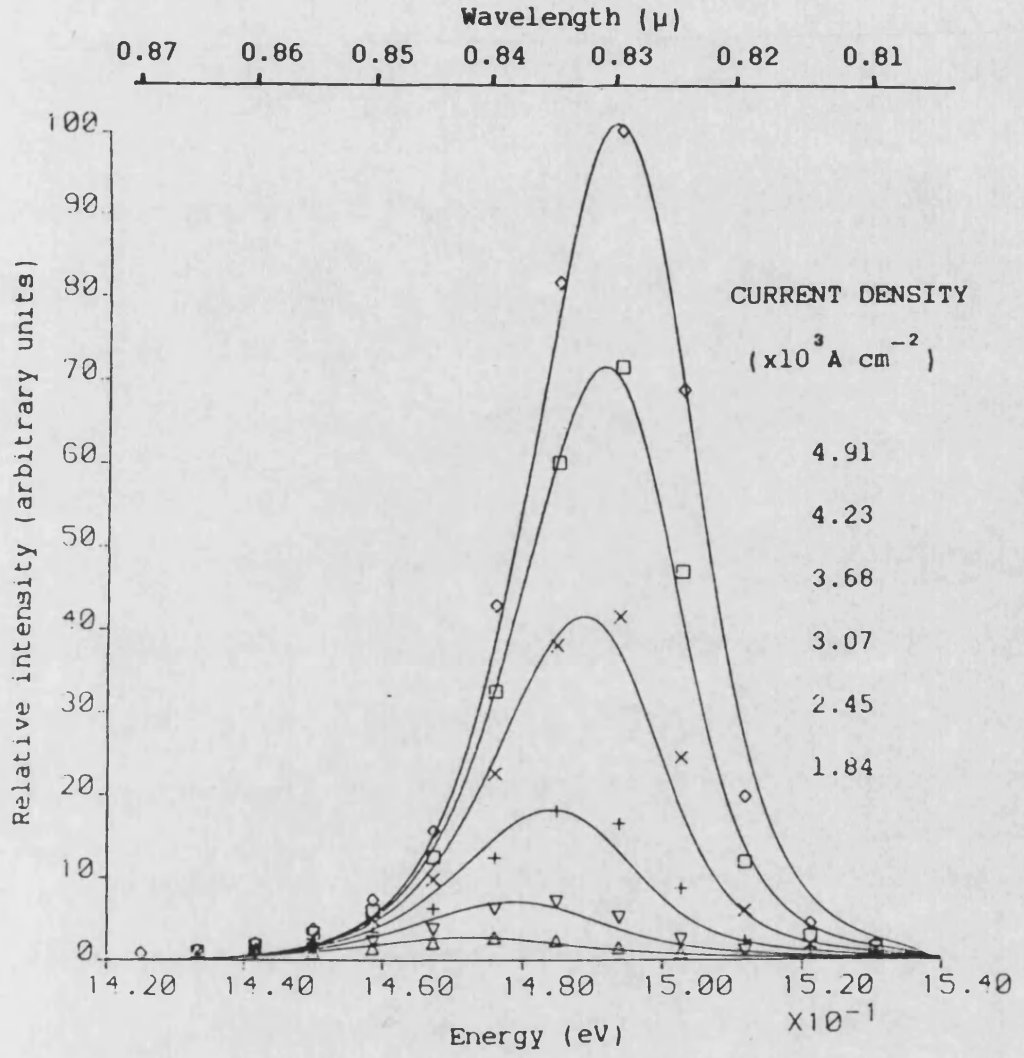

Fig(5.9) Comparison of the theoretical and experimental spectral distribution for SLD A291. Different curves correspond to different current densities.

change in Eg needed to do this is different for each device, table(5.4). The SLDs A547, A234 and A207 all required small changes in Eg to superimpose the theoretical and experimental curves, all well within the 25meV limit that a 6-8% variation in the aluminium content of the active layer would allow. The agreement between theory and experiment is remarkably good over a wide range of wavelengths and current densities. A typical example of the quality of the agreement between experiment and theory is shown in fig(5.10) for SLD A547. These devices all come from the same wafer as the 'master' SLD, A291.

TABLE(5.4)

SLD	CHANGE IN Eg (meV)	WAFER
A547	6.0	A
A234	13.0	A
A207	17.0	A
B180	63.0	B
B330	53.0	B

Devices from wafer B, however, needed larger changes in the bandgap energy to attain a match between theoretical and experimental results for SLDs B330 and B180, table(5.4). The theoretical spectra are also narrower than the experimental results for both of these SLDs. This is clearly shown in fig(5.11) for SLD B330. The descrepencies are primarily at the longer wavelengths suggesting that the semiconductor materials for the two wafers might have different bandtailing parameters. Certainly some of the material parameters

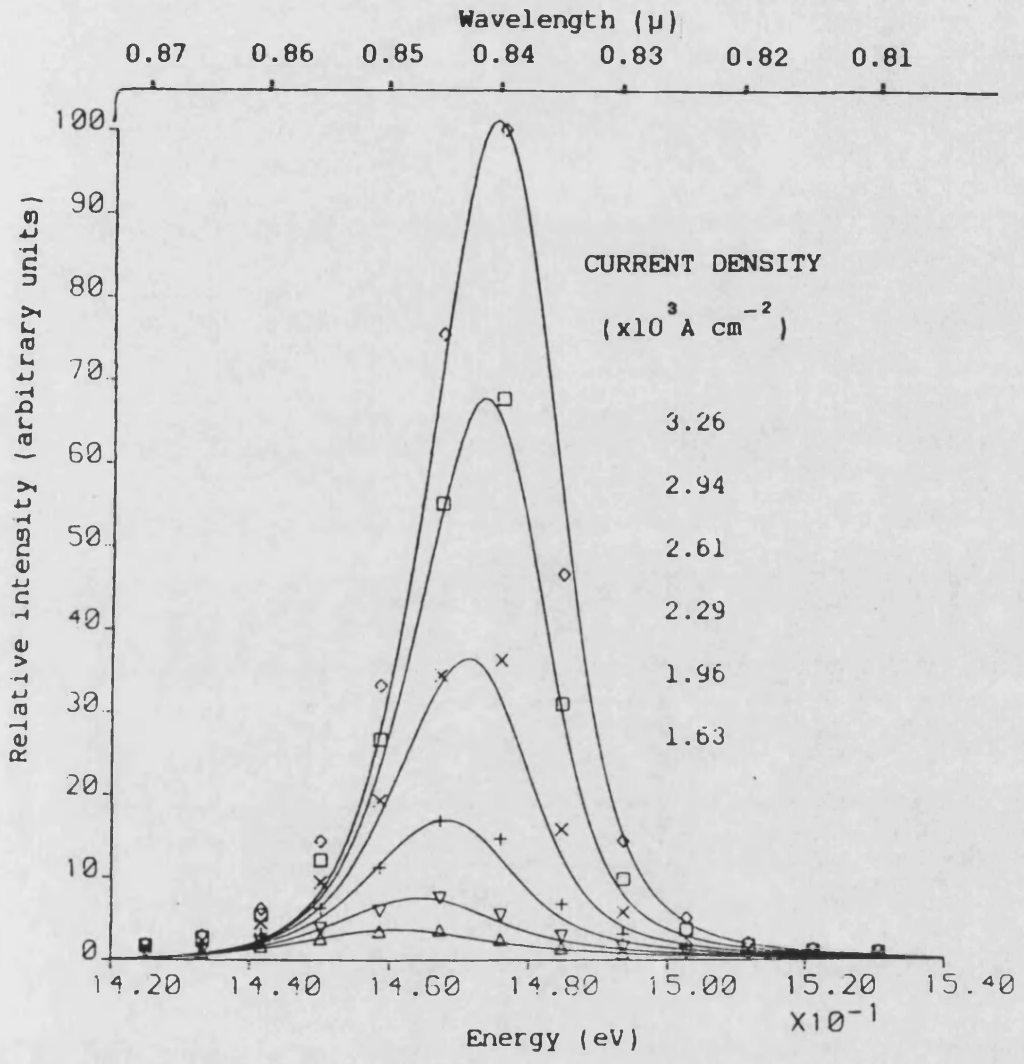

Fig(5.10) Comparison of the theoretical and experimental spectral distribution for SLD A547. Different curves correspond to different current densities.

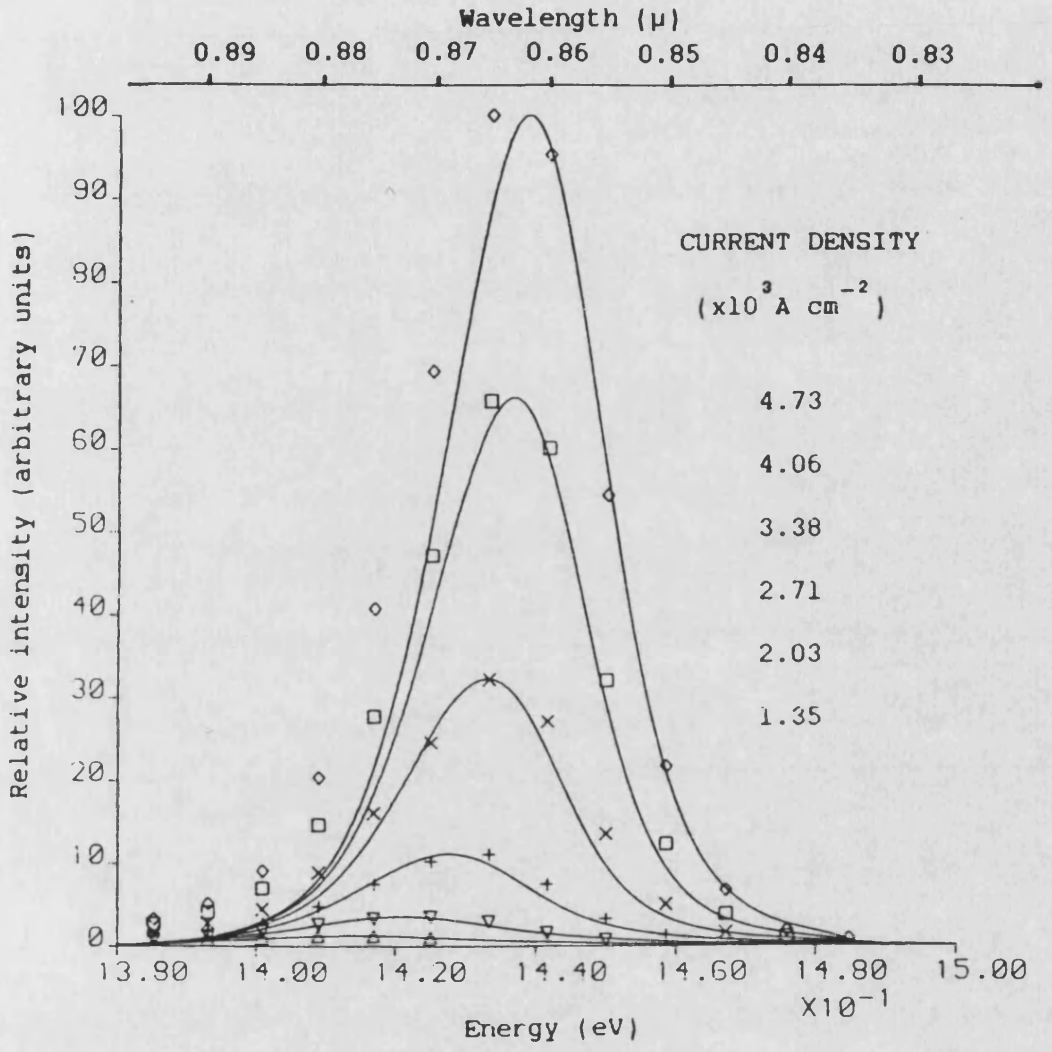

Fig(5.11) Comparison of the theoretical and experimental spectral distribution for SLD B330. Different curves correspond to different current densities.

must be different because the change in Eg needed to superimpose the theoretical and experimental spectra were much larger for wafer B than for wafer A. An attempt to obtain an improved spectral match by changing only the bandtailing parameter proved unsucessful because the light/current characteristic also changed. It is suggested that to obtain reasonable results for these SLDs the size and shape of the gain and spontaneous emission distributions would have to be tailored to suit one of the two devices from that wafer by altering both the recombination coefficient and the bandailing parameter. This exercise was not attempted because only one SLD would be available for comparison after empirically matching the spectral characteristics of the other device to obtain the material parameters.

5.33 Far-intensity distribution.

Theoretical far-intensity distributions are automatically generated by the SLD model as a result of the one-dimensional form obtained for the photon conservation equations. Two examples of how the computed and the experimentally measured far-intensity distributions compare are shown in figs (5.12) and (5.13), for SLDs A291 and A207 respectively. It is found that the theoretical results always predict a narrower far-intensity distribution than is obtained experimentally but the slopes of the curves are very nearly the same in the range of angles $0 < \theta < \theta_f$, $(\theta_f = \tan(w/L))$. This is a consequence of the 'hard-edge' model. It can be shown that the theoretical far-intensity distribution has a linear dependence on θ, (to a very good approximation), for $0 < \theta < \theta_f$, Appendix (A2). It is for this reason that the computed far-field intensity distributions are discontinuous at $\theta = 0$ and the characteristic triangular shaped peak occurs. These triangular shaped peaks remain even at high

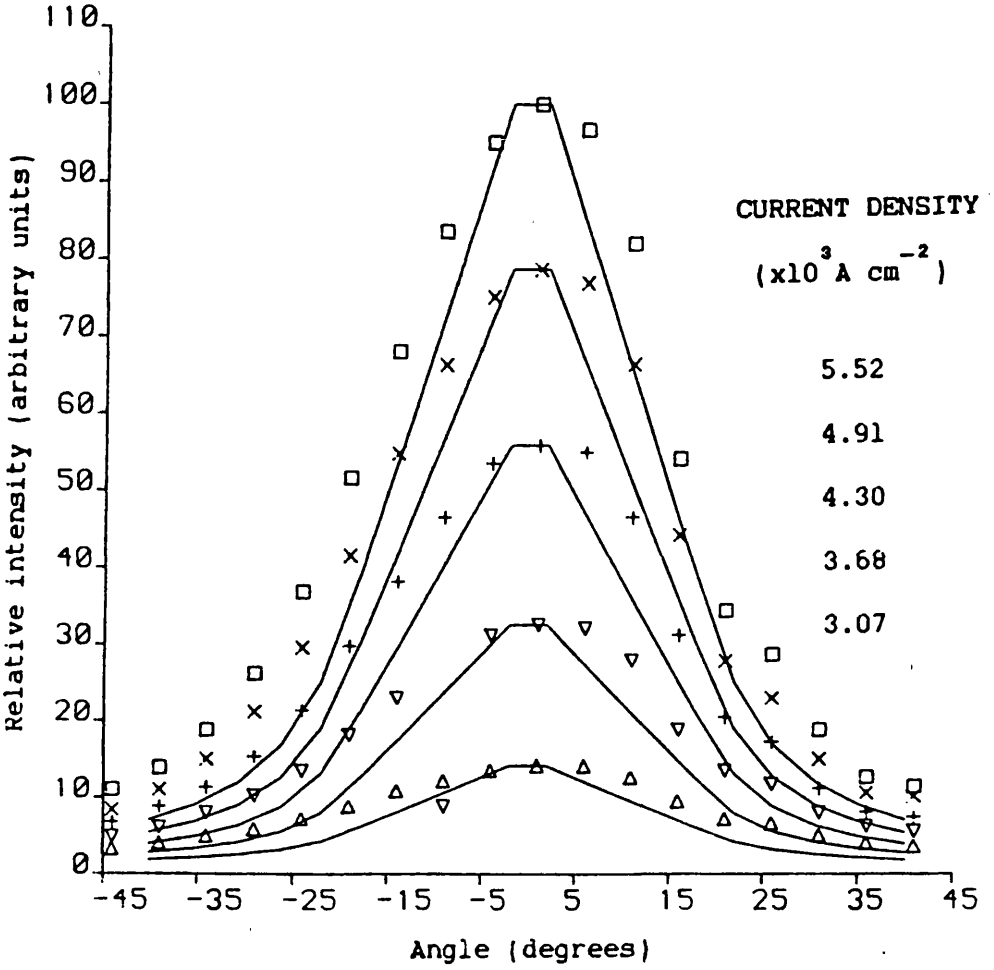

Fig(5.12) Comparison of theoretical and experimental far field angular distributions for SLD A291. Different curves correspond to different current densities.

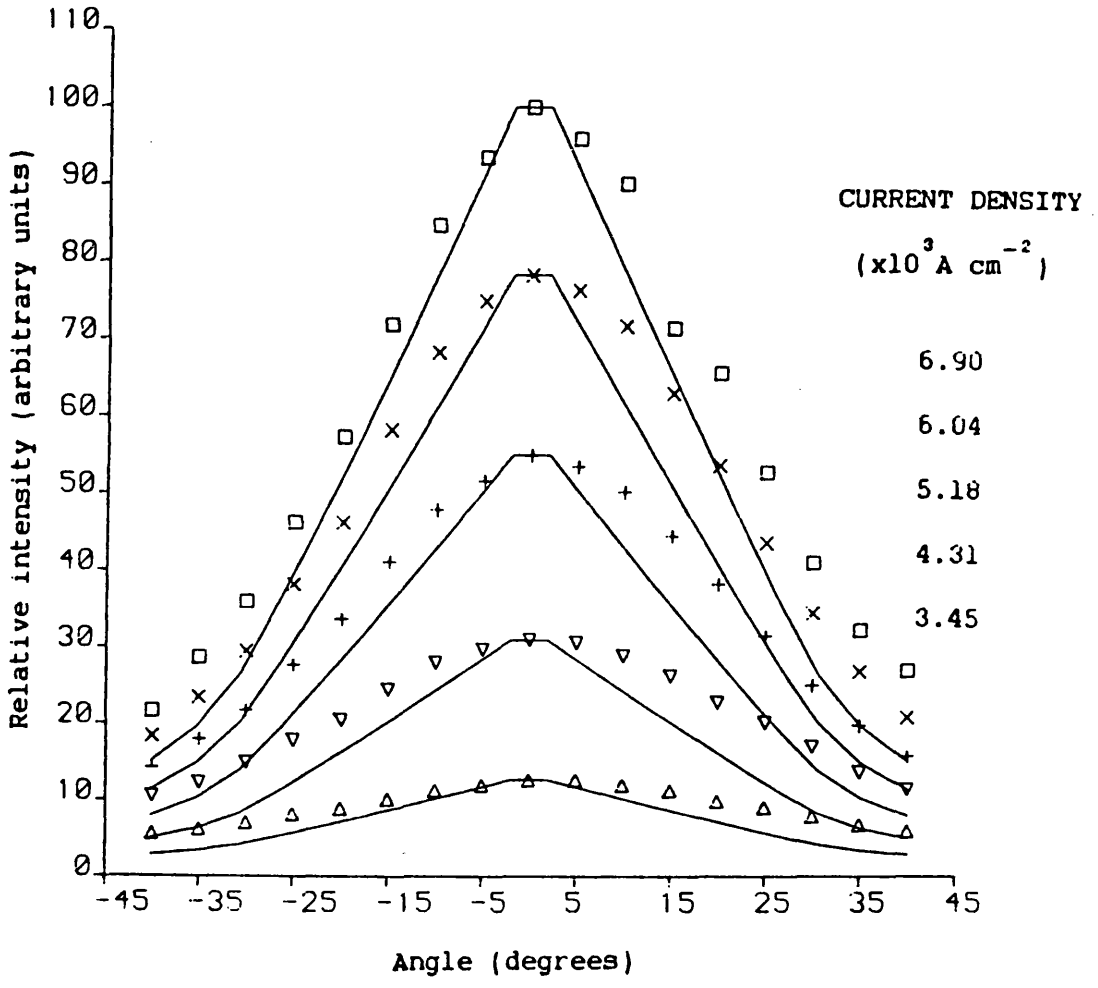

Fig(5.13) Comparison of theoretical and experimental far field angular distributions for SLD A207. Different curves correspond to different current densities.

current densities where the inversion population varies considerably along the length of the SLD. It has been shown by Kambayashi and Sarma, [8] that a 'rounded top' rather than a triangular peaked angular distribution is obtained if, in fact, the inversion population is taken to have a continuous distribution along the direction of the stripe width. In their calculations a gaussian form for the inversion population and a parabolic form for the local gain were used in the lateral direction. Longitudinal variation of the inversion population was not included in their work. Consequently to match their results with the experimental far-field intensity distributions presented here they had to use a rather complicated current dependency for the coefficients governing the parabolic gain variation across the width of the SLD.

5.4 Concluding Remarks

A comparison between theoretical results, obtained from the SLD model described in chapter(4), and experimental measurements made on a number of SLDs has been carried out. Good agreement between theoretical and experimental light/current characteristics was obtained for three out of six SLDs. This agreement extended over a large range of current densities. The fact that good agreement could not be obtained for all of the SLDs was not unexpected, since the characteristics of semiconductor devices, like SLDs, can vary considerably. There are many reasons for this, nearly all to do with the quality and consistency of double heterostructure material. Other factors such as bad contacting and degradation can also alter device characteristics. Agreement between experiment and theory was obtained for the light/current characteristics of two of the remaining three SLDs by altering the radiative recombination efficiency in the model.

Altering the radiative recombination efficiency effectively takes into account defects in the material that cause non-radiative recombination.

The use of realistic local gain and spontaneous emission curves in the theoretical model has been shown to be justified by the very good agreement obtained between the theoretical and experimenal spectral results for all of the SLDs from wafer(A). Such good agreement, over a very wide range of wavelengths and current densities, has not previously been reported. It must, however, be mentioned that the same good agreement between experimental and theoretical spectra was not forthcoming for the two SLDs from wafer(B). This is not surprising since semiconductor material parameters vary considerably from wafer to wafer, and even across the same wafer. Although the theory has only been compared with experimental data for six SLDs from two different wafers it does appear that the model can be successfully used to predict fairly accurate characteristics of SLDs providing the material parameters used in the model have been obtained by matching light/current and spectral characterics for a device from the same wafer.

The far-intensity distributions produced by the one-dimensional formulation of the photon conservation equations in the SLD model show adequate agreement with experimentally measured results. The theoretical results are narrower and have a triangular peak. These discrepancies occur because in the model rigid boundary conditions in the lateral direction, have been used; namely the assumption of constant inversion population and local gain distributions in that direction. It is however a much more complicated problem to include a lateral variation of the inversion population while maintaining its longitudinal dependency and the

simpicity of the one-dimensional formulation in the model is attractive. The increase in the accuracy of predicting the far-intensity distribution that would be achieved by using a two dimensional model does not warrant the extra computational time that would be needed.

References

1) 'Dependence of threshold and electron lifetime on accepter concentration in GaAs-$Ga_{1-x}Al_xAs$ lasers', C.J.Hwang, J.C.Dyment, J. Appl. Phys., vol.44, p.3240, 1973.

2) 'Electron lifetime and diffusion constant in germanium-doped Gallium Arsenide', G.A.Acket, W. Nijman and H.'tLam, J. Appl. Phys., vol.45, p.3033, 1974.

3) 'Current dependence of spontaneous carrier lifetime in GaAs-$Ga_{1-x}Al_xAs$ double-heterostructure lasers', H.Namizaki, H.Kan, M.Ishii and A.Ito, Appl. Phys. Letters, vol.24, p.486, 1974.

4) 'Edge emitting GaAs/GaAlAs LEDs', A.G.Steventon, J.V.Collins, and P.J.Fiddyment, Post office telecommunications headquaters research memorandum, No.79/R4/6, August 1979.

5) 'The influence of technological parameters on spectral properties of double heterostructure superluminescent diodes', Amann, Boeck, and Harth, Frequenz, vol.45, p.635, 1978.

6) 'Spectral behaviour and linewidth of GaAlAs GaAs double heterostructure lasers at room temperature with stripe geometry configuration', Iida, Takata, and Unno, IEEE J. of Quant. Electron., vol.QE-9, p.361, 1973.

7) 'Heterostructure lasers, Part B:Materials and operating characteristics', H.C.Casey,Jr. and M.B.Panish, Academic Press, 1978.

8) 'Spontaneous emission noise distribution from a gain-guided multimode waveguide', T.Kambayashi and J.Sarma, IEEE J. of Quantum Electron., vol.QE-9, p.1084, 1983.

CHAPTER 6

THEORETICAL CHARACTERISTICS OF SLDS

6.1 Introduction.

In the previous chapter a comparison of theoretical and experimental light/current characteristics, spectral and far-intensity 'angular' distributions was carried out for a number of SLDs. In making these comparisons little or no mention of the internal workings of the SLD were made. It is the purpose of this chapter to describe and to explain in detail the SLD's characteristics. This is done with the help of the SLD model, developed in chapter 4, which allows the growth and/or decay of the forward and reverse travelling photon fluxes to be traced throughout the length of the SLD. Wherever possible simple analytic solutions which exist for the photon conservation equations are used to clarify the discussion. In the description of the spectral distribution of the SLD the wavelength dependence of gain saturation receives special attention. The interest in this property stems from realising in optical amplifiers the possibility of altering one optical signal using another signal at a different wavelength. Opto-optic modulators and oscillators, [1], and an optical analogue of the transistor, [2], based on this principle have been postulated. Methods of improving the output power available from SLDs are also discussed together with the advantages and disadvantages they have on the other characteristics. All the results presented in this chapter are theoretical; however, their credibility is enhanced by the use of the same parameters that were used successfuly to match the experimental characteristics of a number of SLDs in chapter 5.

The light/current characteristics of the SLD are discussed first in section (6.2). This is followed by a description of the SLD's spectral distribution in section (6.3). This section includes a detailed description of the wavelength dependence of gain saturation. The far-intensity angular distribution is described in section (6.4) before moving on to discuss ways and means of increasing the light output power of SLDs in section (6.5). Some concluding remarks are made in section (6.6).

6.2 Light/current characteristics.

The light/current characteristics of a typical SLD consist of three well defined regions, fig(6.1):

a) a linear region at low current densities,

b) an exponential region at moderate current densities,

c) a further linear region at high current densities.

Regions (a) and (b) can be adequately described using simplified versions of the photon and charge conservation equations corresponding to equations(4.16), (4.17) and (4.28) respectively,i.e.

$$\frac{\delta P_f}{\delta z} = G(N).P_f + \delta.R_{spon}(N) \qquad (6.1)$$

$$\frac{\delta P_b}{\delta z} = - G(N).P_b - \delta.R_{spon}(N) \qquad (6.2)$$

$$\frac{J}{qd} = G(N).(P_f + P_b) + R_{spon}(N) \qquad (6.3)$$

In these equations the angular, wavelength and polarisation dependencies of equations(4.16), (4.17) and (4.28) are not included for brevity. An analytic solution exists for equations (6.1) and

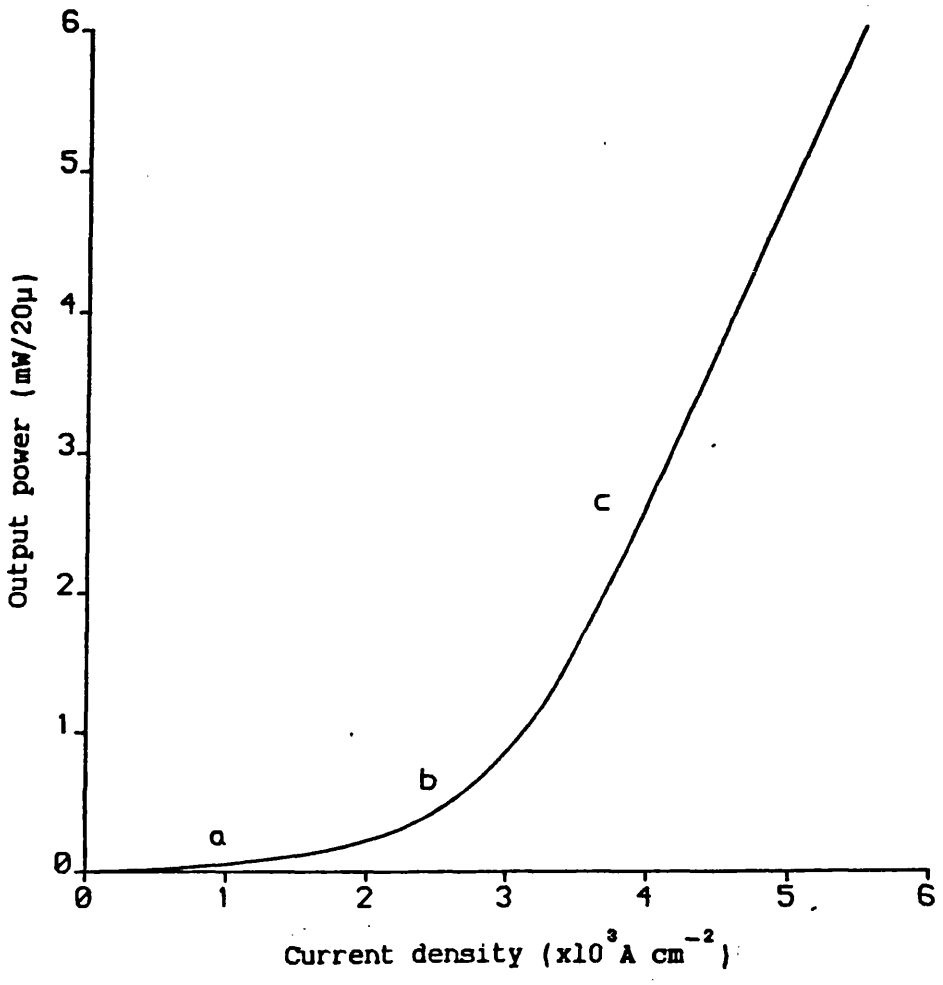

Fig(6.1) Theoretical light current characteristic of SLD A291.

(6.2) if the photon densities, P_f and P_b are small enough so as not to alter the inversion population significantly, e.g.

$$P_f(L) \cong \frac{\delta.R_{spon}(N).(\exp(G(N).L) - 1)}{G(N)} \qquad (6.4)$$

This is a good approximation for the current densities in regions (a) and (b) of the light/current characteristic, fig(6.1), where the inversion population is approximately constant along the length of the SLD, seen quite clearly in fig(6.2). The different curves in fig(6.2) correspond to different. At low current densities where the modal gain, G, is very small the exponential term in equation(6.4) can be expanded to give

$$P_f(L) \cong \frac{\delta.R_{spon}(N).(1 + G(N).L) - 1)}{G(N)} \qquad (6.5)$$

In equation(6.5) G(N) cancels and the photon density depends only on the spontaneous emission. It is also evident from equation (6.3), that the spontaneous emission rate is approximately proportional to the current density when the gain term is small. Hence the output power increases linearly with current density, region (a) in fig(6.1). At moderate current densities the gain term in eguation (6.4) is positive and dominates the spontaneous emission term so that the output power shows an exponential growth with current density, region (b) in fig(6.1). The second linear region of the light/current characteristic, region (c) in fig(6.1), cannot be described by these simplified equations because the inversion population is not constant along the length of the device, fig(6.2). This linear region of the light/current characteristic is attributed to gain saturation. The photon density becomes so large that it depletes the carrier density

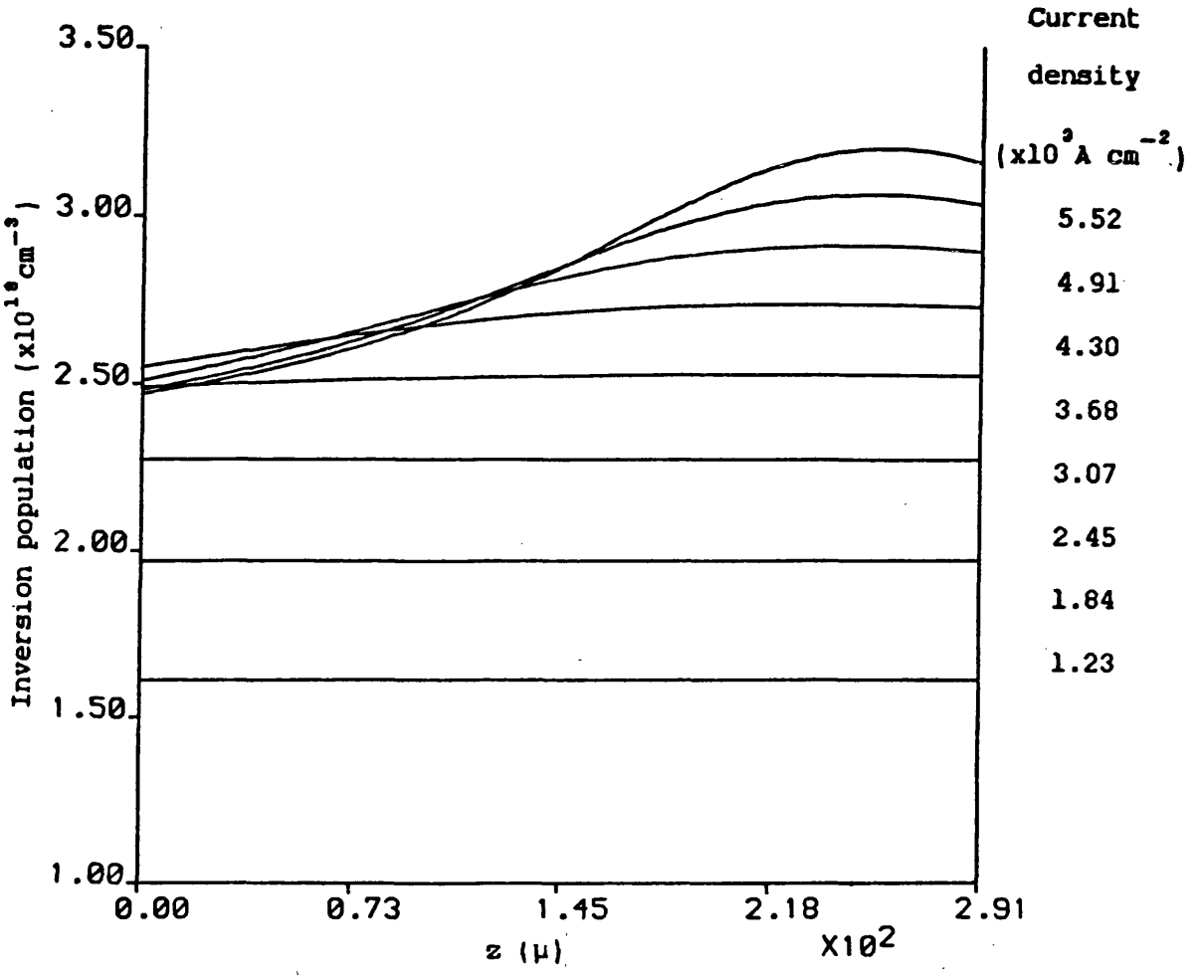

Fig(6.2) Variation of the inversion population in SLD A291 with z.

which, in turn, reduces the growth of P_f and P_b.

The photon distribution within the SLD varies considerably with current density. The photon distributions with length corresponding to a typical current density within regions (a), (b) and (c) of the light/current characteristic, fig(6.1), are shown in figs(6.3-6.5) respectively. The growth of the forward travelling photon flux at current densities corresponding to regions (a) and (b) in fig(6.1) are explicitly given by equation(6.4). At a very low current density, fig(6.3), it can be seen that both P_f and P_b grow quickly with length at first and then saturate. The reason for this behaviour can be understood by substituting a negative value for the gain, G(N), in equation(6.4). The photon distribution within the SLD at a current density within region (b) of fig(6.1) is quite different, both P_f and P_b grow exponentially. Note that the value of P_b is much larger at z=0 than P_f is at z=L. This is a natural consequence of the boundary conditions of the SLD. The front facet reflectivity, R_f=0.3 at z=L, provides an initial value for P_b at z=L whereas the boundary condition, R_b=0.0 at z=0, does not, i.e. P_f=0.0 at z=0. The photon distribution within the SLD at a high current density, corresponding to region (c) in fig(6.1), becomes very assymetric, fig(5.5). P_b attains a very large value as it approaches z=0, so large in fact that it significantly depletes the carriers in the rear of the SLD, fig(6.2). The gain is of course also reduced in this region because it is a function of the inversion population. This not only affects the spatial growth rate of P_b but also the growth rate of P_f so that the increase in output power at high current densities is reduced from the exponential increase seen in region (b) of fig(6.1) to the linear increase of region (c).

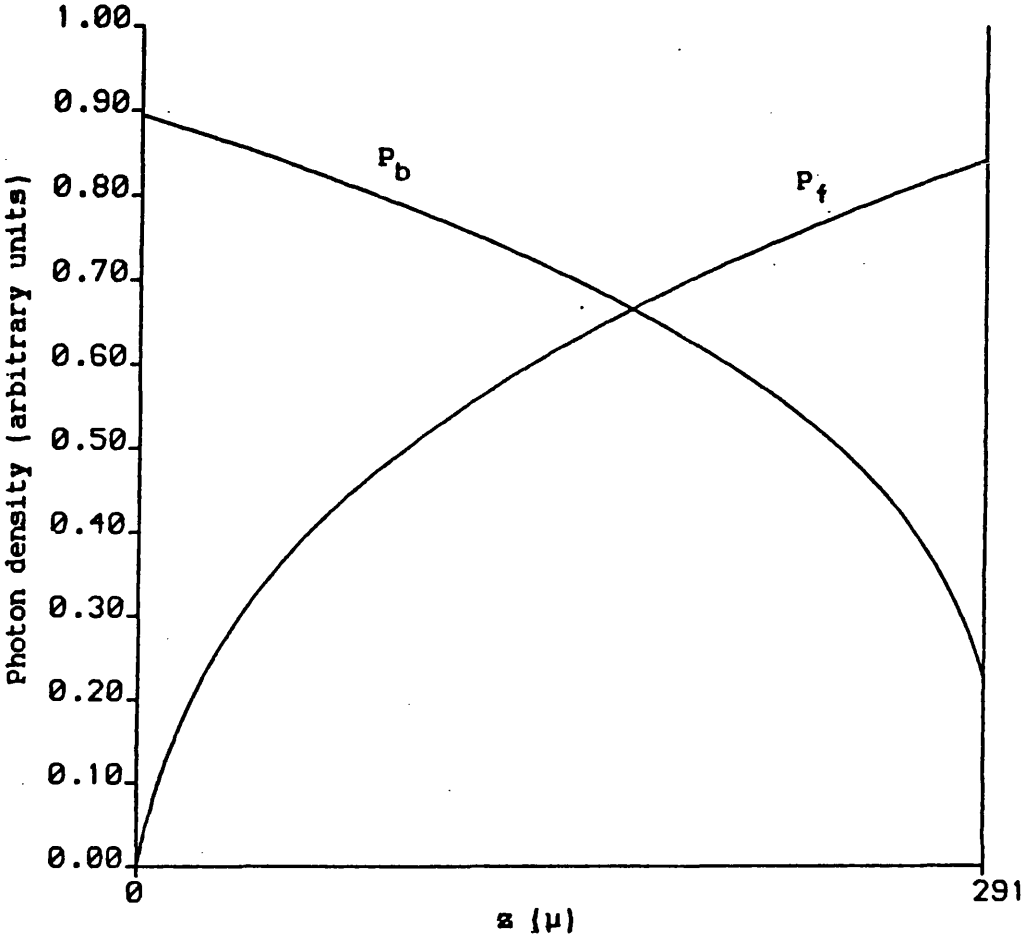

Fig(6.3) Variation of the photon densities P_f and P_b with z in SLD A291,($J = 0.61 \times 10^3 A\ cm^{-2}$).

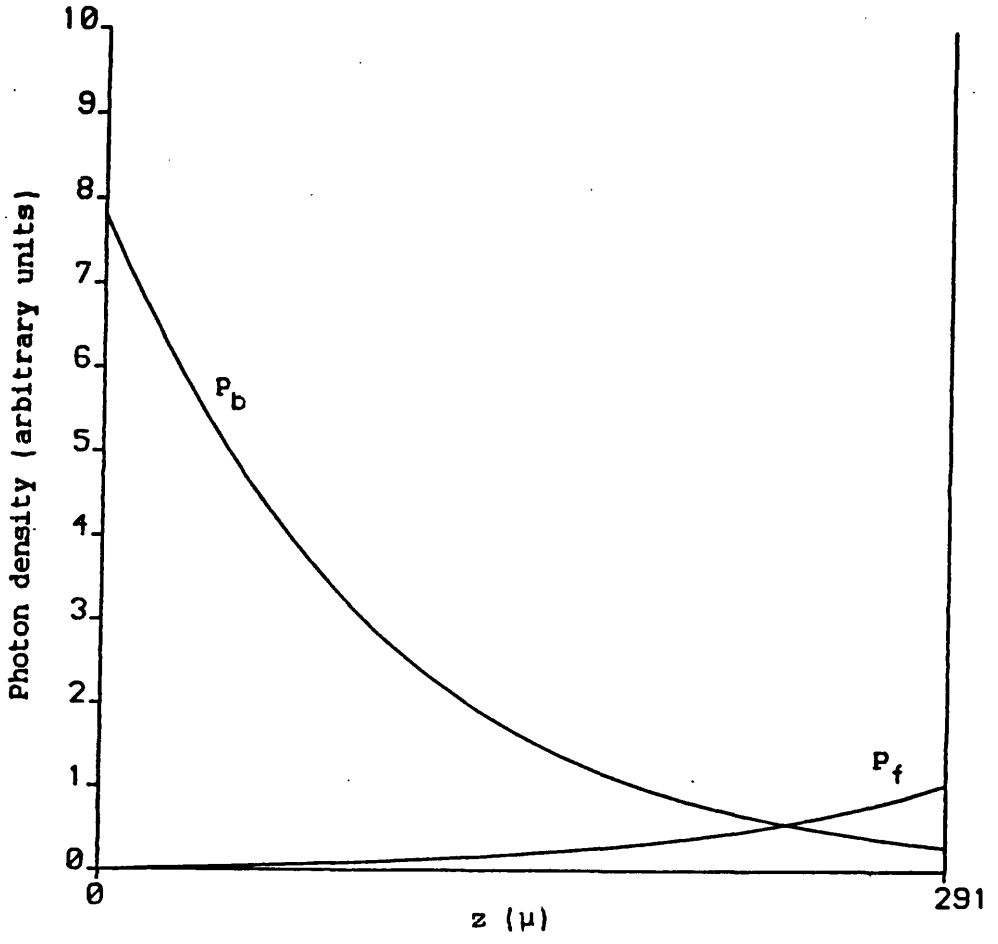

Fig(6.4) Variation of the photon densities P_f and P_b with z in SLD A291,($J = 3.68 \times 10^3 A\ cm^{-2}$).

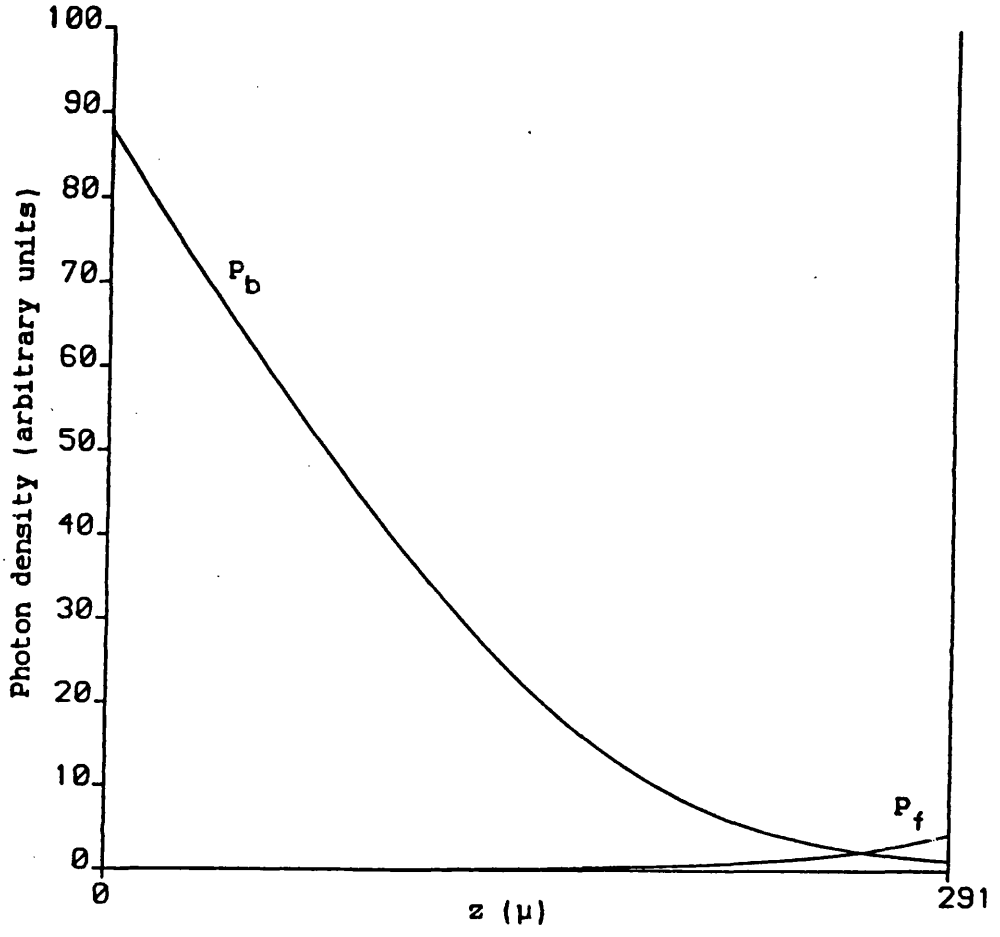

Fig(6.5) Variation of the photon densities P_f and P_b with z in SLD A291,($J = 5.52 \times 10^3 A\ cm^{-2}$).

6.3 Spectral Distribution.

The spectral distribution of an SLD varies considerably with both current density and stripe length. Consider first how the SLD's spectrum changes with current density, fig(6.6). At low current densities the spectrum is very broad, however it quickly narrows as the current density is increased before reaching an almost constant width. Coupled with the spectral narrowing with current density is a movement in the spectral peak from low energy (long wavelength) to high energy (short wavelength). The initial fast movement and narrowing of the SLD's spectrum that occurs at low current densities is attributed to bandfilling. At such low current densities the inversion population increases quickly with current density because the transitions are predominately spontaneous rather than stimulated, fig(6.2). The saturation of the spectral width and the movement of the peak wavelenth at high current densities occurs because of gain saturation. Stimulated emission is dominant at high current densities eating up carriers in the process. This reduces the rate of increase of the inversion population with current density and in fact the inversion population dips considerably towards the rear of the stripe contact, fig(6.2).

An alternative, and perhaps more effective way of displaying the spectral narrowing that occurs in SLDs is to plot the spectral width at half maximum power against current density, fig(6.7). The different curves correspond to various stripe contact lengths. The most striking thing about this graph is the way in which the minimum spectral width narrows as the SLD's stripe contact length is increased. A further feature of fig(6.7) occurs at very high current densities where the spectrum can be seen to broaden slightly. This phenomena has not been observed exprimentally in any

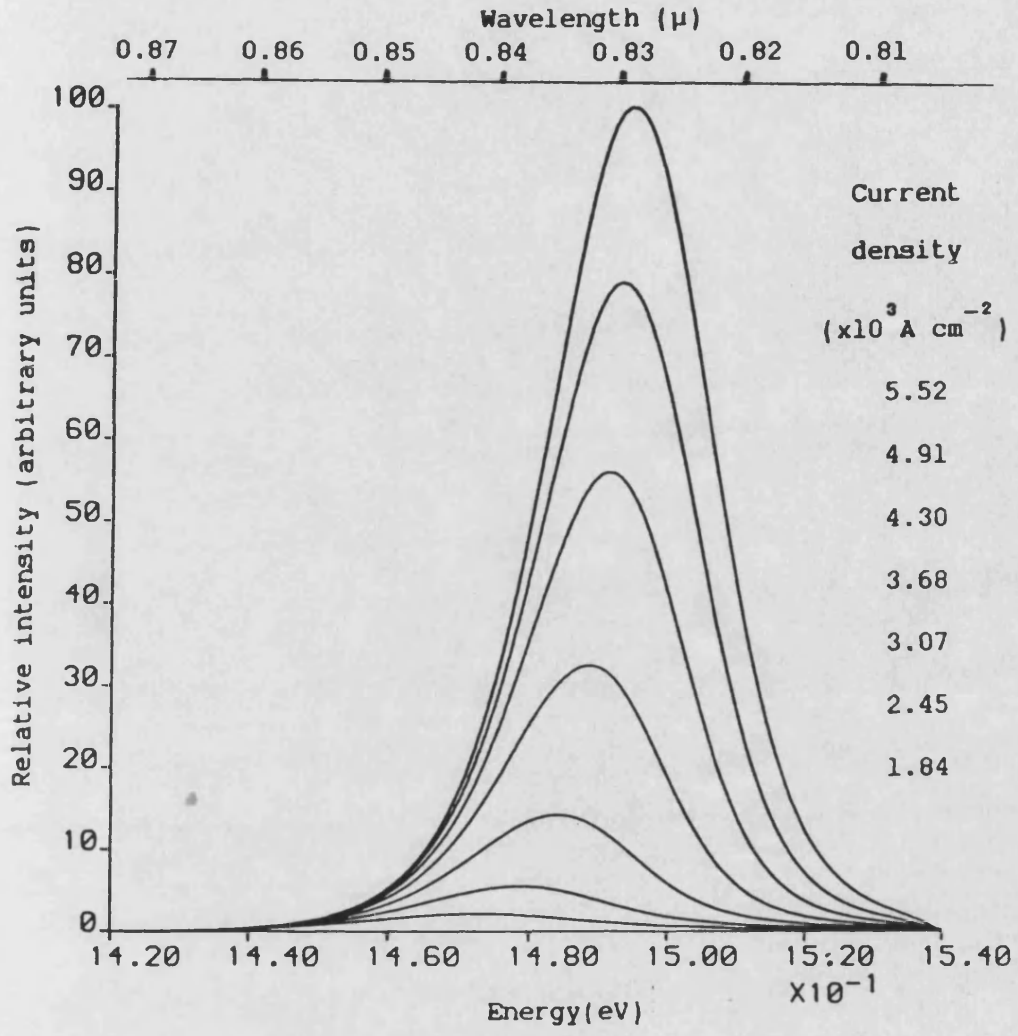

Fig(6.6) Theoretical spectral characteristics of SLD A291.

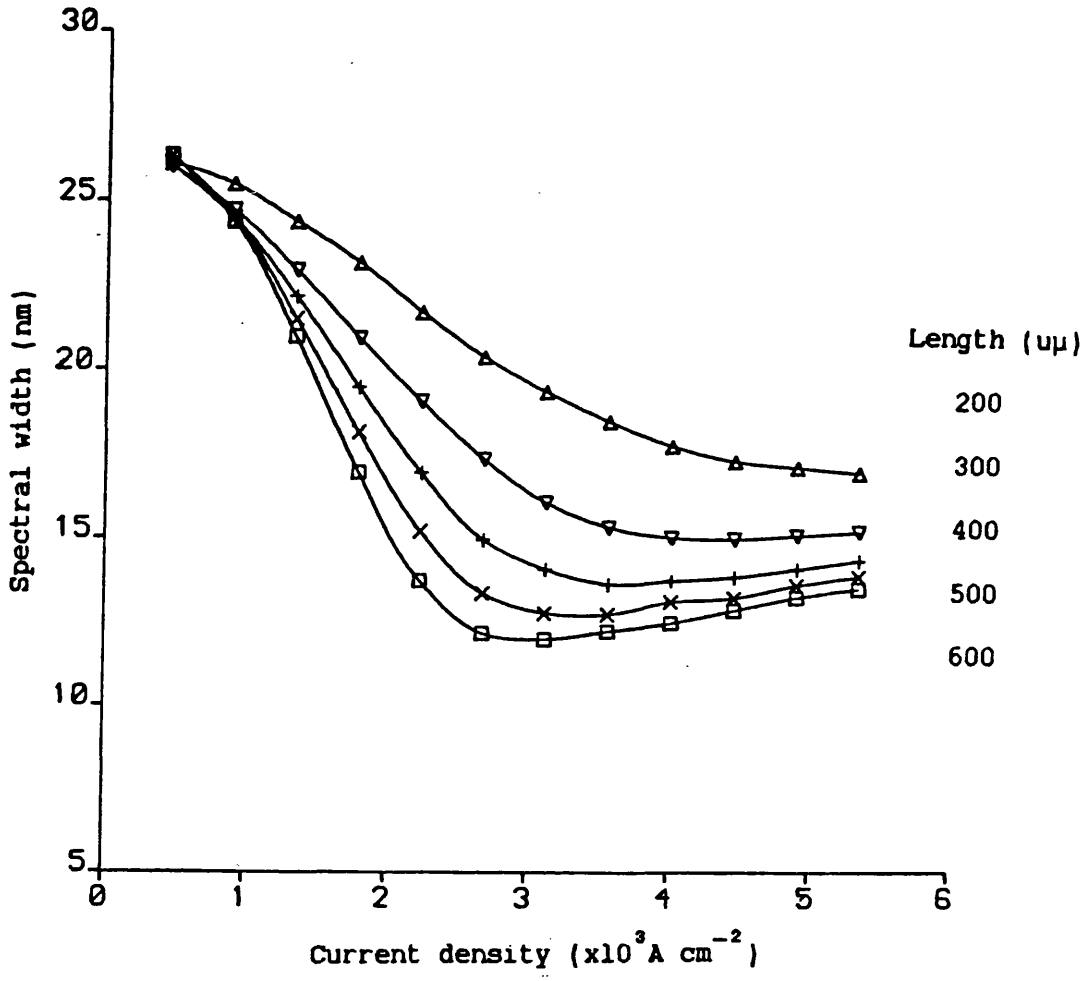

Fig(6.7) Variation of the SLD's spectral width, at half maximum power, with current density for various stripe contact lengths.

of our SLDs, however the experimental results of Boeck and Amann, [3], do show this trend. Our failure to observe this experimentally is believed to be because our SLDs have relatively short absorbing regions ($\cong$ 200μ), table(5.2) which prevents the use of the high current densities necessary to observe this effect. The reason for this spectral broadening can be understood by studying the inversion population curves in fig(6.2). At very high current densities the inversion population under the rear half of the SLD's stripe contact is essentially 'locked' at one level while still increasing with current density under the front half of the stripe. This means that the gain curves are becoming broader in the front of the device and also still moving to slightly lower wavelengths while remaining approximately constant in the rear of the SLD; consequently the spectrum broadens.

The movement of the spectral peak can also be plotted as a function of current density for various device lengths, fig(6.8). It can be seen that the movement of the spectral peak also tends to saturate but not nearly so much as the spectral width curves. These results, which have been shown to agree with experimental measurements in chapter(5), differ from the experimental results of Boeck and Amann, [3]. Their results show a much more pronounced saturation, with the peaks of at least some of their SLDs moving towards longer wavelengths at high current densities. The movement of the spectral peak to long wavelengths with current density has been shown theoretically by Goebel et al, [4]. Their model, however, assumed a constant inversion population along the length of the pumped region which is unrealistic at high current densities. No experimental evidence was shown to substantiate the theoretical movement of the spectral peak to long wavelength with current

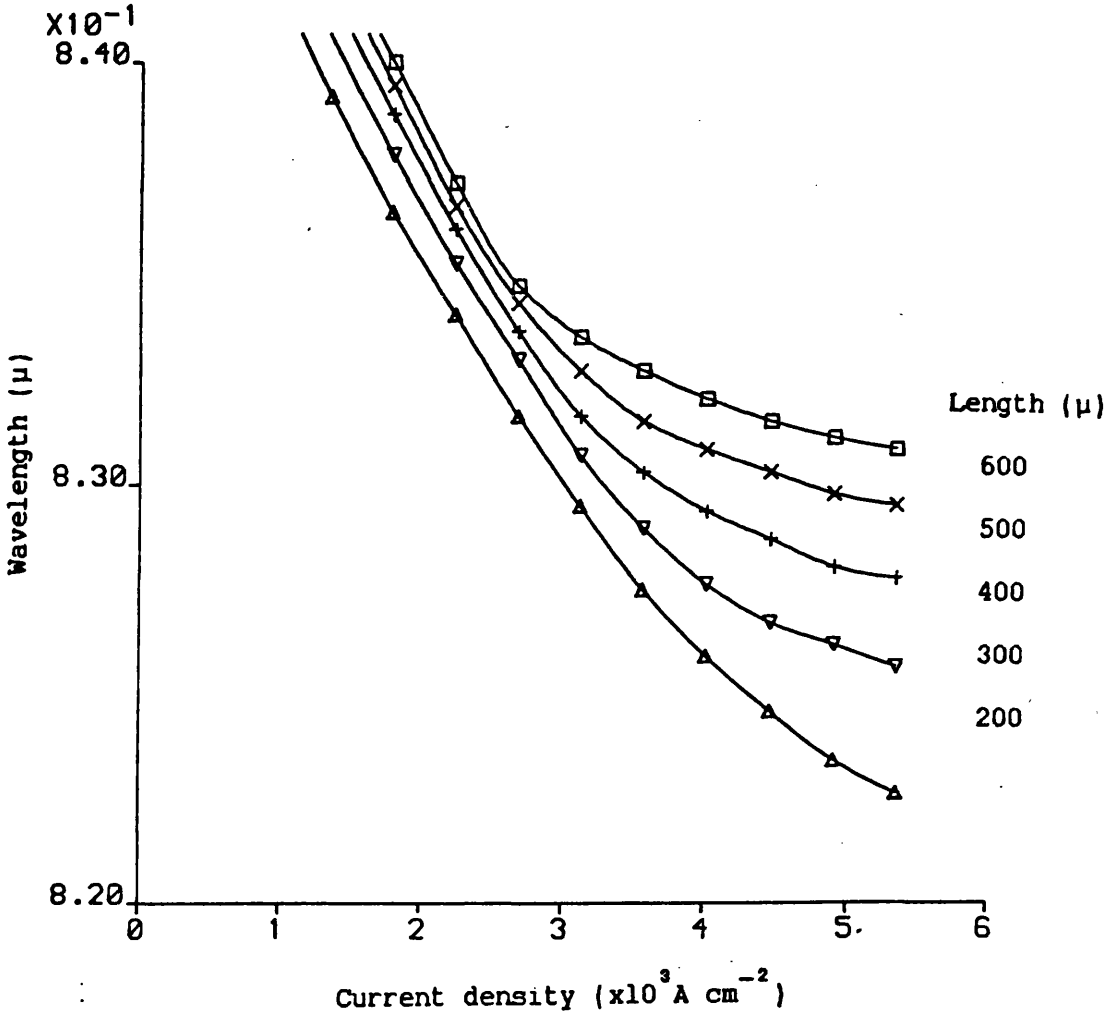

Fig(6.8) Movement of the SLD's spectral peak with current density for various stripe contact lengths.

density. They did, however, show both theoretically and experimentally that the spectral peak moves to long wavelengths with increasing length at a constant current density. The movement of the spectral peak to long wavelengths was attributed to the wavelength dependence of gain saturation, see section(6.31). The reason why the saturation of the peak movement in our model is not so pronounced as that shown by Boeck and Amann probably stems from material differences. Remember that the gain curves used in this model have been specifically tailored to suit the SLDs measured in this project. If the local gain increases more quickly with inversion population, as would be the case if the bimolecular recombination rate was larger, saturation of the spectral peak movement would occur earlier and be more prominent.

6.31 Wavelength dependent saturation in SLDs.

The spectral behaviour of the SLD with length is shown in figs(6.9) and (6.10). These two graphs correspond to two different current densities one low, fig(6.9) and the other high, fig(6.10). Note that the spectral peak moves in the opposite direction with increasing length to that which it does with increasing current density, i.e from high energy (short wavelength) to low energy (long wavelength). A comparison of figs(6.9) and (6.10) shows that the spectrum is narrower and shifts by increasing amounts with length at a high current density than it does for a low current density. However, the most striking feature is observed from fig (6.10) where the spectral curves for the longer device lengths actually cross those of shorter device lengths at the high energy (low wavelength) side of the spectrum. This is a clear indication of the wavelength dependence of gain saturation. The implication is that the growth of

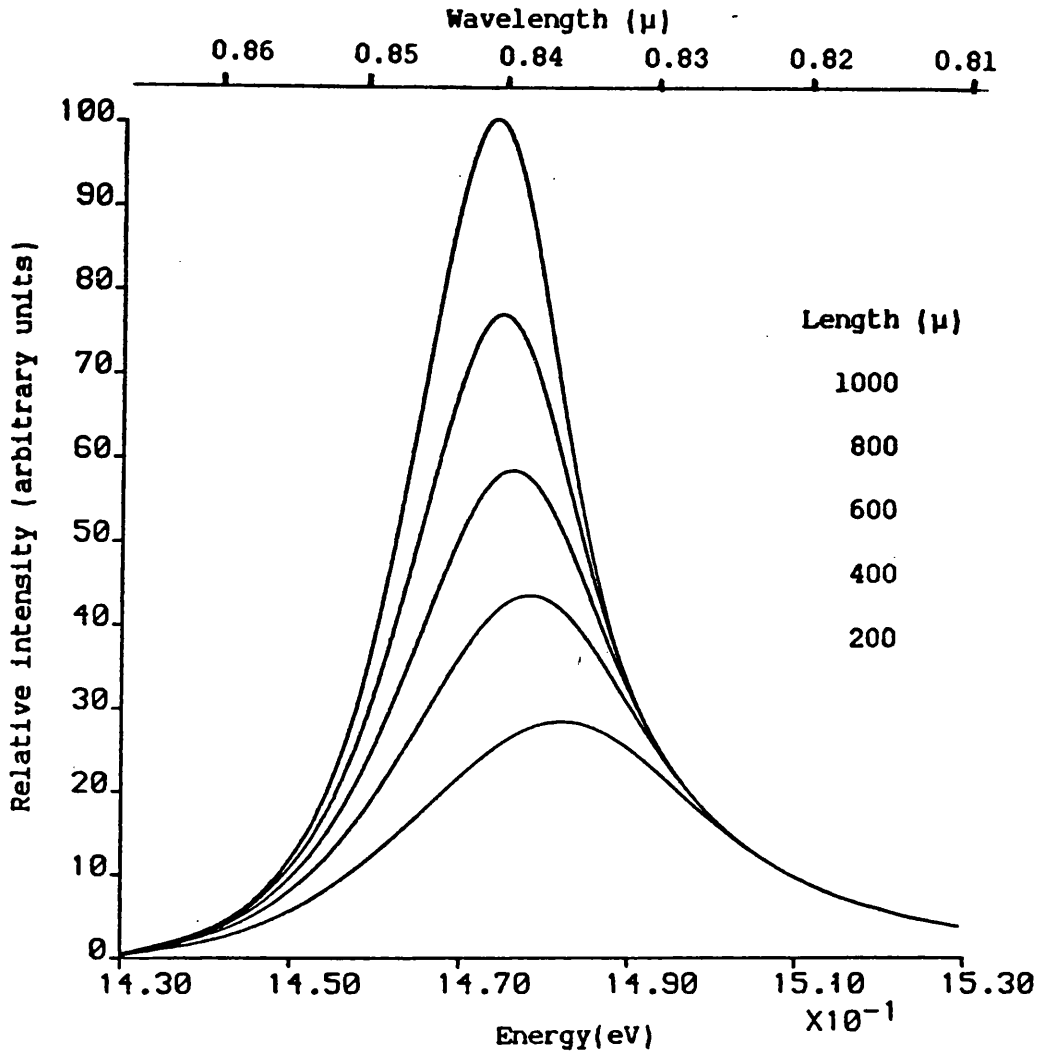

Fig(6.9) Spectral variation of the SLD shown as a function of length. Current density = 1.79×10^{3} A cm^{-2}.

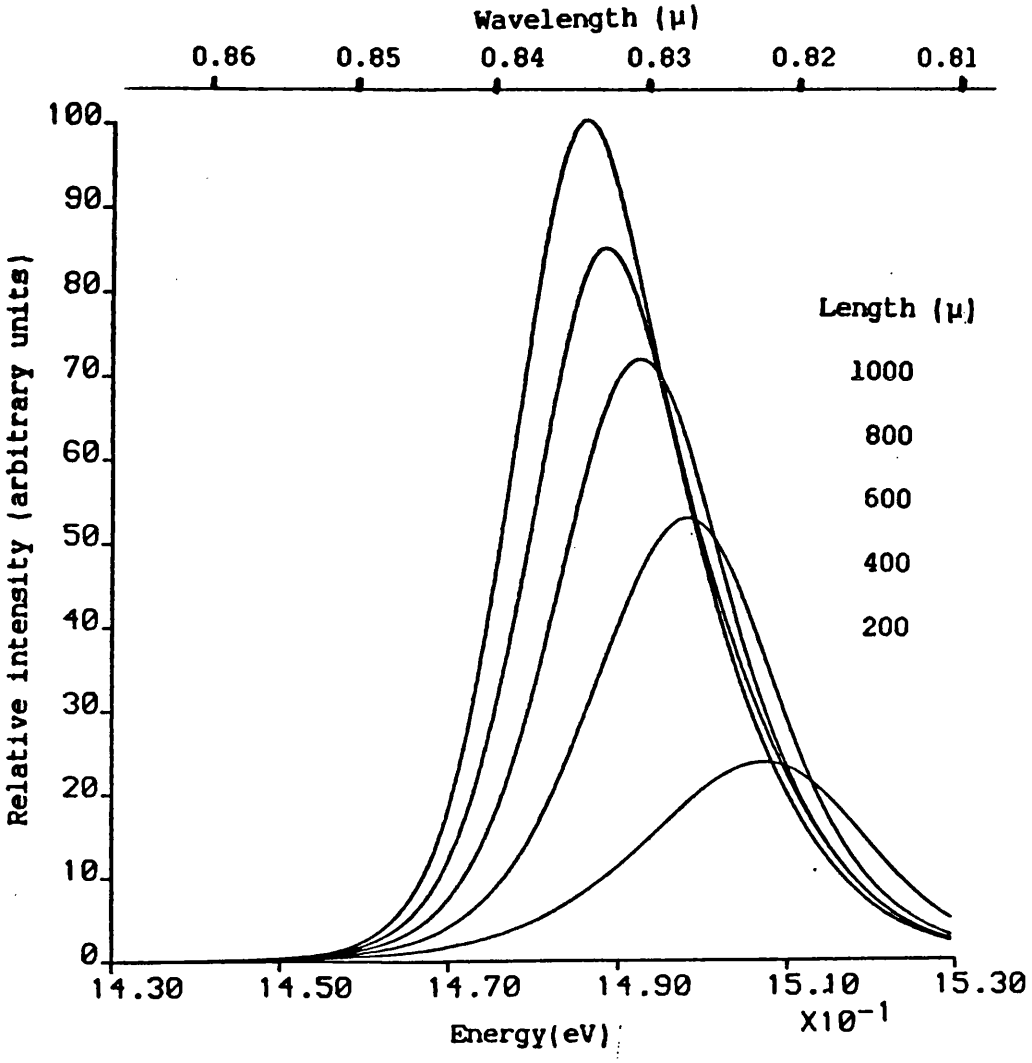

Fig(6.10) Spectral variation of the SLD shown as a function of length. Current density = 5.36×10^{3} A cm^{-2}.

the photon density at one wavelength causes the photon density at a different wavelength to saturate, [4,5]. This property has been described analytically, for a device similar in structure to the SLD, by Sarma, [5], who studied the single pass semiconductor amplifier. Consider two monochromatic signals that are large enough so that they alone affect the inversion population inside of the device. It is then possible to write the photon and charge conservation equations in the form

$$\frac{\delta P_f(\lambda_1)}{\delta z} = G(N,\lambda_1).P_f(\lambda_1) + \delta.R_{spon}(N,\lambda_1) \qquad (6.6)$$

$$\frac{\delta P_f(\lambda_2)}{\delta z} = G(N,\lambda_2).P_f(\lambda_2) + \delta.R_{spon}(N,\lambda_2) \qquad (6.7)$$

$$\frac{J}{qd} = G(N,\lambda_1).P_f(\lambda_1) + G(N,\lambda_2).P_f(\lambda_2) + \sum_{\lambda} R_{spon}(N,\lambda) \qquad (6.8)$$

Equations (6.6) and (6.8) can be combined to give

$$\frac{\delta P_f(\lambda_1)}{\delta z} = \frac{J}{qd} - G(N,\lambda_2).P_f(\lambda_2) + \sum_{\lambda} R_{spon}(N,\lambda) + \delta.R_{spon}(N,\lambda_1) \qquad (6.9)$$

It can be seen from equation (6.9) that the growth or decay of $P_f(\lambda_1)$ is dependent on $P_f(\lambda_2)$. Saturation occurs when $\frac{\delta P_f(\lambda_1)}{\delta z} = 0$ and

$$P_f(\lambda_2) = \frac{\frac{J}{qd} - \sum_{\lambda} R_{spon}(N,\lambda) + \delta.R_{spon}(N,\lambda_1)}{G(\lambda_2)} \qquad (6.10)$$

$P_f(\lambda_2)$ must of course be positive to have any physical meaning and from equation(6.8) the numerator of equation(6.10) is also positive, therefore $G(\lambda_2)$ must also be positive for saturation to occur. In

addition to this it can be seen from equation (6.7) that $G(N,\lambda_1).P_f(\lambda_1) < \delta.R_{spon}(N,\lambda_1)$ i.e. $G(\lambda_1)$ must be negative. This means that saturation only occurs at the high energy side of the spectrum where the gain curves become negative (see fig(5.6) in chapter(5)). A fact that is confirmed by the results shown in fig(6.10).

An alternative way of displaying the wavelength dependent saturation that occurs with length is to plot the variation of the photon density with length for different wavelengths, figs(6.11) and (6.12). The behaviour of the photon densities distribution with length at the two extremes of the spectrum show a stark contrast; saturation only occuring at short wavelengths (high energies), fig(6.12). The saturation that occurs is also quite clearly in the rear half of the device, fig(6.12), and shows up more dramatically in the reverse travelling photon flux. This behaviour is, of course, expected because it is in the rear part of the device that the inversion population is depleted most, fig(6.2). The carriers are depleted in the rear part of the device because the reverse travelling photon flux at central wavelengths, where the photon density is largest, is much larger than the forward travelling flux, fig(6.11). The curves in fig(6.12) for the shortest wavelenth show the forward travelling photon flux first saturating near z=0 because the gain is negative and then growing before eventually showing signs of saturation again at z=L.

Although it is possible to show analytically that wavelength dependent saturation occurs with increasing length it is more complicated to show analytically whether or not saturation will occur with increasing current density. It is conceivable that this effect might show up in the rear portion of the SLD because the

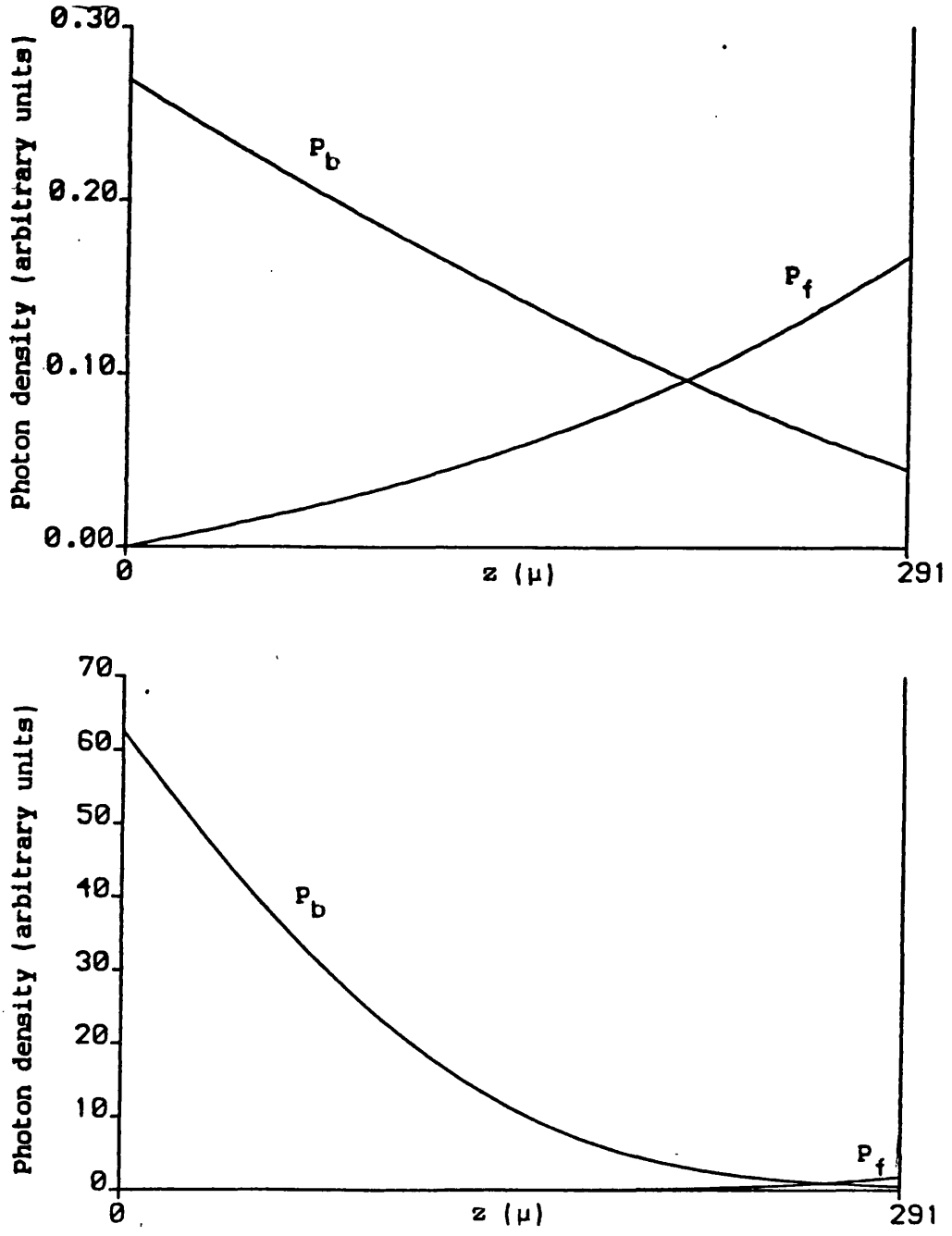

Fig(6.11) Variation of the photon density within an SLD at two different wavelengths, λ = 0.8521μ or E = 1.455 (top) and g = 0.8282μ or E = 1.497 (bottom). Current density = 5.52×10^3A cm^{-2}.

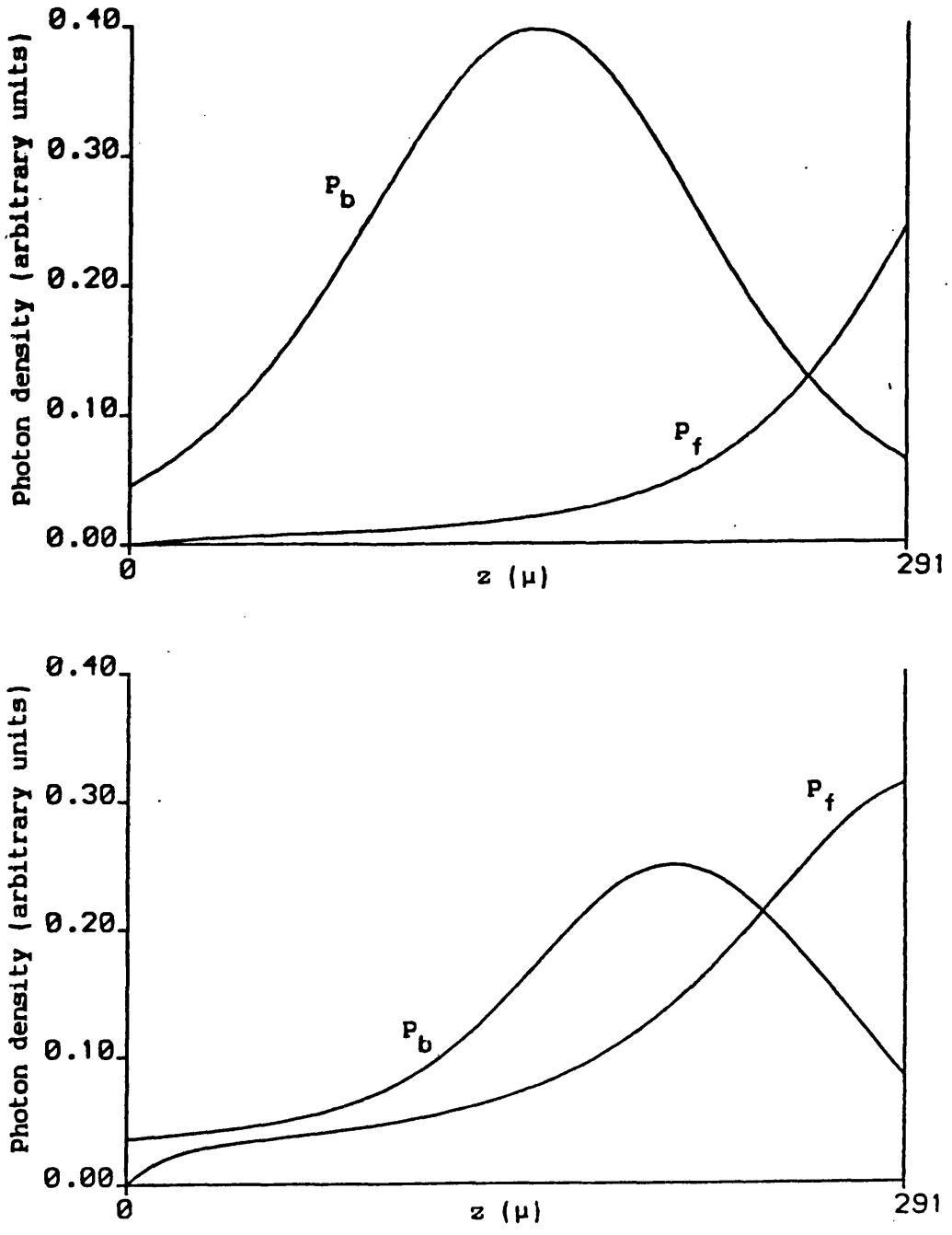

Fig(6.12) Variation of the photon density within an SLD at two different wavelengths, λ = 0.8130μ or E = 1.525 (top) and g = 0.8056μ or E = 1.539 (bottom). Current density = 5.52×10^{3} A cm^{-2}.

inversion population curves for very high current densities do actually cross in that part of the device, fig(6.2). This does in fact prove to be the case as fig(6.13) confirms. This graph shows the photon distribution with length at a very short wavelenth for two different current densities. It can be seen that the reverse travelling flux for the lower of the two current densities (dashed curve) does have a larger value at z=0 than its higher current density counter part, (solid curve). The difference between their two values is however very small and does not manifest itself significantly at the front of the SLD.

6.4 Far-intensity distribution.

The theoretical far-intensity distribution in the lateral direction has an unphysical triangular shape, fig(6.14). It is therefore worth reiterating some of the comments made in section(5.5) of the previous chapter: 1) The triangular nature of the peak stems from the use of a lateral gain distribution having an abrupt change from $G = G(N)$ underneath the stripe contact to $G = -\infty$ outside this region. 2) The missing rounded top tends to make the theoretical far-intensity distribution narrower than the corresponding experimental measurements. The fact that the theoretical results are narrower than the experimental measurements means that the theoretical results set an upper-limit for the performance of actual devices that may never be achieved in practice. It is however felt that the difference is sufficiently small to make the theoretical results useful.

It can be seen from fig(6.14) that the far-intensity angular distribution behaves similarly to the spectral distribution, starting off very broad at low current densities and narrowing quickly as the current density is increased, before saturating at

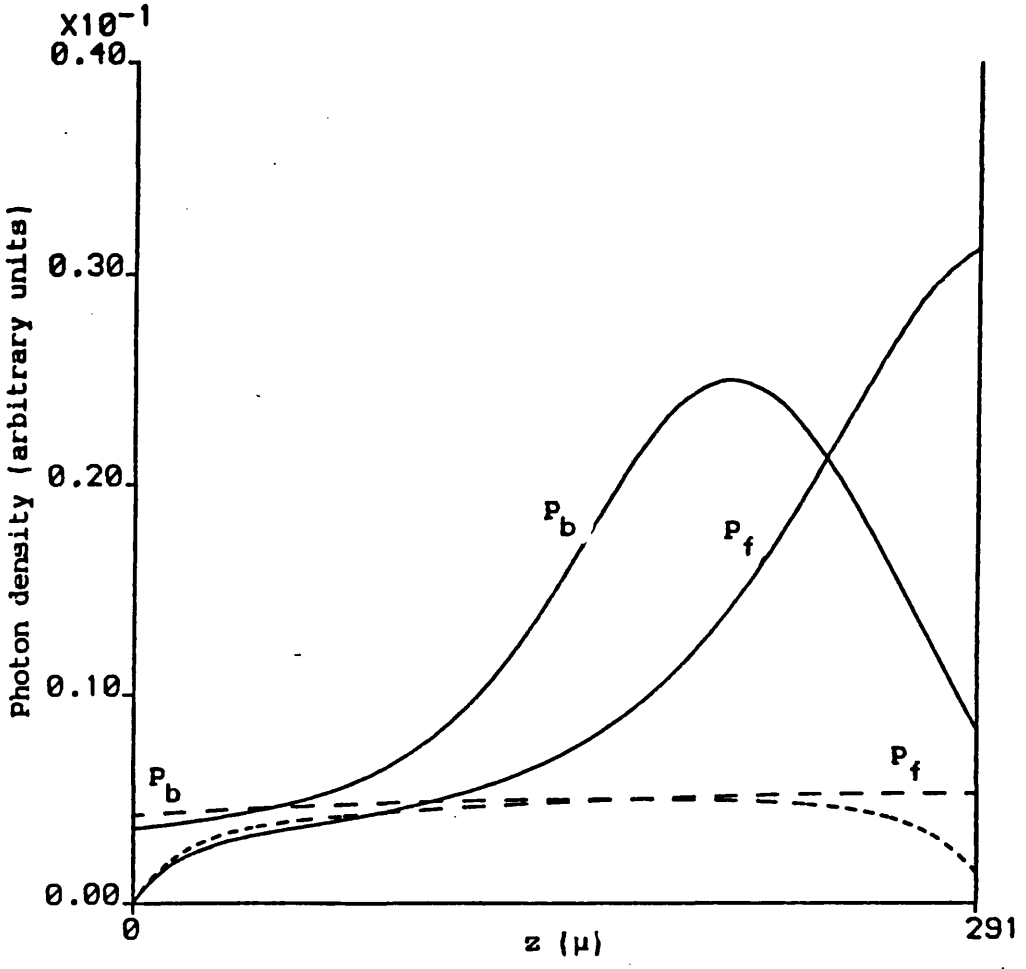

Fig(6.13) Variation of the photon density within an SLD at two different current densities, $J = 5.52 \times 10^{3}$ A cm^{-2} (solid curves) and $J = 4.91 \times 10^{3}$ A cm^{-2} (dashed curves). $\lambda = 0.8056\mu$ or $E = 1.539$.

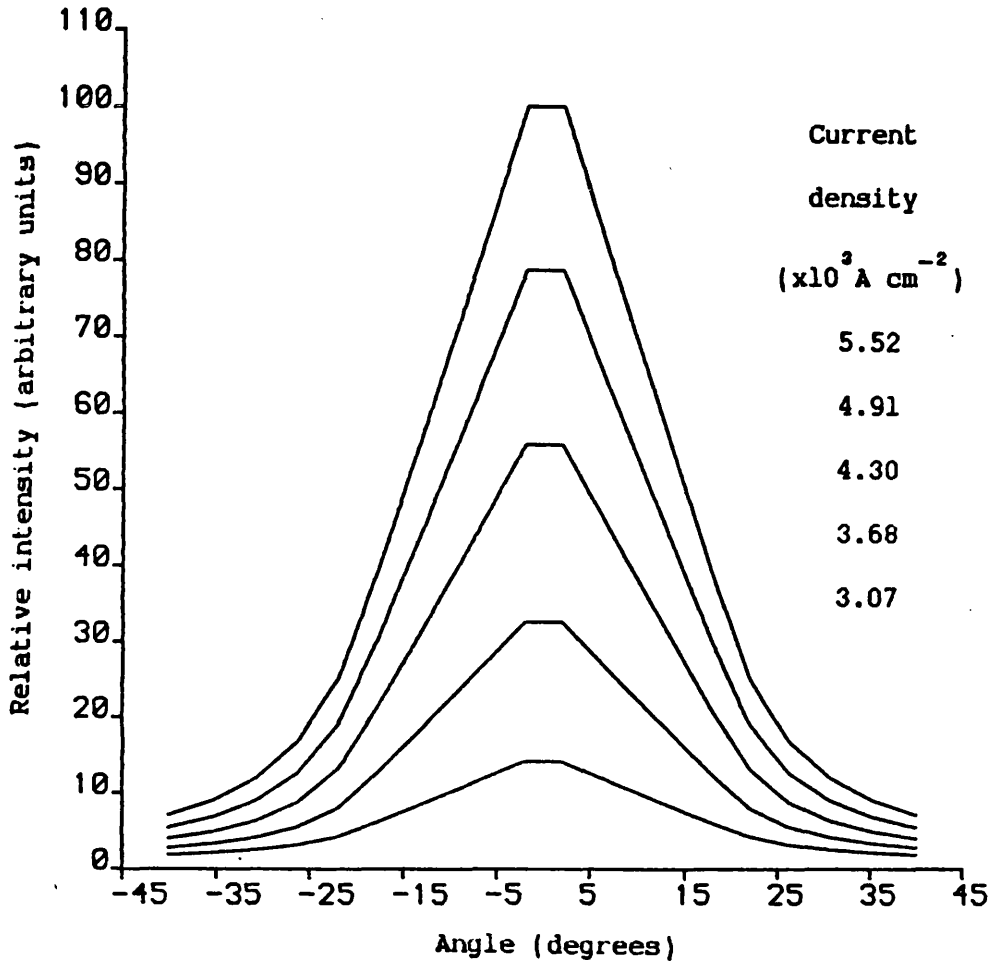

Fig(6.14) Theoretical far-field 'angular' distribution for SLD A291.

high current densities. This behaviour is much more visible if the width of the distribution measured at half maximum power is plotted against current density, fig(6.15). The different curves correspond to various stripe contact lengths. It is quite clear from this graph that the stripe contact length has a marked effect on the minimum far-intensity width that a particular device can attain. These results have implications not only on the coupling efficiency to optical fibres but also on the noise properties of optical amplifiers, [6].

6.5 Improving SLD characteristics.

The most obvious way of increasing the light output from an SLD is to increase the length of the stripe contact, fig(6.16). This is not only advantageous in increasing the light output for a given current density but also because the spectral width and the far-intensity angular distributions also narrow. There is, however, the drawback of having to increase the drive current significantly to maintain the same current density. Other methods of inceasing the output power are available. Increasing the width of the SLD will increase the output power but has a detrimental affect on the angular distribution and requires higher drive currents. Reducing the active layer thickness also increases the output power even though the actual optical confinement to the active layer is reduced, fig(6.17). No extra drive current is needed but the width of both the spectral and far-intensity angular distributions are increased, a rather undesirable effect. This occurs because the inversion population inside the SLD increases making the local gain larger and spectrally broader. The modal gain is, of course, also affected by the reduction in the confinement factor. The net effect is a modal gain curve that

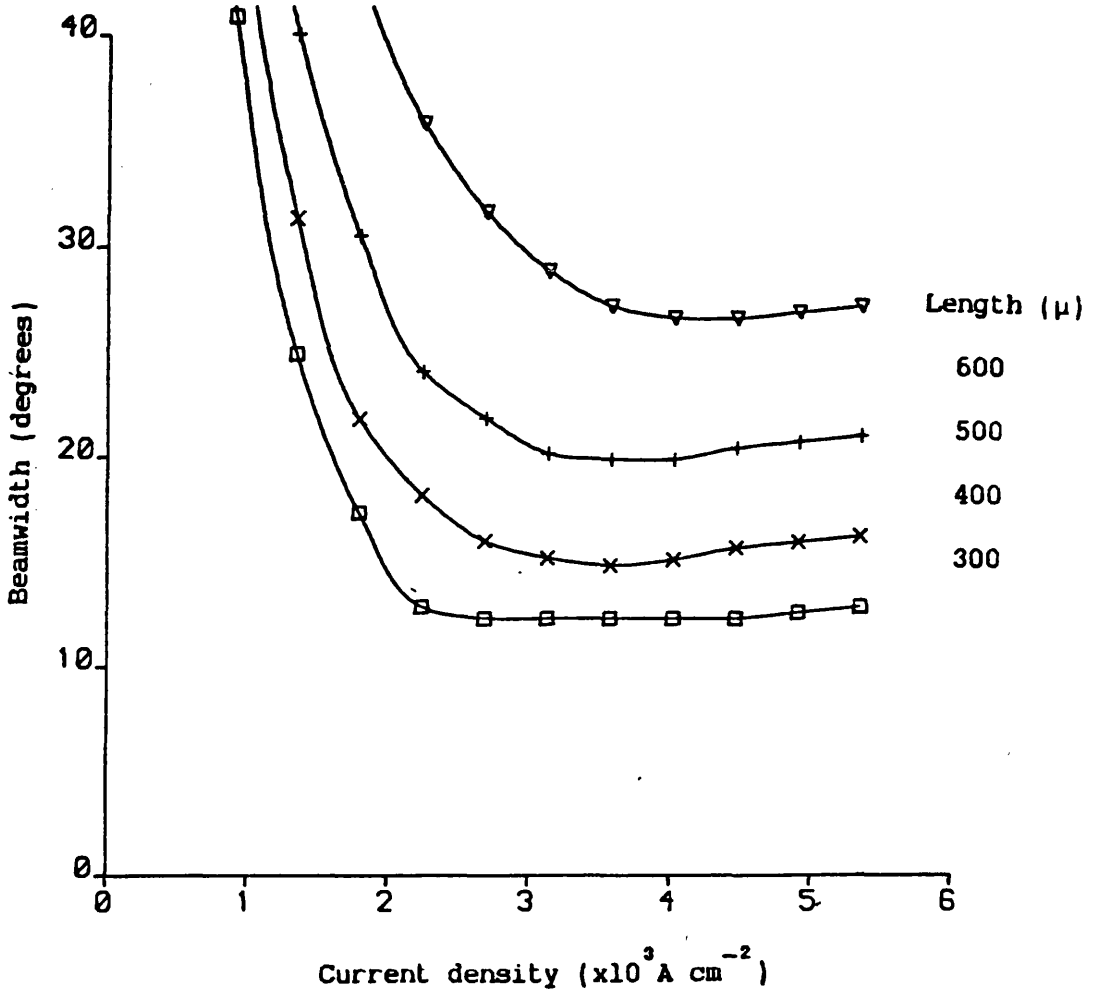

Fig(6.15) Variation of the beamwidth of an SLD, measured at half maximum power, with current density. The different curves correspond to different SLD lengths.

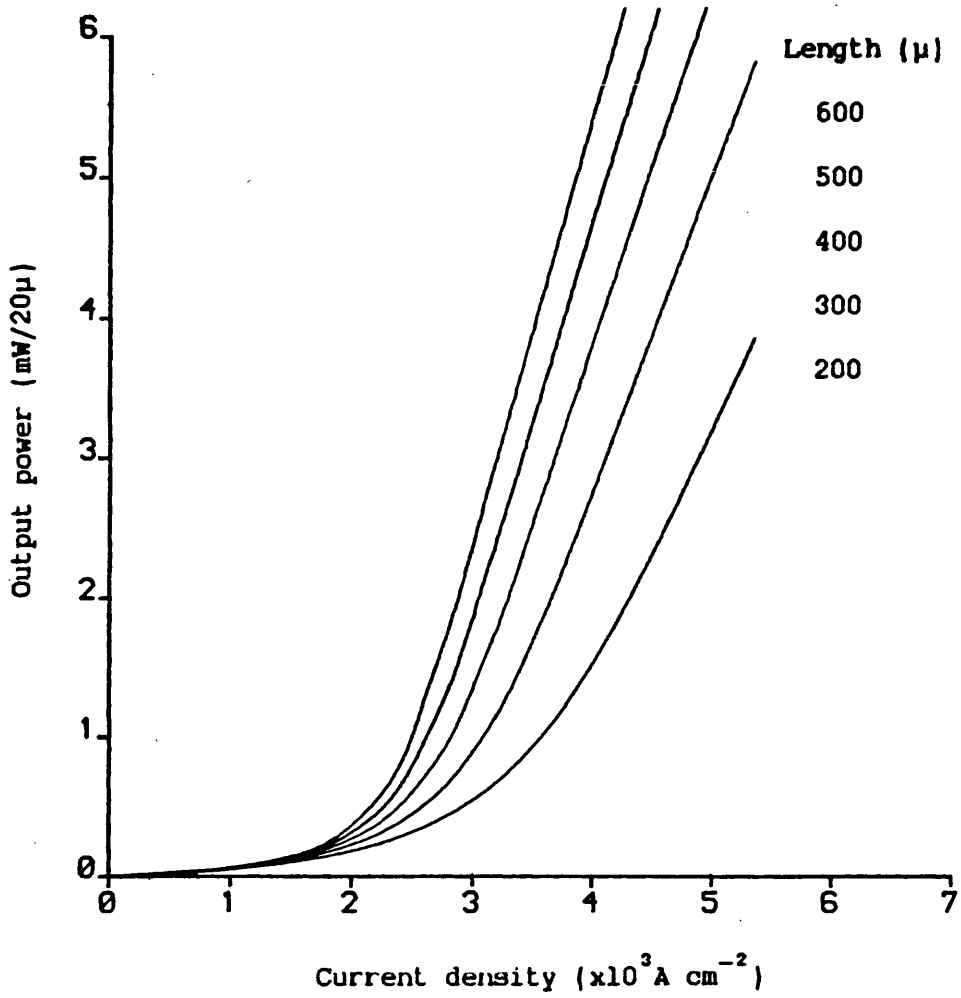

Fig(6.16) Variation of the output power of an SLD with current density for various stripe contact lengths.

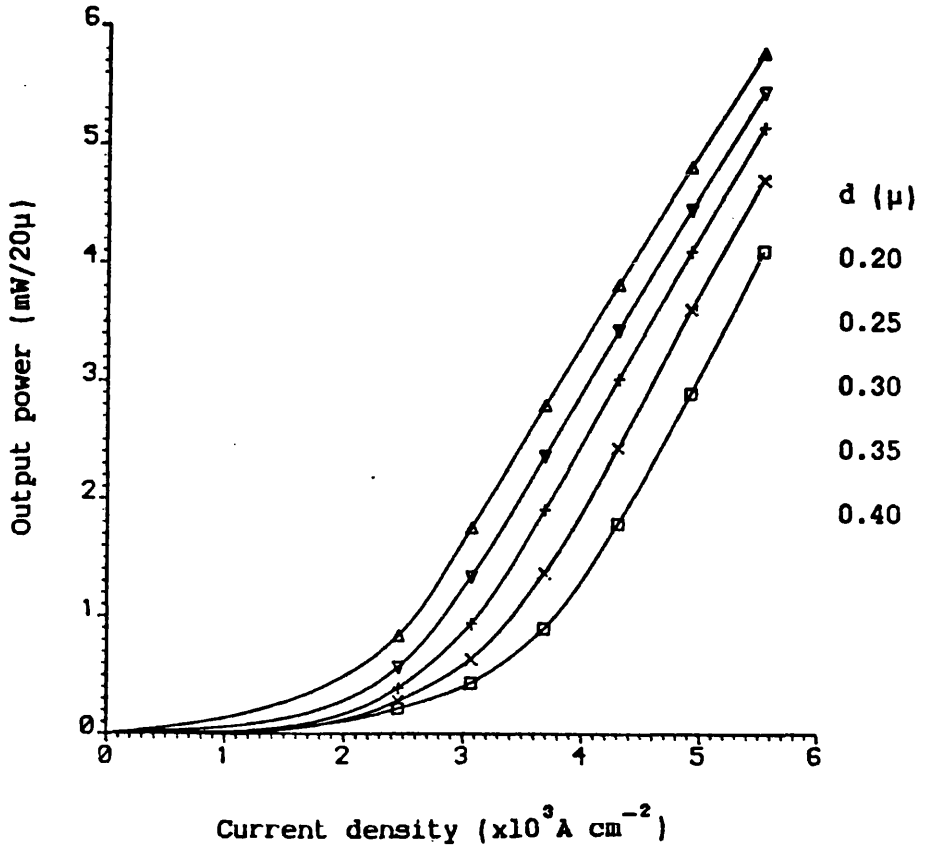

Fig(6.17) Variation of the output power of SLD A291 with current density shown as a function of active layer thickness, d.

has a peak value almost the same as before the active layer was reduced but which is spectrally broader.

An alternative method of increasing the efficiency of an SLD entails reducing the reflectivity of the front facet of an ordinary SLD with an anti-refection coating. This makes the device almost symmetrical in structure thereby reducing the amount of gain saturation that occurs towards the rear of the SLD. A comparison of the output power of an SLD with and without an anti-reflection coating is shown in fig(6.18). At low current densities there is little difference between the output powers of the coated and uncoated devices. However, at high current densities the output power of the coated SLD is increased by as much as four times compared to the casually expected increase of 1.4 due to the change in transmittivity of the front facet. A comparison of the carrier density variation with length with and without an anti-reflection coating, fig(6.19) and fig(6.2) respectively, confirms that the increase in the output power arises from the reduction in gain saturation towards the rear of the SLD. This method of increasing the ouput power of SLDs was first reported by Amann and Boeck, [6], who demonstrated a factor of four increase in output power experimentally. The spectral and far-intensity 'angular' distributions both narrow , when the output power is increased in this manner, however the change in their widths, at half maximum power, is very small and this probably explains the failure of Boeck and Amann to observe any change experimentally, [7]. This method of increasing the output power is by far the best as no extra drive current is necessary and no detrimental effects occur in the spectral and far-intensity distributions. It is also possible to combine this with an increase in stripe length to obtain an even larger increase

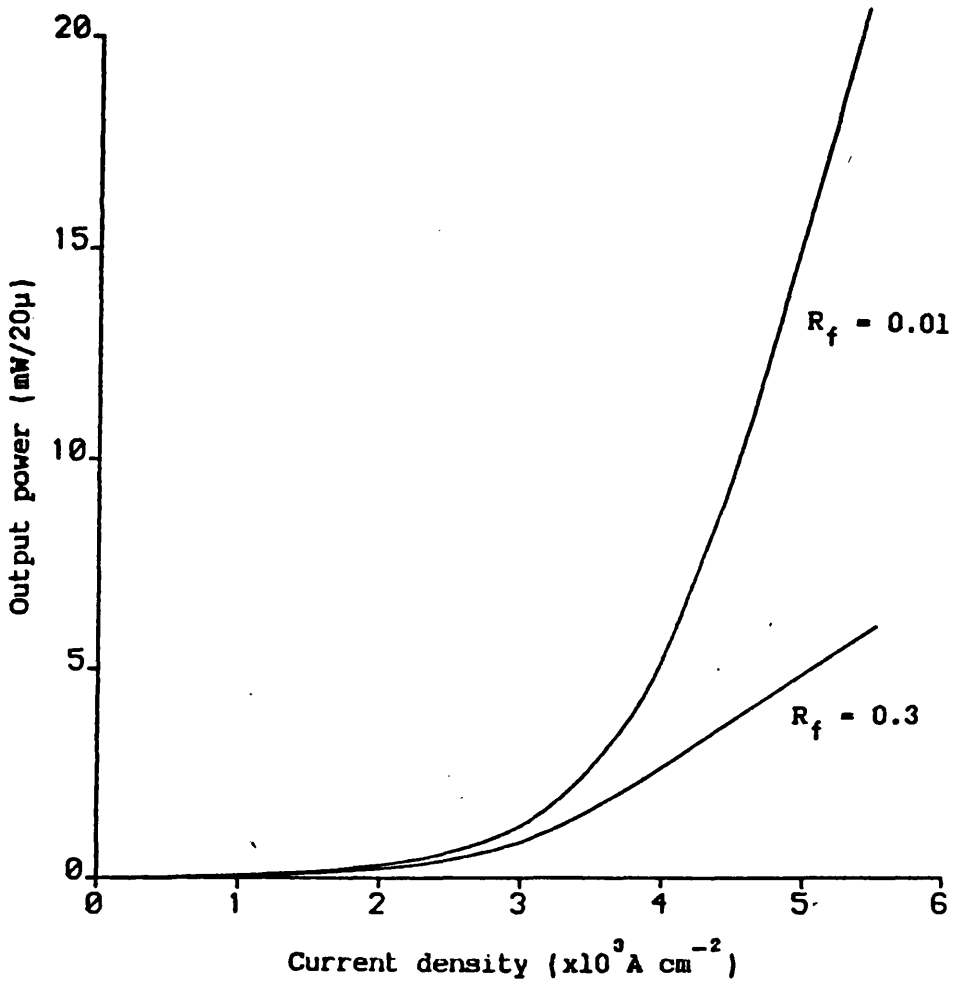

Fig(6.18) Comparison of the output power of an SLD with and without an antireflection coating.

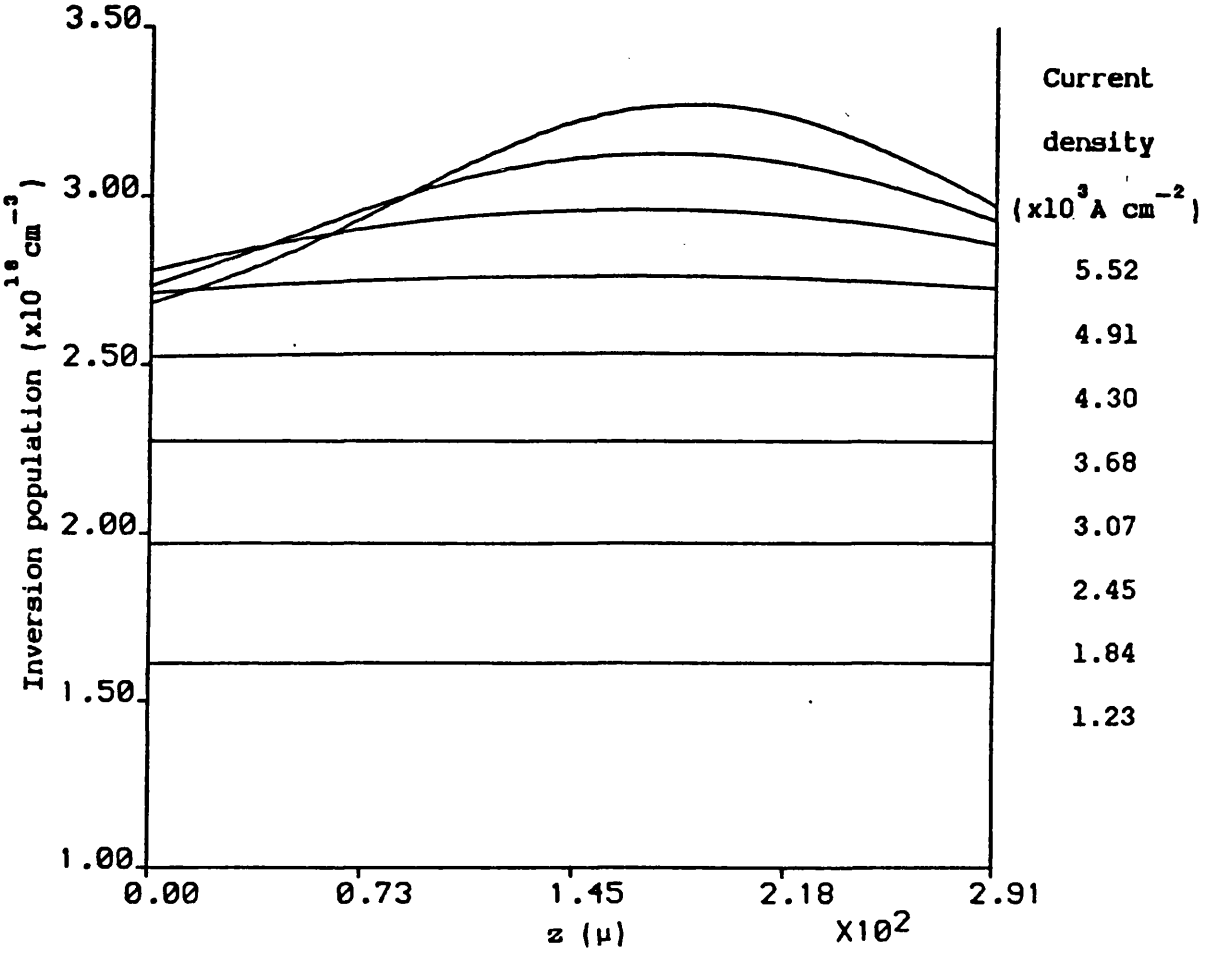

Fig(6.19) Variation of the inversion population with length of SLD A291 with an antireflection coating, R_f = 0.01.

in output power.

The photon distribution along the length of an SLD at high current densities shows a very asymetric distribution, fig(6.5). This means that there is a potentially high output power source available at $z = 0$ if the power can be extracted rather than being absorbed in the unstriped region of the SLD. The simplest method of obtaining this power would be to produce an SLD by reducing the reflectivity of one facet of a conventional stripe contact laser diode with an anti-reflection coating. It is however impossible to obtain much power from such a device with present day technology. The best anti-reflection coating quoted to date, is of the order of 0.01%, [8]. SLDs have been made by this method using anti-reflection coatings of this quality, [9], but the maximum output power achieved, before oscillations occurred was less than that obtained from a conventional SLD. An alternative method of reducing the reflectivity could be used such as positioning the stripe contact at an angle to the facet, [10]. This method is also somewhat impractical because the far-intensity angular distributions produced by such structures are very lop-sided making coupling to optical fibres or other optical devices difficult and extremely inefficient. Methods of overcoming this problem remain a particular challenge.

6.6 Concluding remarks.

The SLD model, developed in chapter 4, has been used to obtain detailed information about the photon and carrier density variation with length inside of the SLD. This information, along with some simple analytic approximations, has been used to describe the light/current characterisics, spectral and far-intensity 'angular' distributions of the SLD. In discussing the spectral distribution the

wavelength dependence of gain saturation has recieved special attention. Saturation of the photon density at one wavelength has been shown to occur not only with length but also with current density. This behaviour, however, is restricted to reverse travelling photons which are absorbed in the unstriped region at the rear of the SLD. In addition to describing the SLD's characteristics, ways of increasing the output power have been discussed together with the advantages and disadvantages of each method.

References.

1) 'Optooptic modulation based on gain saturation', R.W.Gray and L.W.Casperson, IEEE J. of Quant. Electron., vol.QE-14, p.893, 1978.

2) 'Proposals and analyses on laser amplifier based integrated optical circuits', K.Otsuka, IEEE J. of Quant. Electron., vol.QE-17, p.23, 1981.

3) 'The influence of technological parameters on spectral properties of double heterostructure Superluminescent diodes', Amann, Boeck and Harth, Frequenz, vol.45, p.635, 1978.

4) 'Wavelength dependence of gain saturation in GaAs lasers, E.O.Goebel, O.Hildebrand and K.Lohnert, IEEE J. of Quant. Electron., vol.QE-13, p.848, 1977.

5) 'Longitudinal effects on the spectral characteristics of edge-emitting LED's', J.Sarma, presented at the 4th IEEE Spec. Conf. on the Technol. of Electroluminescent Diodes, Brighton, 1980.

6) 'Spontaneous emission noise distribution from a gain-guided multimode waveguide', IEEE J. of Quant. Electron., vol.QE-19, p.1084, 1983.

7) 'High-efficiency superluminescent diodes for optical-fibre transmission', M.C.Amann and J.Boeck, Electronics letters, vol.15, No.2, p.41, 1979.

8) 'Measurement of modal reflectivity of an antireflection coating on a superluminescent diode', I.P.Kaminow, G.Eisenstein and L.W.Stutz, IEEE J. of Quant. Electron., vol.QE-19, p.493, 1983.

9) 'Lateral confinement InGaAsP superluminescent diode at 1.3μ', I.P.Kaminow, G.Eisenstein, L.W.Stutz and P.P.Dentai, IEEE J. of Quant. Electron., vol.QE-19, p.78, 1983.

10) 'Investigation of superluminescence emitted by a gallium arsenide diode', L.N.Kurbatov, S.S.Shakhidzhanov, L.V.Bystrova, V.V.Krapukhin

and S.I.Kolonenkova, Sov. Phys.-Semicond., vol.4, p.1739, 1982.

CHAPTER 7

POLARISATION CHARACTERISTICS OF SLDS

7.1 Introduction

It has been demonstrated that SLDs and SLD type structures can be used advantageously as light sources for fibre gyroscopes, [1,2]. The main advantage of SLDs over lasers when applied to fibre gyroscopes is their short coherence length which greatly reduces the ammount of Rayleigh backscattering, [2], a severe source of noise in fibre gyroscopes. It has also been suggested in [1] that the relatively unpolarised nature of the SLD's radiation can be used to good effect in reducing the polarisation noise in fibre gyroscopes. Although the polarisation light/current characteristics of SLDs have in the past been measured, [3,4], it seems that no previous model of the SLD has attempted to include any polarisation dependency. This information is important not only because of the SLD's application to fibre gyroscopes but also because the SLD provides useful information about active waveguides and associated structures. In particular the SLD gives an indication of the background spontaneous radiation (noise) one encounters in travelling wave laser amplifiers. This type of amplifier is basically a laser which has had an antireflection coating applied to both facets, and is in fact identical in structure to the Superradiance diode investigated in [2]. In this type of amplifier it has been demonstrated experimentally, [5], and shown theoretically, [6], that the amplification of a TM signal is not that much smaller than that for a TE signal. This suggests that the TM noise will also be of a comparable size to the TE noise so that simply filtering out the TM noise should produce a worthwhile

improvement in the signal to noise performance of the amplifier.

SLDs have quite different polarisation characteristics to double-heterostructure lasers which oscillate preferentialy in TE modes, i.e. with the electric field vector parallel to the junction plane, fig(7.1), [7]. The mode selectivity in lasers has been attributed to the polarisation dependent reflectivity of the cavity facets, [8]. In SLDs however the output is not dependent on feedback so that they might be expected to display a slight preference for the TM mode because the transmittivity is greater for this mode than it is for the TE mode. This, however, does not prove to be the case, experimental measurements, [3,4], showing that SLDs have a distinct preference for the TE polarisation, which increases with current density. Lee et al suggested in [3] that the favouring of the TE mode might arise from some property of the gain medium. It is known that the confinement factor for the TE mode is slightly greater than it is for the TM mode, see chapter(3) , so that the gain experienced by the TE mode is greater than that experienced by the TM mode. There is, however, a further parameter, the fraction of spontaneous emission coupling to the TE and TM modes, which may be at least be partly responsible for the observed polarisation behaviour of SLDs. The fraction of spontaneous emission coupling to the TE and TM modes is not necessarily equal, [9,10]. The SLD model developed in chapter(5) includes the facility for investigating the polarisation dependency of SLDs. The reflectivity, confinement factor and the spontaneous emission are all polarisation dependent parameters in the model. The SLD model not only predicts the polarisation dependency of the total light output power but also gives it's spectral variation. This provides the means for a further check between experiment and theory.

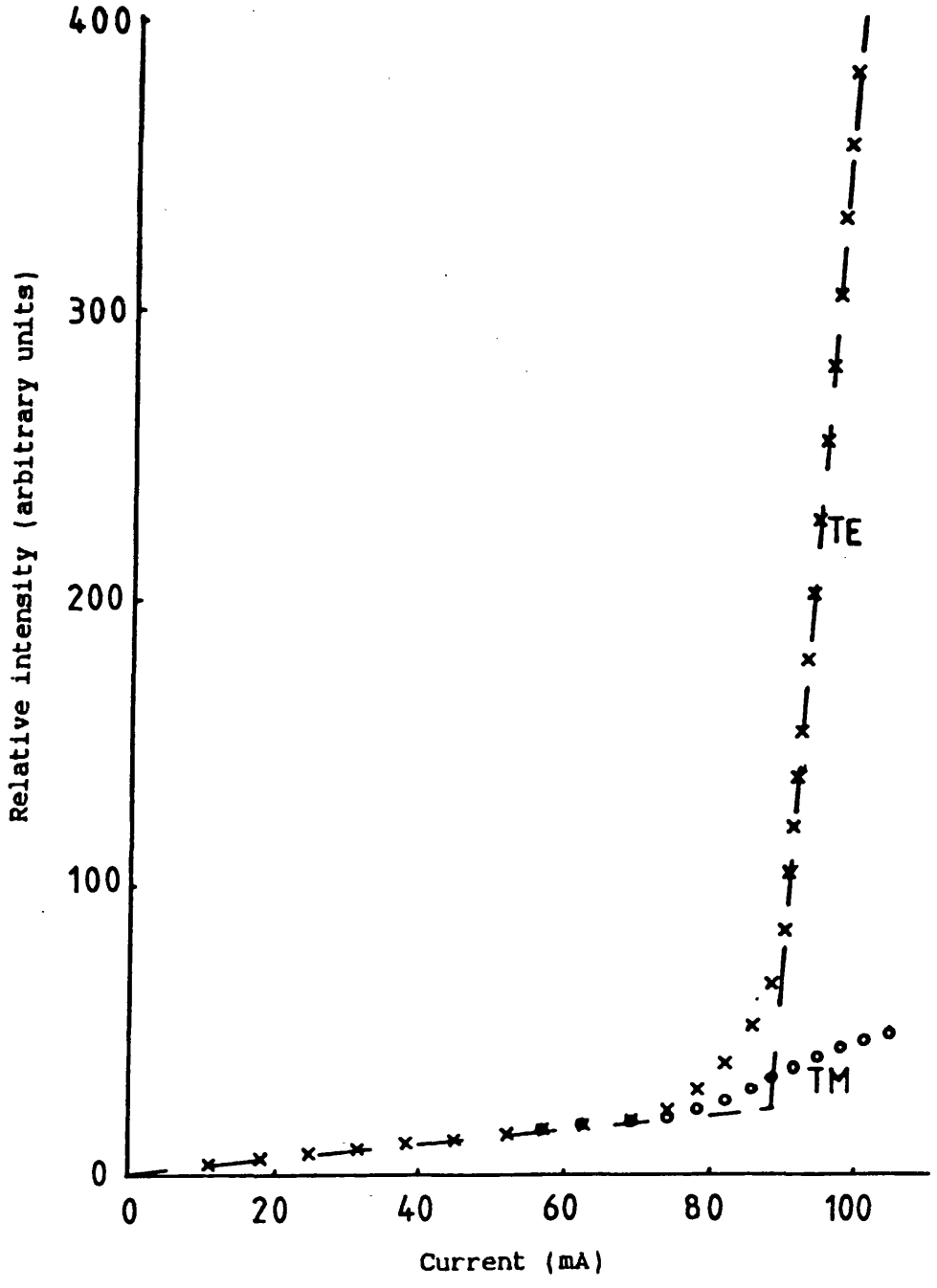

Fig(7.1) Polarisation dependent light/current characteristics of a typical laser, [7].

7.2 'Degree of Polarisation' measurements.

The light emitted by SLDs is partially polarised and is often described by a commonly used term, the degree of polarisation, DOP. This is defined as

$$DOP = \frac{(P_{TE} - P_{TM})}{(P_{TE} + P_{TM})} \times 100\ \% \qquad (7.1)$$

where P_{TE} and P_{TM} are the power in the TE and TM modes respectively. The factor of 100 simply converts the fraction into a percentage. This equation implies that the DOP is 100% when all of the power is in the TE modes, -100% when the radiation is totally from TM modes and zero if the light is unpolarised.

To obtain the degree of polarisation, DOP, of SLDs as a function of current density it is necessary to measure the light/current characteristics of both the TE and TM polarisations. Once this has been done it is a simple matter to obtain the DOP as a function of current density by applying equation(7.1). A Glan-Thompson prism polariser was used to make all of the polarisation measurements. This was first calibrated by allowing a beam from a Helium Neon laser, which is circularly polarised, to pass through the polariser onto a sheet of glass inclined at it's Brewster angle and observing the reflection from the glass. When the polariser is rotated to the point where the reflected beam from the glass vanishes only TE radiation is being transmitted through the polariser and the position of the polariser for TE transmission is known. The position of the polariser for TM transmission is at right angles to this.

The experimental arrangement for measuring the polarisation dependent light/current characteristics is similar to that which has

been previously described in section(6.3) for the light/current characteristics with the exception that now a Glan-Thompson polariser is inserted between the two objective lenses, fig(7.2). In the first instance a small numerical aperture (NA = 0.17) x10 objective was used to collect the SLDs rays thus limiting the maximum angle of capture to less than 10^0 half angle which, because of the high refractive index of GaAs ($\sim$3.5), corresponds to internal rays incident on the front facet at a maximum angle of 3^0 in the lateral plane. This precaution was taken to reduce any effect that rays striking the front facet at an angle in the lateral plane have upon the transmittivity of the TE and TM polarisations. It can be seen from fig(7.3) that the plane wave reflectivity for TE and TM waves is approximately equal up to an angle of 5^0. When the x10 objective was replaced by a x45 (NA=0.65) objective there was virtually no change in the results even though the internal capture angle was increased to 10^0 and the plane wave reflectivity for TE and TM waves are no longer equal at such large angles, fig(7.3). This is not surprising of course, because the bulk of the power is contained in the on-axis rays and these dominate the SLD's properties.

Measurements were made with the polariser positioned to transmit the TE polarisation power and also with the polariser rotated by 90^0 to transmit the TM polarisation power. These measurements were checked by rotating the polariser 90^0 twice and taking further measurements at each position. This precaution is necessary because if the polariser is not perfectly perpendicular to the incident beam the beam can be deflected from its true path leading to a certain degree of experimental error. These errors, although not very large, are compounded when the degree of polarisation is calculated. It can be seen from fig(7.4) that this

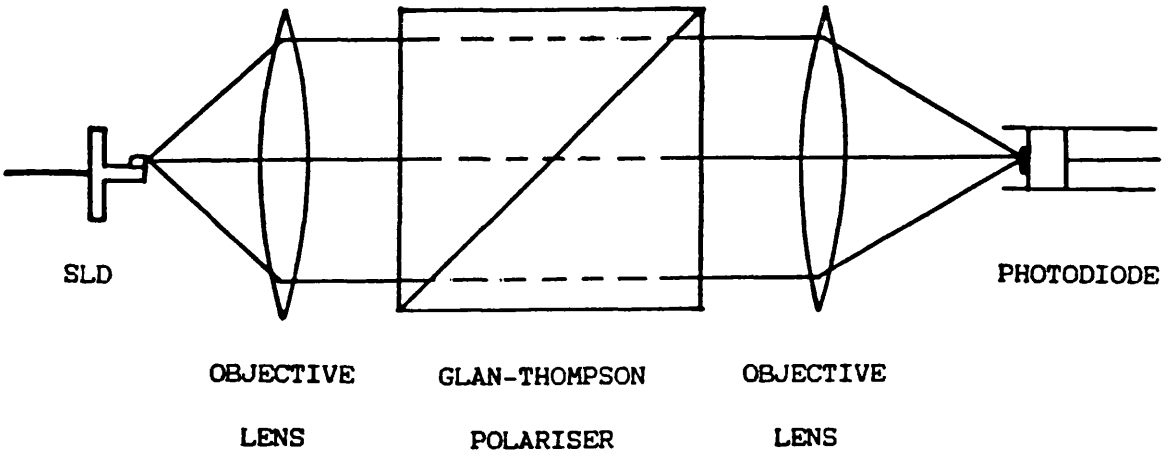

Fig(7.2) Schematic diagram of the polarisation dependent light/current characteristic measurement system.

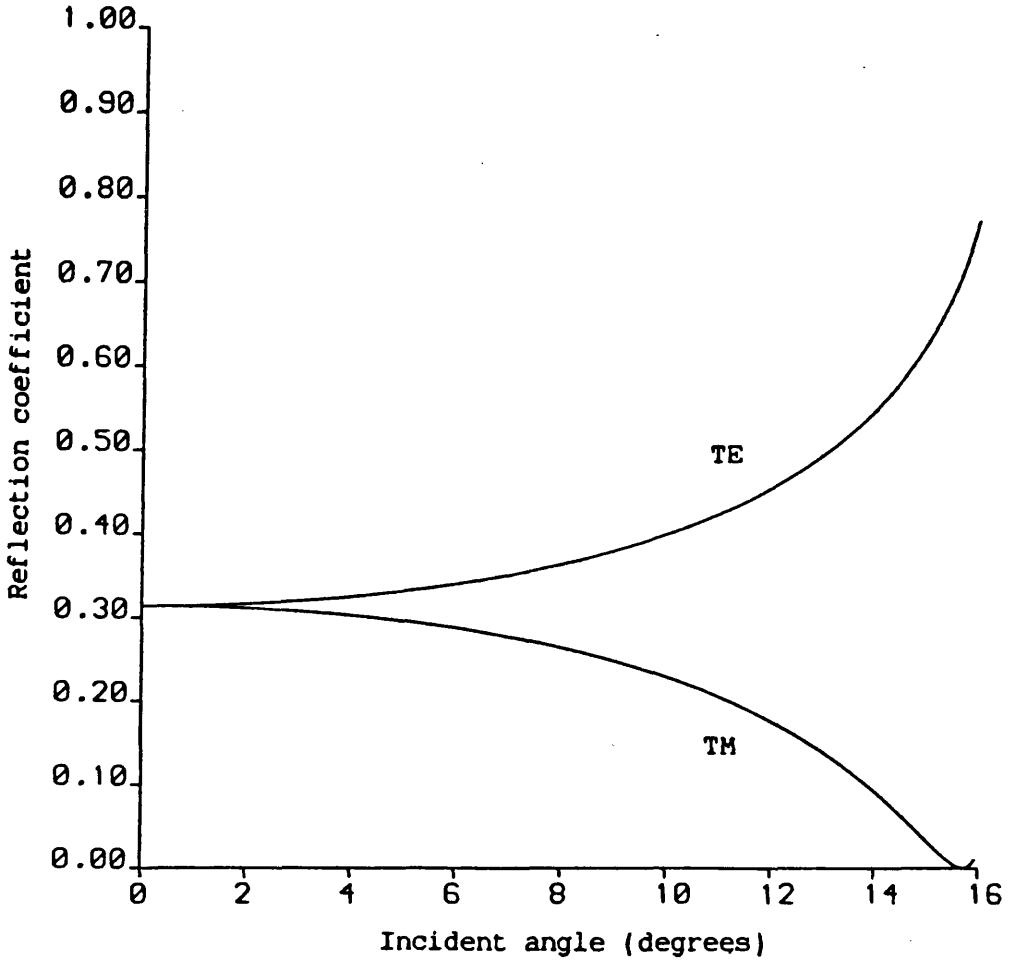

Fig(7.3) Plane wave reflectivity of GaAs showing the spliting of the TE and TM polarisations that occurs as the incident angle is increased.

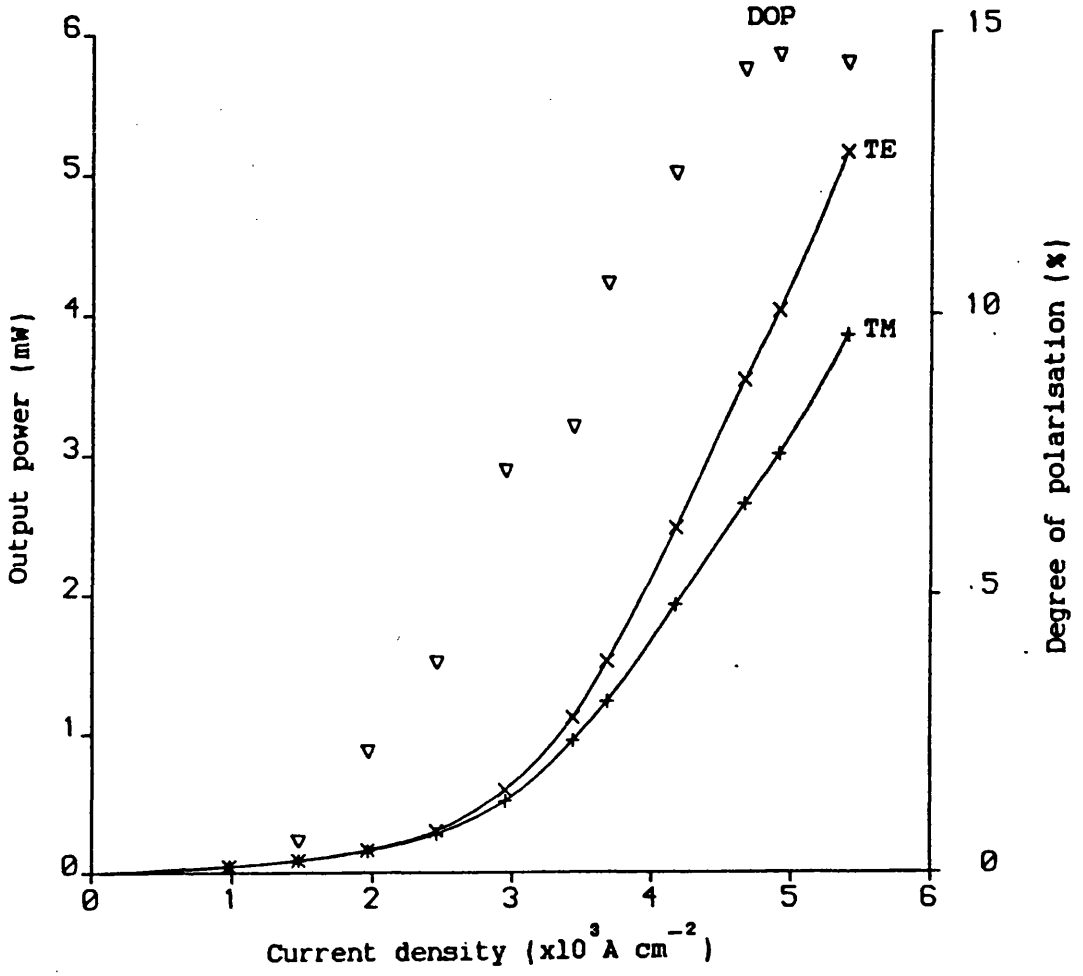

Fig(7.4) Experimental polarisation characteristics of SLD A291 shown as a function of current density. The degree of polarisation (DOP) is also shown.

tends to produce a scatter of points in the DOP plot compared to the more uniform curves of the TE and TM light/current characteristics.

7.3 Comparison of theory and experiment.

The SLD model described in chapter(4) contains three variables, reflectivity, confinement factor and the fraction of spontaneous emission entering a mode, that are polarisation dependent. In chapters (5) and (6) average values for these parameters were used to obtain results that are independent of polarisation. Now, however, it is necessary to include their polarisation dependent values. Expressions for the TE and TM confinement factors have previously been given in chapter(3), equations (3.56 and 3.60) respectively, which for the active layer thickness of the measured devices (d = 0.3) and the refractive indices of the active and passive layers (n_1 = 3.55 and n_2 = 3.38) give Γ_{TE} = 0.76 and Γ_{TM} = 0.72. The polarisation dependent reflectivities for the fundamental TE and TM modes are shown in fig(7.5), [11], as a function of active layer thickness for various refactive index steps between the active and passive layers. For the values of refractive indices and active layer thickness quoted above R_{TE} = 0.38 and R_{TM} = 0.26. Although the polarisation dependencies of the reflectivity and confinement factor are well documented the same cannot be said for the fraction of spontaneous emission coupling to each mode. The theory for calculating this quantity is extremely complicated and its value was therefore determined empirically by matching theoretical DOP results with experimental measurements. This was done initially for the SLD, A291, designated as the master device in chapter(5), by varying the fraction of spontaneous emission into each mode. Some theoretical results are shown in fig(7.6) for

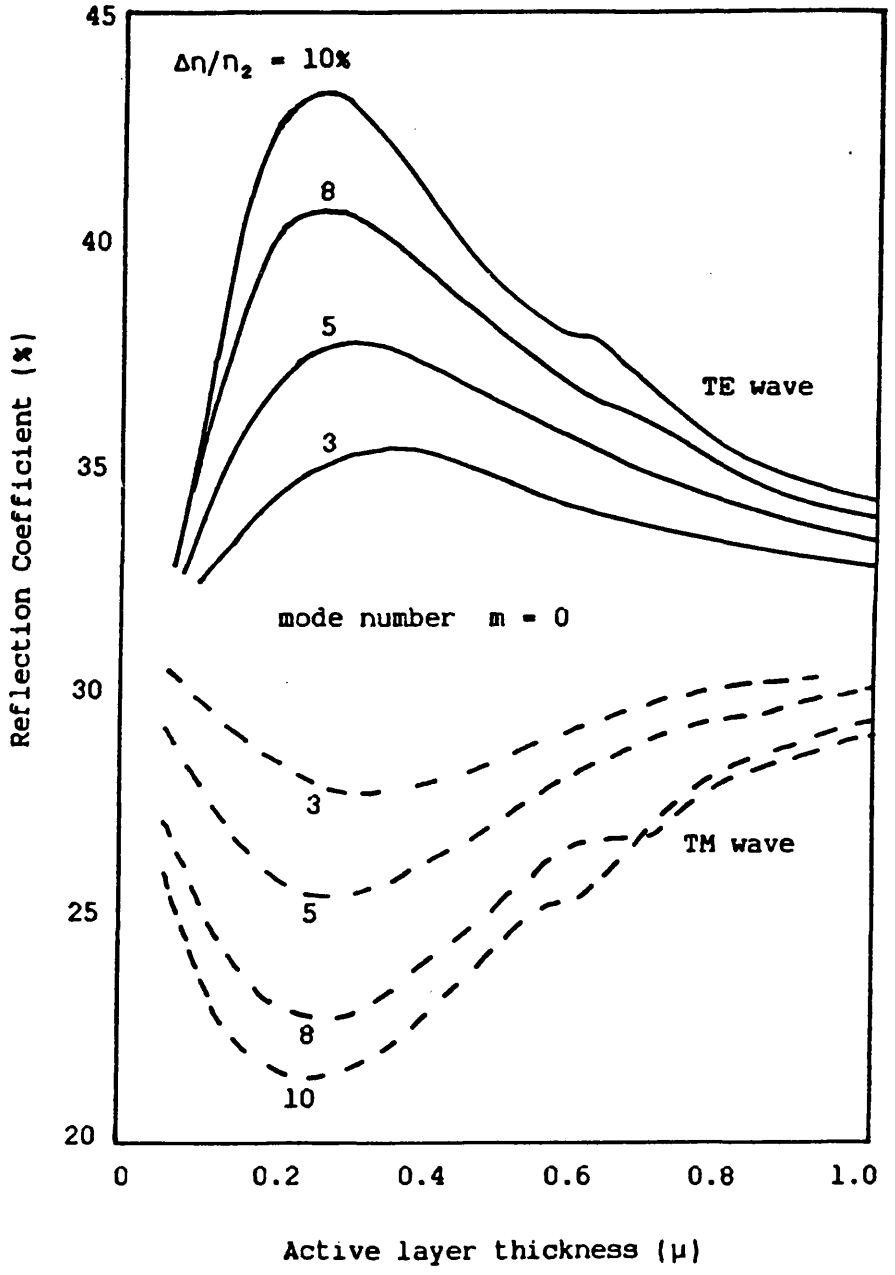

Fig(7.5) Reflection coefficient for the fundamental mode as a function of active layer thickness for symmetric DH laser. $\Delta n/n_2 = (n_2 - n_1)/n_2 \times 100\%$, [11].

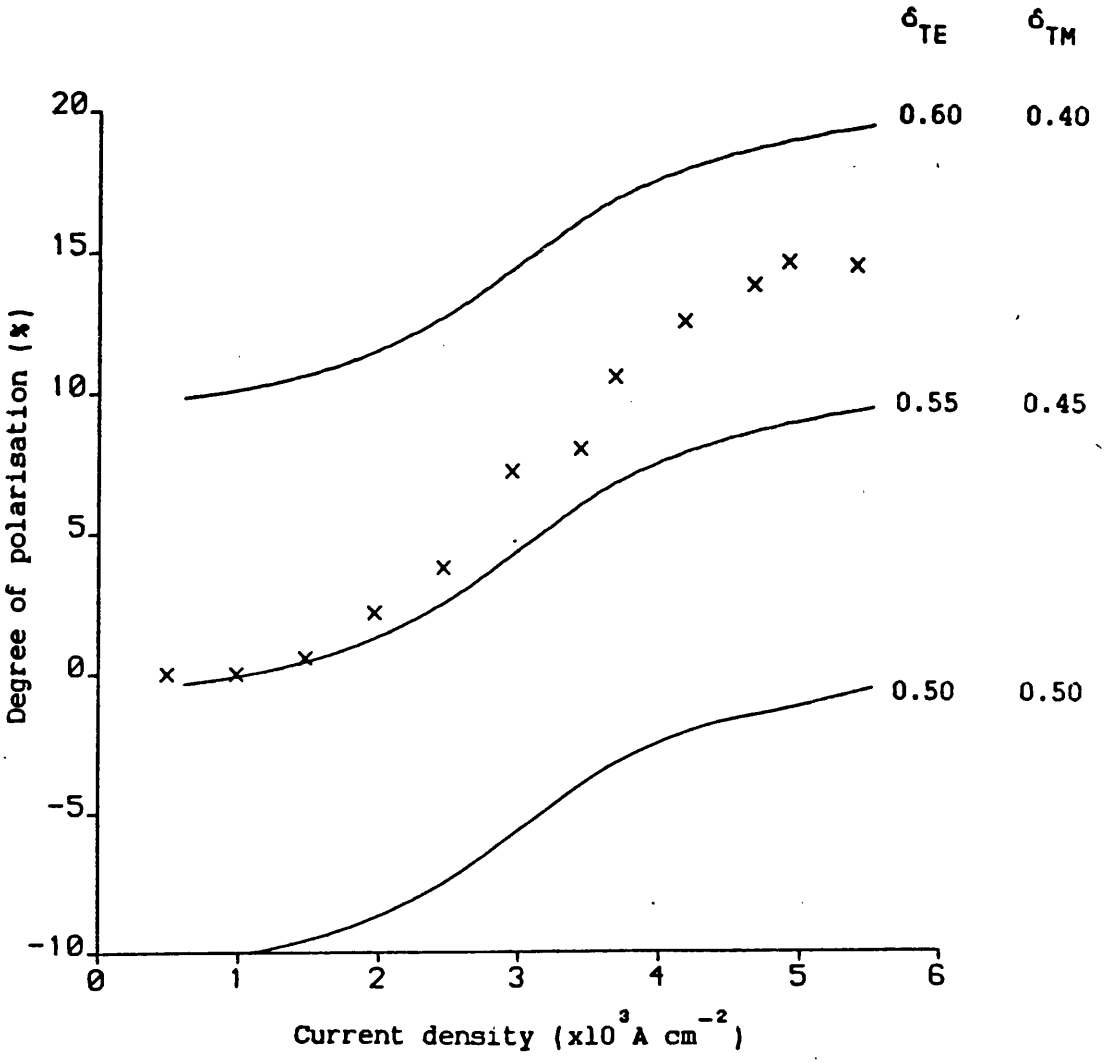

Fig(7.6) Degree of polarisation v current density for SLD A291. The solid curves represent theoretical calculations for varying fractions of spontaneous emission entering the TE and TM modes, Γ_{TE} = 0.76 and Γ_{TM} = 0.72, R_{TE} = 0.38 and R_{TM} = 0.26.

various fractions of spontaneous emission entering each mode together with some experimental results for comparison. It can be seen that when the fraction of spontaneous emission entering the TE and TM modes are equal, i.e. $\delta_{TE} = \delta_{TM} = 0.5$, the theoretical DOP is negative for all current densities indicating that the fraction of spontaneous emission entering the TE mode must be greater than that entering the TM mode; i.e. $\delta_{TE} > \delta_{TM}$ is required if a reasonable match with the experimental results is to be obtained. When $\delta_{TE} = 0.6$ and $\delta_{TM} = 0.4$ the theoretical DOP results are too high throughout the current density range. Much better results are obtained if $\delta_{TE} = 0.55$ and $\delta_{TM} = 0.45$, however, the theoretical change in the DOP with current density is less than that in the experimental results. This suggests that the values used for the TE and TM confinement factors, the only other polarisation dependent parameter that changes with current, may be in error. The DOP proved to be fairly sensitive to any change in the confinement factors as fig(7.7) illustrates. In this graph the fraction of spontaneous emission entering each mode is kept constant, $\delta_{TE} = 0.55$ and $\delta_{TM} = 0.45$, and the difference in the confinement factors varied. It was found that with $\Gamma_{TE} = 0.77$ and $\Gamma_{TM} = 0.71$ an improved match was obtained with the experimental results. Although these values differ from the calculated values the difference is not that great for the values to be considered unreasonable. The best possible agreement with the experimental results was obtained with $\delta_{TE} = 0.555$ and $\delta_{TM} = 0.445$ and $\Gamma_{TE} = 0.77$ and $\Gamma_{TM} = 0.71$, fig(7.8).

Having adopted these values for the master SLD theoretical results were calculated for the remaining SLDs by changing only their stripe contact dimensions. The results for the remaining SLDs from wafer(A) are shown in fig(7.9) while those from wafer(B) are given in

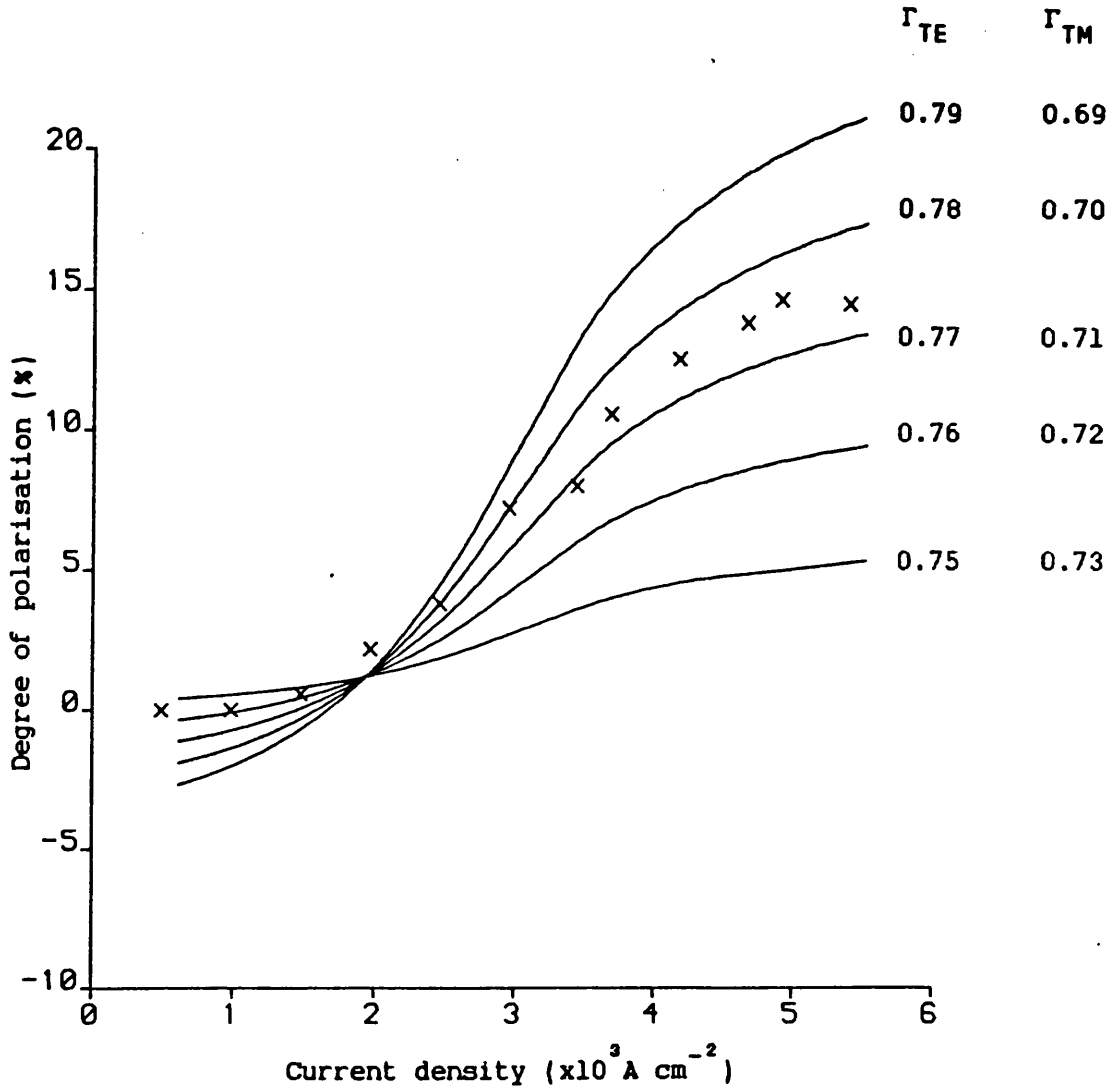

Fig(7.7) Degree of polarisation v current density for SLD A291. The solid curves represent theoretical calculations for various TE and TM confinement factors. δ_{TE} = 0.55 and δ_{TM} = 0.45 R_{TE} = 0.38 and R_{TM} = 0.26.

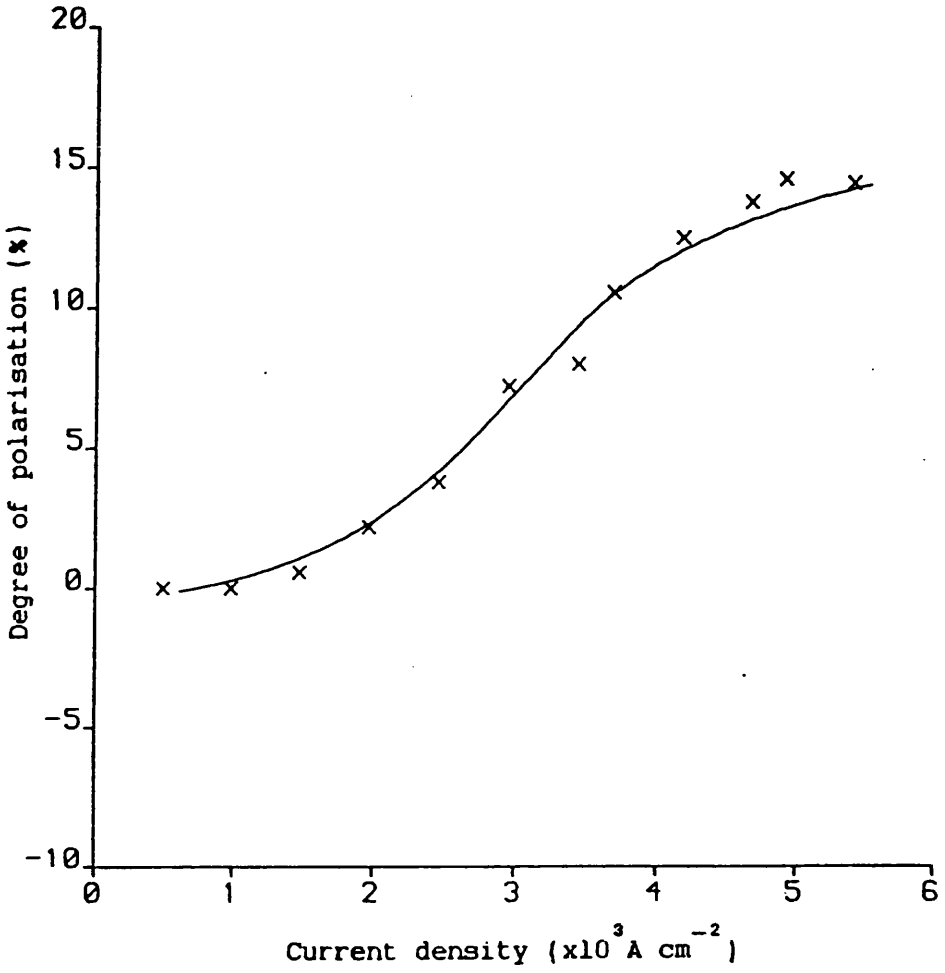

Fig(7.8) Degree of polarisation v current density for SLD A291. This graph shows the best agreement that was obtained between experiment and theory. δ_{TE} = 0.555 and δ_{TM} = 0.455, Γ_{TE} = 0.77 and Γ_{TM} = 0.71, R_{TE} = 0.38 and R_{TM} = 0.26.

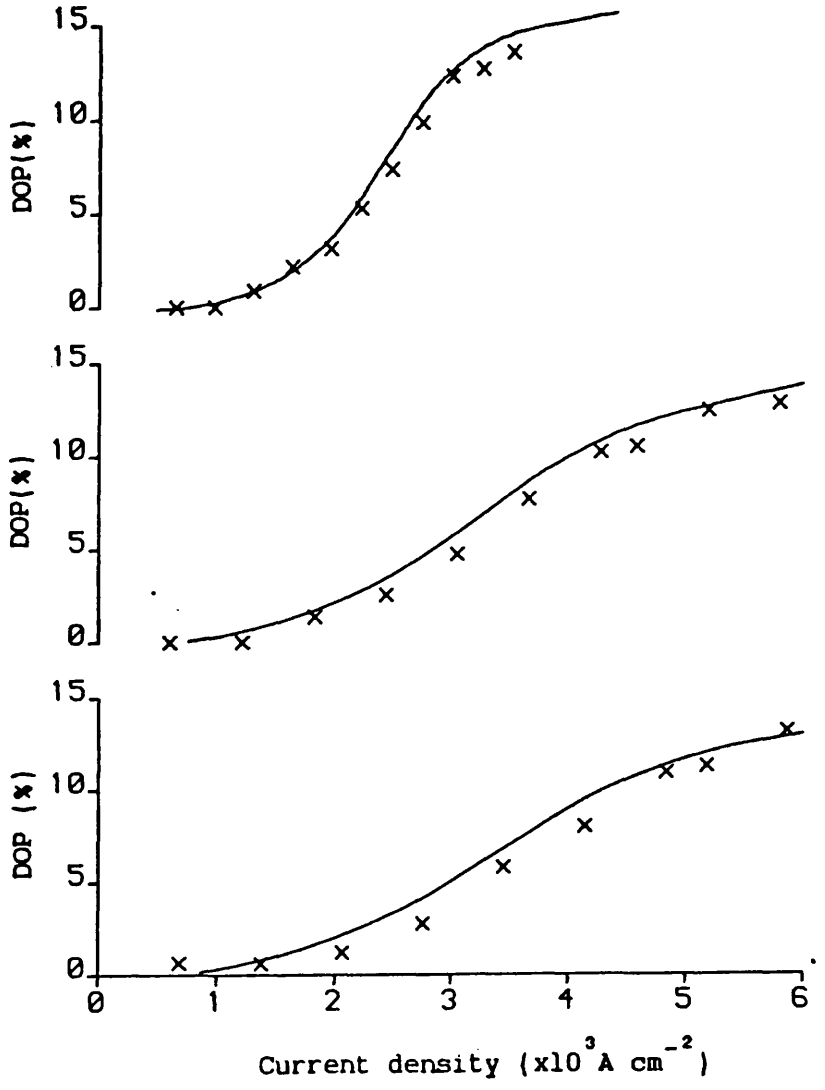

Fig(7.9) Comparison of the variation of the degree of polarisation with current density for SLDs A547 (top), A234 (middle) and A207 (bottom). Parameters as for fig(7.8).

fig(7.10). It can be clearly seen that all of the SLDs from both wafers show very similar trends and the agreement between theory and experiment is very good.

A great deal of insight into why the SLD displays the observed polarisation characteristics it does can be obtained from a much simplified version of the photon conservation equation for the forward travelling flux, equation(4.16).

$$\frac{dP_k}{dz} = \Gamma_k g(N) P_k + \delta_k R_{spon}(N) \qquad (7.2)$$

In this equation all the angular and spectral dependencies have been removed leaving the suffix 'k' to represent the polarisation dependencies. Under low injection current conditions the inversion population may be taken to be constant along the length and an analytic solution of equation(7.2) can be obtained.

$$P_k(L) = \frac{\delta_k R_{spon}(N)}{\Gamma_k g(N)} (\exp(\Gamma_k g(N) L) - 1) \qquad (7.3)$$

$P_k(L)$ represents the photon density just inside the output facet and this must be multiplied by the transmittivity of the facet to obtain the actual output photon density, $P_k(out)$.

$$P_k(out) = \frac{\delta_k R_{spon}(N)}{\Gamma_k g(N)} (\exp(\Gamma_k g(N) L) - 1)(1 - R_k) \qquad (7.4)$$

If equation(7.4) is combined with equation(7.1) an expression for the DOP is obtained.

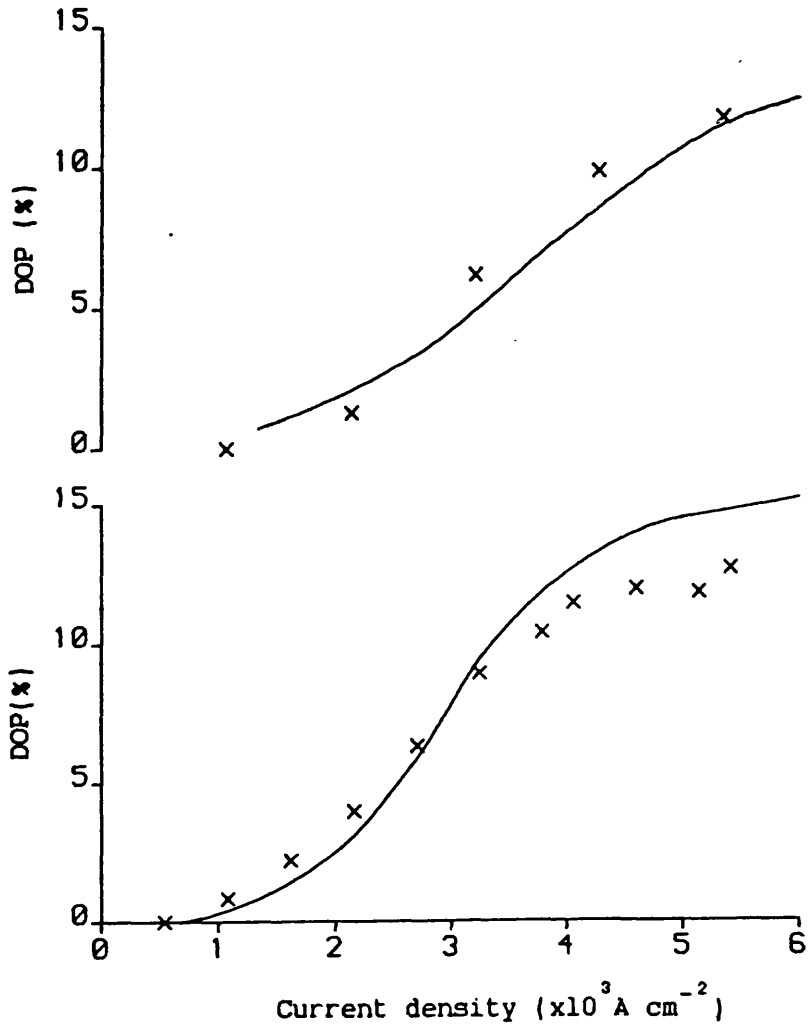

Fig(7.10) Comparison of the variation of the degree of polarisation with current density for SLDs B180 (top) and B330 (bottom). Parameters as for fig(7.8).

$$DOP = \frac{\frac{(1-R_{TE})\delta_{TE}}{\Gamma_{TE}}(\exp[\Gamma_{TE}g(N)L]-1) - \frac{(1-R_{TM})\delta_{TM}}{\Gamma_{TM}}(\exp[\Gamma_{TM}g(N)L]-1)}{\frac{(1-R_{TE})\delta_{TE}}{\Gamma_{TE}}(\exp[\Gamma_{TE}g(N)L]-1) + \frac{(1-R_{TM})\delta_{TM}}{\Gamma_{TM}}(\exp[\Gamma_{TM}g(N)L]-1)} \qquad (7.5)$$

It becomes apparent from this equation that the change in the DOP with inversion population, (current density), is entirely governed by the difference in the exponential terms, i.e the difference in the TE and TM confinement factors. This agrees with the numerical results shown in figs(7.6) and (7.7) where changing the fraction of spontaneous emission coupling into the TE and TM modes did not alter the change in the DOP with current density but altering the difference in the TE and TM confinement factors did. Further verification of the fact that the change in the DOP with current density depends only on the difference in the confinement factors can be obtained by calculating the prefactors to the exponential terms in equation(7.5) using the values of R, δ and Γ that gave the desired agreement between theory and experiment for the DOP curves.

$$\frac{(1-R_{TE})\delta_{TE}}{\Gamma_{TE}} = 0.4613 \qquad \frac{(1-R_{TM})\delta_{TM}}{\Gamma_{TM}} = 0.4614$$

The prefactors are almost exactly equal and cancel in equation(7.5) to leave only the exponential terms.

Equation(7.5) can be simplified further by considering the case where the local gain, g(N), is approximately zero. In this case the exponential can be expanded producing

$$P_k(out) = \frac{\delta_k R_{spon}(N)}{\Gamma_k g(N)}(1 + \Gamma_k g(N)L - 1)(1 - R_k) \qquad (7.6)$$

which reduces to

$$P_k(\text{out}) = \delta_k R_{spon}(N)L(1 - R_k) \qquad (7.7)$$

so that the DOP may be written as

$$\text{DOP} = \frac{(1-R_{TE})\delta_{TE} - (1-R_{TM})\delta_{TM}}{(1-R_{TE})\delta_{TE} + (1-R_{TM})\delta_{TM}} \qquad (7.8)$$

and depends only on the reflectivity and the fraction of spontaneous emission entering the TE and TM modes. This, coupled with the knowledge that it is only the confinement factor that produces a variation of the DOP with current density, suggests that the combination of the TE and TM reflectivities and fraction of spontaneous emission entering each mode required to give a good match between experiment and theory is not unique. This hypothesis proved to be correct, a number of combinations giving good agreement between theory and experiment. An example is shown in fig(7.11) in which the fracion of spontaneous emission is taken to be equal into each mode and $R_{TE} = 0.305$ and $R_{TM} = 0.335$. These values of reflectivities are however somewhat unrealistic because if they were in fact correct double heterostructure lasers would lase in the TM mode and not the TE mode. This leads to the conclusion that the use in this model of the values of reflectivity calculated by Ikegami, [11], $R_{TE} = 0.38$ and $R_{TM} = 0.26$ and the fractions of spontaneous emission entering each mode $\delta_{TE} = 0.555$ and $\delta_{TM} = 0.445$ are more realistic, fig(7.8).

7.4 Polarisation dependent spectra

In the previous section it has been shown that the theoretical model of the SLD produces good agreement with experimental DOP measurements when certain specific polarisation

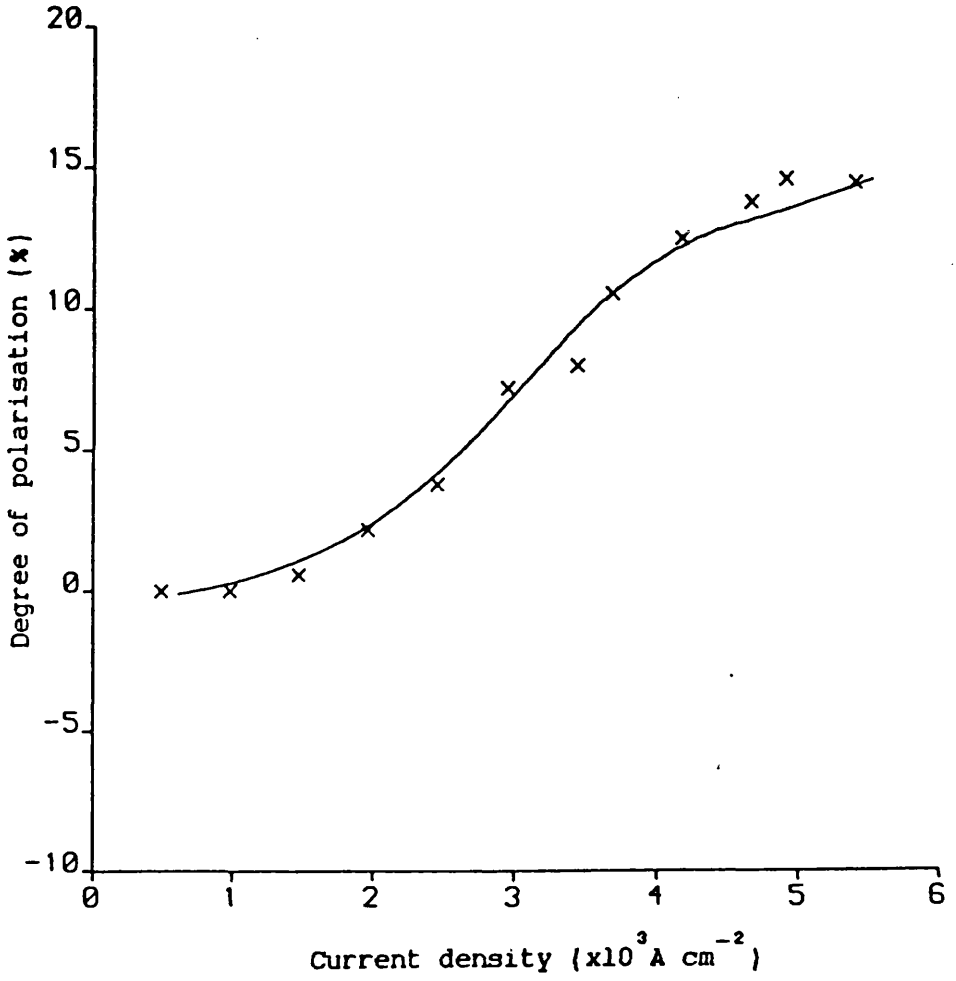

Fig(7.11) Degree of polarisation v current density for SLD A291, showing that, when the fraction of spontaneous emission entering the TE and TM modes is equal, the TM reflectivity must be larger than the TE reflectivity if a good match between theory and experiment is to be obtained.
The parameters used were $\delta_{TE} = 0.5$ and $\delta_{TM} = 0.5$, $\Gamma_{TE} = 0.77$ and $Q_{TM} = 0.71$, $R_{TE} = 0.305$ and $R_{TM} = 0.335$.

dependent parameters are used. The theoretical model also predicts the TE and TM spectral distributions. These results are automatically obtained from the model and therefore provide a further means of testing it. To do this it was necessary to measure the polarisation dependent spectra of the SLDs.

To measure the TE and TM spectral distributions a monochromator was inserted between the polariser and the objective lens that focuses the beam onto the photodetector. Unfortunately it is not possible to make direct polarisation measurements by simply rotating the polariser by 90^0 because the optics within the monochromator is polarisation dependent. This became immediately obvious when an initial test run was made because the measured TM power was greater than the TE power throughout the whole spectrum of the SLD. This contradicts the fact that the total TE power is always greater than the total TM power. It is therefore necessary to eliminate the polarisation dependent properties of the monochromator to obtain a true picture of the TE and TM spectral distributions. The simplest method of overcoming this problem is to include a half wavelength retardation plate between the polariser and the monochromater. This allows the beam to be rotated by 90^0 when the polariser is positioned for TM transmission so that the monochromator always recieves a 'TE polarised beam'. Unfortunately a half wavelength retardation plate was not readily available for this experiment so an alternative method of achieving the same effect was used. This involved actually rotating the SLD itself by 90^0 to effectively turn the polarisation reference also by 90^0.

Althougth this method is quite simple in principle, in practice, great care is needed when rotating the SLD by 90^0 because this can alter the ammount of power entering the monochromator. It is

therefore necessary to ensure that the distance between the collection lens, polariser and the monochromator entrance slit are kept to a minimum so that when the SLD's stripe width is perpendicular to the entrance slit the image of the SLD falls totally within the slit. As an added precaution the width of the monochromator's slits were increased from 0.1mm, used for the spectral measurements described in section(5.3), to 0.2mm. This reduces the spectral resolution of the monochromator to 5nm which, although quite large, is still sufficient for this experiment.

To further reduce any experimental error, introduced by rotating the SLD, measurements were taken for both the TE and TM polarisations with the stripe width of the SLD at right angles to the monochromator's entrance slit and also with the SLD's stripe width in the same plane as the monochromator's entrance slit. By utilisng these two pairs of measurements a ratio of the TE to TM spectra can be obtained. When the stripe width of the SLD is perpendicular to the monochromator's slit and the polariser is positioned to transmit TE polarised light the power transmitted through the monochromator can be designated $A.P_{TE}$ where A is the transmission factor for TE polarised light. Similarly, when the polariser is positioned to transmit TM polarised light the power transmitted through the monochromator can be designated $B.P_{TM}$ where B is the transmission factor for TM polarised light. When the SLD is rotated by 90^{0}, so that it's stripe width lies in the same plane as the monochromator's entrance slit, the polarisation reference plane is also rotated by 90^{0}; i.e. when the polariser is positioned to transmit TE polarised light it actually transmits TM polarised light. This means that the measured TE polarised light experiences the monochromator's TM transmission factor, B, and the transmitted power is $B.P_{TE}$.

Similarly when the polariser is positioned to transmit TM polarised light it actually transmits TE polarised light so that the measured TM polarised light experiences the monochromator's TE transmission factor, A, and the transmitted power is $A.P_{TM}$. If the two TE measurements are now summed and the ratio taken with the sum of the two TM measurements the monochromator's transmission factors are eliminated, i.e.

$$\frac{A.P_{TE} + B.P_{TE}}{B.P_{TM} + A.P_{TM}} = \frac{(A + B).P_{TE}}{(B + A).P_{TM}} \qquad (7.9)$$

This method therefore gives the ratio of TE to TM for the spectral distributions of the SLD which is adequate because only relative power measurements are possible with this arrangement.

The wavelength scanning mechanism of the monochromator was driven with a linear motor which was also used to drive the x-direction of an x-y recorder. The output from the photodetector was fed via a box-car averager to the y-direction of the x-y recorder allowing a hard copy of the spectral distribution to be obtained. It was necessary to use the box-car averager to reduce the amount of noise because only very small powers are obtained at the two extremes of the spectrum. From the spectral plots it was possible to obtain the variation of the DOP with wavelength for a range of current densities. The errors can be quite large near the two extremes of the spectra because of the nature of the DOP calculation. Unlike the calculation for the total power DOP, which only involves inserting measured values into equation(7.1), this calculation involves first summing the two TE and TM measurements with the active layer of the SLD in the vertical and horizontal positions, before evaluating equation(7.1). This therefore leads to an increase in the error of

the measured DOP.

7.5 Comparison of theoretical and experimental polarisation dependent spectra.

It has already been mentioned that the theoretical polarisation dependent spectral distribution of the SLD is automatically calculated by the SLD model. Figs (7.12) and (7.13) show an example of how this compares with experimental measurements for the SLD, A291. These particular graphs show the TE and TM spectral distribution for two different current densities. The agreement between experiment and theory is quite good. However, this method of displaying the data makes it difficult to spot the fact that the TE and TM curves actually cross at the high energy side of the spectrum, figs (7.12) and (7.13). A much better and more informative way of representing the same picture is to plot the variation in the DOP with wavelength, fig(7.14). This figure shows the spectral variation in the DOP at the two current densities corresponding to figs (7.12) and (7.13) and also at a slightly lower current density. The match between theory and experiment is quite good at the higher current densities, although not quite so good at the lowest current density. There is also a larger discrepency towards the high energy side of the spectrum, with the experimental DOP becoming more negative than the theoretical calculations predict. It is however more important to point out that in all cases both the experimental and theoretical DOPs have the same general shape and do ,in fact, become negative at short wavelengths (high energies) i.e the TE and TM spectral curves cross. These features are expected because the analytic approximation, equation(7.5), shows that the DOP depends entirely on the TE and TM modal gains. Hence the DOP peaks

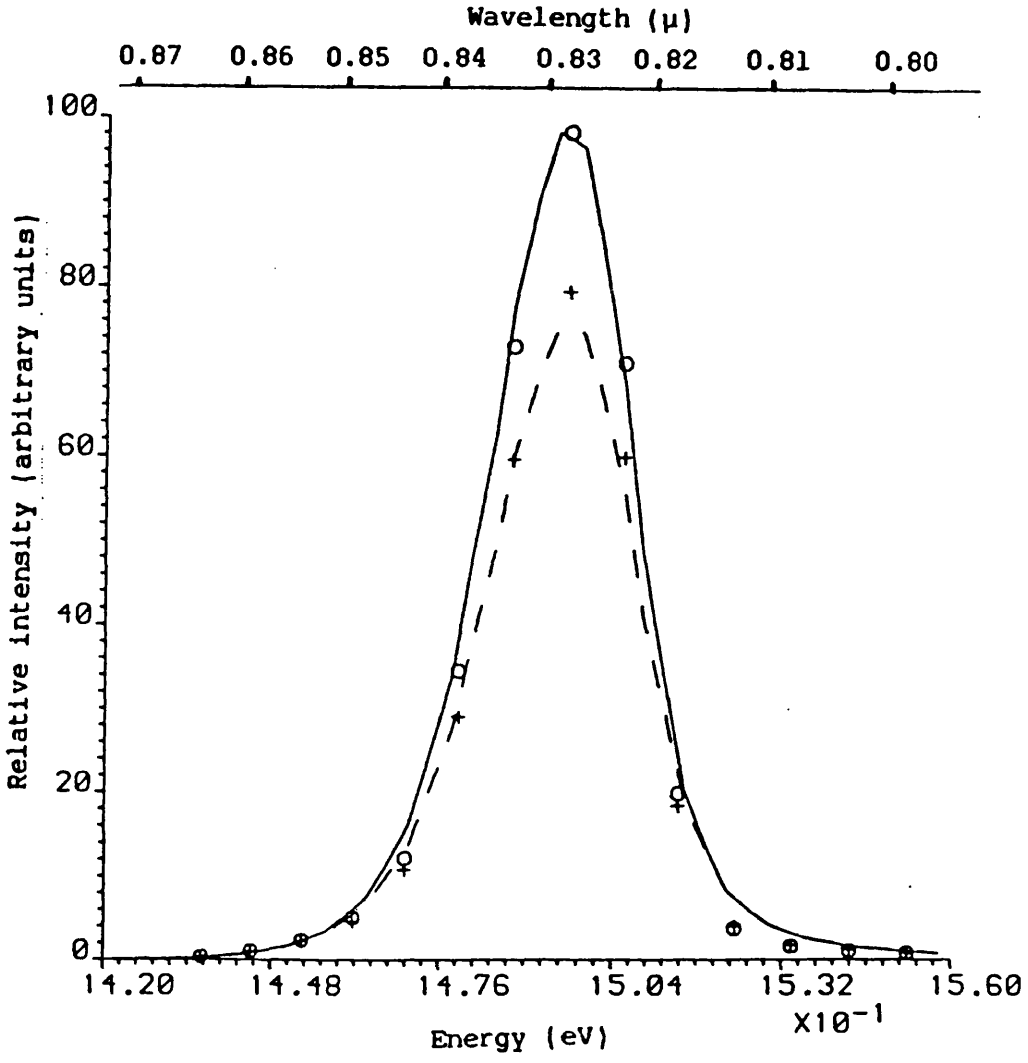

Fig(7.12) Comparison of the theoretical and experimental polarisation dependent spectra of SLD A291 at 300mA ($J = 3.68 \times 10^{3} A^{-2} cm$).

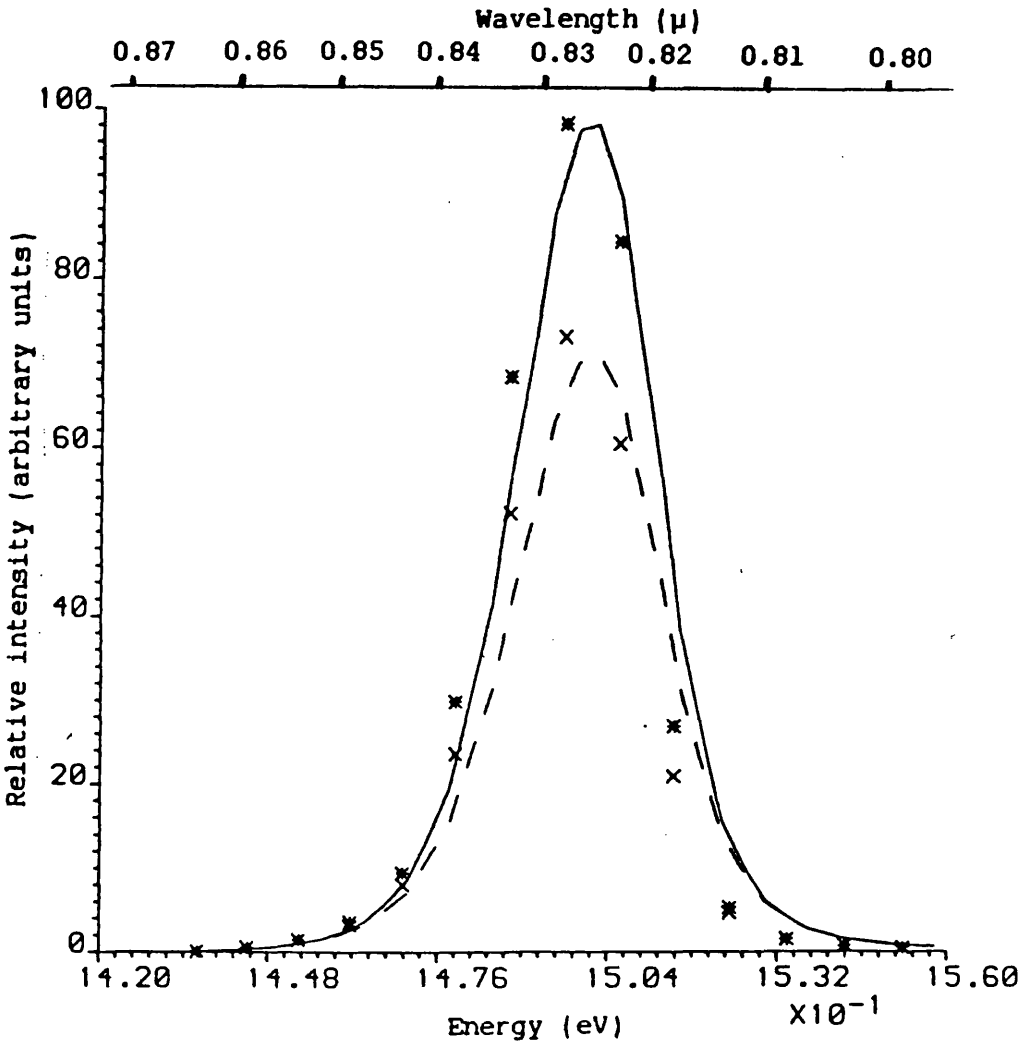

Fig(7.13) Comparison of the theoretical and experimental polarisation dependent spectra of SLD A291 at 400mA ($J = 4.91 \times 10^{3}$ A cm^{-2}).

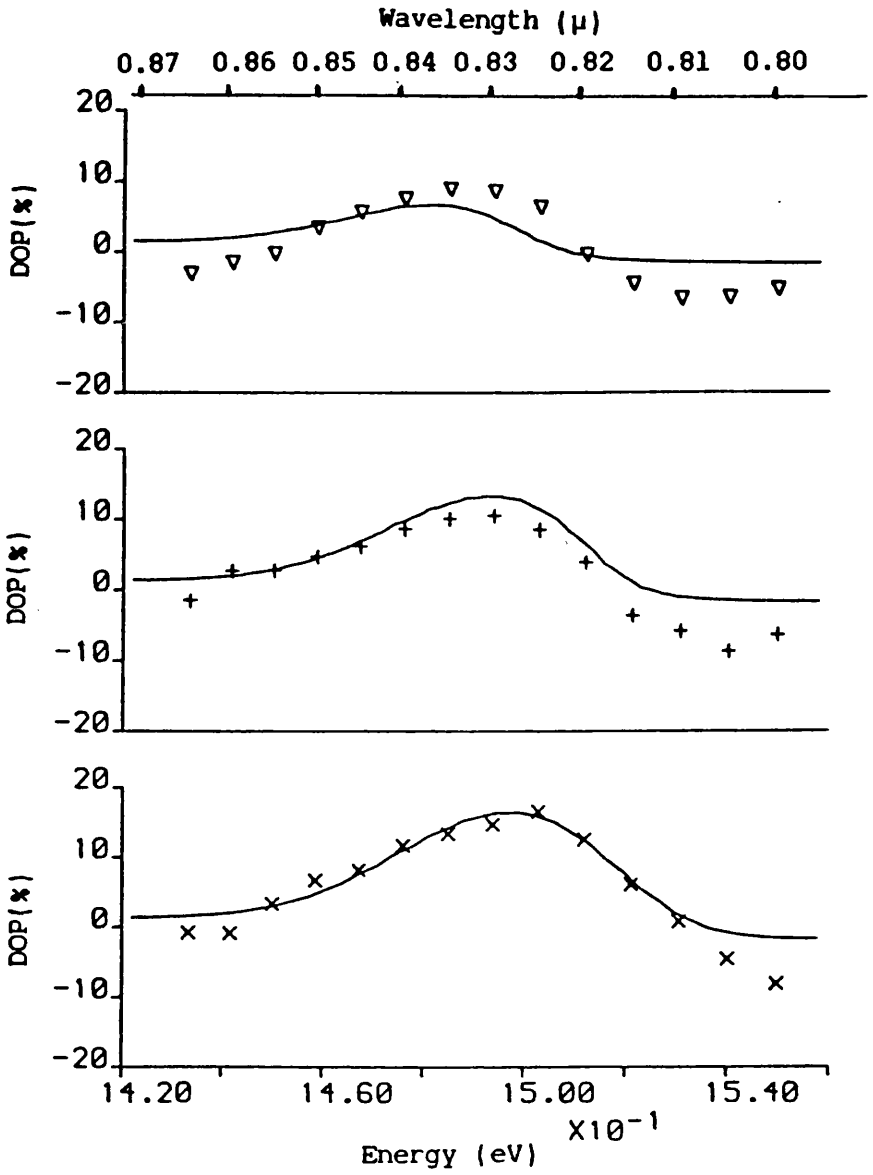

Fig(7.14) Comparison of the theoretical and experimental variation of the degree of polarisation with energy for SLD A291. The three plots correspond to different currents, from top to bottom I = 200, 300 and 400 mA (J = 2.45, 3.68 and 4.91 x10^{3} A cm^{-2}).

and becomes negative at the same wavelengths as the local gain.

A further example of the variation of the DOP with wavelength is given in fig(7.15) for the SLD, A547. Again each graph corresponds to a different current density. In these particular figures it is noticable that at high energies the experimental data seems to reach a minimum DOP somewhat below the theoretically predicted value before rising again. This is also evident to a lesser extent in the experimental results for the SLD, A291. Whether or not this is a real effect or some systematic error in the experimental measurement is not clear. This behaviour occurs at the very extreme of the spectrum where power levels are very low indeed thus making the possibility of experimental error much more likely.

7.6 Conclusion.

The polarisation characteristics of SLDs have been investigated using the model developed in chapter(4). It has been found that the DOP of an SLD can be matched to a high degree of accuracy, for a number of devices, using suitable values for the TE and TM confinement factors, reflectivities and the fraction of spontaneous emission entering each mode. A simple analytic expression for the DOP of an SLD showed that the difference in the TE and TM confinement factors dominated the change in the DOP with current density. It has also been shown that it is possible to match experimental and theoretical DOP curves using different combinations of the fraction of spontaneous emission coupling to the TE and TM modes and TE and TM modal reflectivities. This was demonstrated using the SLD model by keeping the fraction of spontaneous emission entering each mode equal and varying the modal reflectivities. The values for the TE and TM reflectivities necessary to obtain good

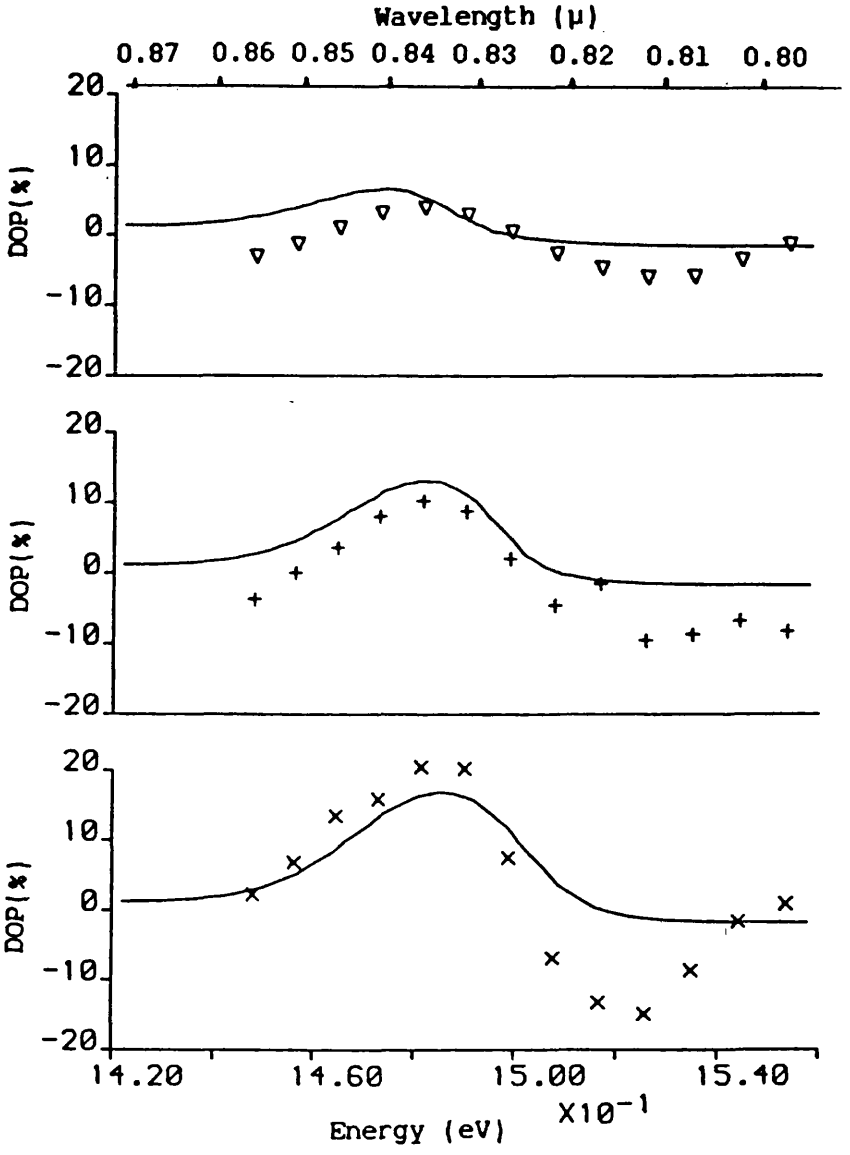

Fig(7.15) Comparison of the theoretical and experimental variation of the degree of polarisation with energy for SLD A547. The two plots correspond to different currents, top I=300mA ($J = 1.96 \times 10^{3}$ A cm^{-2}), bottom I = 400mA ($J = 2.61 \times 10^{3}$ A cm^{-2}).

agreement between the theoretical and experimental DOP curves were however unrealistic, the TE reflectivity being less that the TM reflectivity. If these values were in fact correct semiconductor lasers would lase in TM modes rather than TE modes. It is therefore concluded that the fraction of spontaneous emission entering the TE mode is certainly greater than that entering the TM mode. The actual values for the fraction of spontaneous emission entering the TE and TM modes used successfully to match all of the measured SLDs, with modal reflectivities, $R_{TE} = 0.38$ and $R_{TM} = 0.26$ obtained from [11], were $\delta_{TE} = 0.555$ and $\delta^{TM} = 0.455$ respectively.

The polarisation dependent spectra of a number of SLDs have been measured and compared with results obtained from the theoretical model. The agreement is quite reasonable, but by no means perfect. The discrepency may be due to the presently used method of measuring the polarisation dependent spectra and the fact that errors are compounded in the DOP calculation. What is more important, however, is the fact that both experiment and theory show similar trends. They both show that the DOP peaks and goes negative at the same wavelengths as the local gain curves. This behaviour is expected from the analytic expression for the DOP, equation(7.5), which shows that any change in the DOP occurs because of the TE and TM modal gains.

References;-

1) 'Low drift fibre gyro using a superluminescent diode', K.Bohm, P.Marten, K.Petermann, E.Weidel and R.Ulrich, Electron. Lett., vol.17, p352, 1981.

2) 'High-power low-divergence superradiance diode', C.S.Wang, W.H.Cheng, C.J.Hwang, W.K.Burns and R.P.Moeller, Appl.Phys.Lett., vol.41, no.7, p587, 1982.

3) 'Investigation of superluminescence emitted by a gallium arsenide diode', L.N.Kurbatov, S.S.Shakhidzhanov, L.V.Bystrova, V.V.Krapukhin and S.I.Kolonenkova, Sov. Phys.-Semicond., vol.4, no.11, p.1739, 1971.

4) 'A stripe-geometry double-heterostructure amplified-spontaneous-emission (superluminescent) diode', T.P.Lee, C.A.Burrus,Jr. and B.I.Miller, IEEE J. of Quant. Electron., vol.QE-9, no.8, 1973.

5) 'Polarisation characteristics of a travelling-wave-type semiconductor laser amplifier', J.C.Simon, Electron. Letts., vol.27 no.18 p.438, 1982.

6) 'Computer modelling of semiconductor laser amplifiers', I.Middlemast and J.Sarma, presented at 'SILA 84', Cardiff, 1984.

7) 'Noise characteristics of stripe-geometry double heterostructure junction lasers operating continuously-1.Intensity noise at room temperature', T.L.Paoli IEEE J. of Quant. Electron., vol.QE-11, p.276, 1975.

8) 'Physics of Semiconductor Laser Devices', G.H.B.Thompson, John Wiley and sons, 1980.

9) 'Analysis of diode laser properties', W.Streifer, D.R.Scifres and R.D.Burnham, IEEE J. of Quant. Electron., vol.QE-18, p.487, 1982.

10) 'Analysis of spontaneous emission effects on spectra and L vs I characteristics of diode lasers', W.Streifer, D.R.Scifres and

R.D.Burnham, Japan. J. of Appl. Phys., vol.21, pL282, 1982.

11) 'Reflectivity of mode at facet and oscillation mode in double-heterostructure injection lasers', T.Ikegami, IEEE J. of Quant. Electron., vol.QE-8, p470, 1972.

CHAPTER 8

CONCLUSIONS

8.1 Introduction.

A comprehensive model of the SLD was described in chapter(4). Many new features have been included in this model. They include: 1) an approximate method for reducing the two-dimensional photon and charge conservation equations into a one dimensional form, which however, still yeilds the lateral far-intensity distribution; 2) a detailed representation of the wavelength dependency of the local gain and the spontaneous emission derived from the basic semiconductor band structure, chapter(2); 3) the inclusion of polarisation dependent confinement factors, reflectivities and seperate coupling factors for each polarised mode. Consequently this model is capable of reproducing the light/current characteristics, spectral distribution, far-intensity 'angular' distribution and polarisation dependent characteristics of SLDs.

A comparison between theoretical results, obtained from the SLD model, and experimental measurements made on a number of SLDs has been carried out. Good agreement between the theoretical and experimental light/current characteristics, over a large range of current densities, was obtained for half of the measured SLDs. Considering that the characteristics of semiconductor devices, such as SLDs and lasers, vary from device to device, and the limited number of SLDs available for measurement, a fifty percent match is quite acceptable. Device characteristics vary primarily because of the difficulty in growing double-heterostructure material with consistent properties, although other factors such as bad contacting

and degradation are also important. It was also demonstrated that, by altering the radiative recombination efficiency for individual SLDs, agreement between experiment and theory could be obtained for all but one of the measured SLDs. Changing the radiative recombination efficiency is acceptable because it compensates for material defects which act as non-radiative recombination centres.

The use of realistic local gain and spontaneous emission curves in the theoretical model has been shown to be justified by the very good agreement obtained between the theoretical and experimental spectral distributions for all of the SLDs from one double heterostructure wafer. This agreement extended over a very wide range of wavelengths and current densities. Such extensive agreement between theoretical and experimental spectral distributions has not previously been reported. Slight changes in the bandgap were needed in the model to match the experimental measurements. This has the effect of shifting the whole spectral distribution in energy, without altering its shape or size significantly. The justification for altering the bandgap in the model is to account for the variation of the aluminium content in the active layer. The agreement between experiment and theory for SLDs from different wafers was, however, not so good. Much larger changes in the bandgap were necessary to match the experimental results, and the spectral distributions were narrower. These descrepencies are thought to arise from the different semiconductor properties displayed by different wafers.

The far-intensity angular distributions produced by the one-dimensional formulation of the photon and charge conservation equations in the SLD model show adequate agreement with experimental measurements. The theoretical angular distributions show a characteristic triangular peak and are narrower than the experimental

distributions. These features arise from the assumption of a constant inversion population and local gain in the lateral direction in the SLD model. It is, however, a much more complicated problem to include a lateral variation of the inversion population while maintaining the longitudinal dependent formulation. The simplicity of the one-dimensional formulation is particularly attractive. The increase in the accuracy of predicting the far intensity distribution that would be achieved by using a two-dimensional model does not warrant the extra computational time that would be needed.

The polarisation characteristics of SLDs have been investigated extensively and presented in chapter(7). It has been found that the degree of polarisation of an SLD can be matched to a high degree of accuracy using suitable values for the TE and TM confiement factors, reflectivities and fraction of spontaneous emission entering each mode in the SLD model. Good agreement between experiment and theory was in fact obtained for all of the measured SLDs. It has been demonstrated both numerically and analytically that the change in the DOP in an SLD is dominated by the difference in the TE and TM confinement factors. It has also been shown that the fraction of spontaneous emission entering the TE mode is greater than that entering the TM mode. In fact, if the values of reflectivity, obtained from [1], for the active layer thickness and refractive indices of the active and passive layers of the measured SLDs, are used in the SLD model the fractions of spontaneous emission entering the TE and TM modes needed to obtain a match with experiment are δ_{TE} = 0.555 and δ_{TM} = 0.455 respectively. This is a substantial difference and is a pertinent consideration of the noise properties of devices like the travelling wave amplifier.

The polarisation dependent spectral distributions of the

SLDs have also been measured and compared with theoretical results. The agreement between theory and experiment was reasonably good considering the method that had to be used for measuring the polarisation dependent spectra. More importantly, however, both theoretical and experimental DOP spectral distributions showed similar trends. The maximum value of the DOP for both theoretical and experimental spectral distributions coincided with the peak of the spectral distribution, and they also went negative at the same wavelength. This occured at the short wavelength side of the spectral distribution where the local gain goes negative. These results are, of course, expected from the analytic expression obtained for the DOP, in section (7.3), which links the change in the DOP to the local gain via the TE and TM confinement factors. These results add further weight to the fact that the fraction of spontaneous emission coupled into the TE mode is greater than that coupled into the TM mode.

The theoretical model has been used to analyse different methods for increasing the output power from SLDs. The most effective way of increasing the output power is to apply an anti-reflection coating to the output facet of the SLD. This has been shown to increase the output power of SLDs by a factor of four without any increase in drive current. No adverse side effects are produced by the antireflection coating. In fact, a slight reduction in the width of the spectral and far-intensity distributions was observed. The next best method of increasing the output power of SLDs was found to be to increase the length of the stripe contact. This has a beneficial effect on the spectral and far-intensity widths, both of which narrow with increasing length. These benifits, however, are at the expense of requiring an increase in the actual drive current needed to maintain the same current density.

The wavelength dependence of gain saturation has also been investigated in SLDs. It has been shown both numerically and analytically that the photon density at one wavelength can cause the photon density at a different wavelength to saturate with increasing length. This behaviour shows up more in the reverse travelling photon flux than in the forward travelling flux because of the larger value of the latter and only occurs at short wavelengths for which the local gain can become negative. It has also been shown numerically that saturation of the photon density at certain wavelengths occurs not only with length but also with current density. This behaviour was only found in the rear region of the stripe and occured at very short wavelengths where the photon density was extremely small.

8.2 Suggestions for further research.

The SLD model described in this project has already been developed into a Fabry-Perot amplifier model, [1], by altering the boundary conditions and including a field representation of the signals. Furthermore, with a further modification of the boundary conditions the effect of reflection from optical fibres on amplifier performance has been investigated, [2]. This demonstrates the ease with which a model of an active optical waveguide, such as the SLD, can be used to model other devices.

It has been shown that the polarisation dependent properties of the SLD stem partly from the difference in the TE and TM confinement factors and also from the fraction of spontaneous emission coupling into the TE mode being greater than that coupled into the TM mode. The theory for calculating the fraction of spontaneous emission coupling into the TE and TM modes is very involved, [3,4], but is certainly worthy of further investigation.

There is also scope for including the polarisation dependent ' values for the fraction of spontaneous emission couped into each mode into models of other devices, such as lasers and laser amplifiers. In particular these values will affect the noise performance of travelling wave amplifier models. The objective of such models is to obtain a reduction in the spontaneous emmission, a severe source of noise.

The modulation capacity of SLDs has been investigated, both experimentally, [5], and theoretically, [6]. The theoretical model, [6], however, only considered small signal modulation and did not include any spectral or angular dependencies. Developing a fully self consistent time dependent model of the SLD would be an obvious extension of the existing model. This type of model would be particularly useful for studying the self sustained oscillations that SLDs display when they are excessively pumped so that the absorbing region becomes transparent and lasing occurs. Such a model would, of course, have to take into account the optical pumping of the absorbing region. The inclusion of an absorbing region in the model opens a further avenue for research because devices with passive region have been shown to display bistability.

The SLD model could also be extended to take into account a non-uniform current density distribution along the length of the SLD. This could prove useful in enhancing the wavelength dependency of gain saturation by providing a larger gradient in the inversion population. This type of behaviour is of great interest in active integrated optics where many devices rely on a small change in one signal producing a large change in another, [7,8].

References

1) 'Computer simulation of Fabry-Perot laser amplifiers', I.Middlemast, J.Sarma, 'SILA' conference, Cardiff, 1984.

2) 'The effect of optical fibre coupling on the performance of laser amplifiers', Internal research report, Elec. Eng. Dept., Universiy of Bath, 1985.

3) 'Analysis of diode laser properties', W.Streifer, D.C.Scifres, and R.D.Burnham, IEEE J. of Quant. Electron., vol.QE-18, p. ,1982.

4) 'Analysis of spontaneous emission effects on spectra and L vs I characteristics of diode lasers', W.Streifer, D.C.Scifres, and R.D.Burnham, Jap. J. of Appl. Phys., vol.21, p.L282, 1982.

5) 'Modulation characteristics of double-heterostructure superluminescent diodes', M.C.Amann and W.Harth, Electron. Lett., vol.13, p.291, 1977.

6) 'On the theory of the superluminescent diode. 2 Small signal modulation', J.Boeck, M.C.Amann and B.Stegmuller.

7) 'Optooptic modulation based on gain saturation', R.W.Gray and L.W.Casperson, IEEE J. of Quant. Electron., vol.QE-14, p.893, 1978.

8) 'Proposals and analyses on laser amplifier based integrated optical circuits', K.Otsuka, IEEE J. of Quant. Electron., vol.QE-17, p.23, 1981.

Appendix A1

The symmetry of the SLD structure is such that a similar analysis can be applied to rays directed in both the '+θ' and '-θ' directions. This can be shown to be true by representing the symmetry of the photon density about $x = w/2$. Let $s = x - w/2$ and $p_{fk}(\theta,\lambda,z,x) \equiv p'_{fk}(\theta,\lambda,z,s)$, $p_{rk}(\theta,\lambda,z,x) \equiv p'_{rk}(\theta,\lambda,z,s)$. The symmetry can then be described by the relations

$$\begin{aligned} p_{fk}(\theta,\lambda,z,s) &= p'_{fk}(-\theta,\lambda,z,-s) \\ p'_{rk}(\theta,\lambda,z,s) &= p'_{rk}(-\theta,\lambda,z,-s) \end{aligned} \qquad \text{(A1.1)}$$

Following the same argument as was used to define the average photon density for $\theta \geq 0$ rays, equation (4.10), the corresponding definition for $\theta \leq 0$ rays is

$$P_{fk}(-\theta,\lambda,z) = 1/w \int_{g_\theta(z)}^{w} dx\, p_{fk}(-\theta,\lambda,z,x) = 1/w \int_{g_\theta(z)-w/2}^{w/2} ds\, p'_{fk}(-\theta,\lambda,z,x) \qquad \text{(A1.2)}$$

where $g_\theta(z) = (L-z)\tan|\theta|$. Next let $s' = -s$ so that

$$P_{fk}(-\theta,\lambda,z) = 1/w \int_{w/2-g_\theta(z)}^{-w/2} (-ds')\, p'_{fk}(-\theta,\lambda,z,-s') \qquad \text{(A1.3)}$$

$$= 1/w \int_{-w/2}^{w/2-g_\theta(z)} ds\, p'_{fk}(-\theta,\lambda,z,x)$$

Using the symmetry relation (A1.1) and noting that $h_\theta(z) = w - g_\theta(z)$, fig(A1.1), equation (A1.3) may be rewritten as

$$P_{fk}(-\theta,\lambda,z) = 1/w \int_{-w/2}^{w/2-g_\theta(z)} ds\, p'_{fk}(\theta,\lambda,z,s') \qquad \text{(A1.4)}$$

$$= 1/w \int_{0}^{w-g_\theta(z)} ds\, p'_{fk}(\theta,\lambda,z,x) = P_{fk}(\theta,\lambda,z)$$

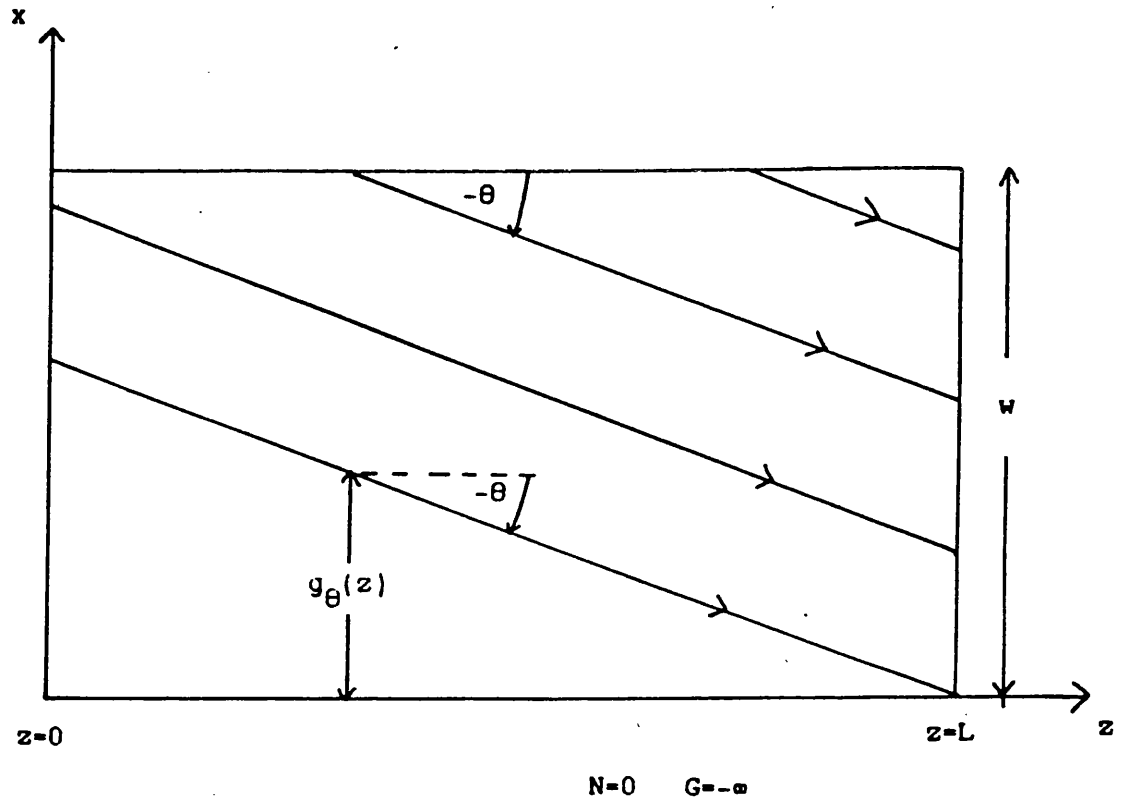

Fig(A1.1) Schematic diagram of the active region of the SLD showing rays travelling in a '-θ direction' and remaining totally within its boundaries. This provides the basis for the definition of the average photon density for '-θ' rays.

The fact that the same form of equation is obtained for both the '+θ' and '-θ rays is extremely useful because it means that it is only necessary to solve for positive values of 'θ' in the computer model, thus halving the ammount of computation time.

Appendix A2

The 'hard-edge' model of the SLD described in chapter 4 has been shown to display a 'straight-line' dependence with θ in its far-field distribution for small angles, chapter 5. This behavior can be shown analytically for low current densities where the inversion population can be assumed to be constant througout the length of the SLD. This means in fact that the inversion population is a constant value everywhere under the striped contact and zero elsewhere. The photon density distribution with x at z=L is constant in the range $L\tan(\theta) \leq x \leq w$ where the pathlength for all rays is the same but is non-uniform in the range $0 \leq x \leq L\tan(\leq)$ where the pathlength varies for all rays, fig(A2.1). Consequently the analytic solution for the photon distribution, equation(4.7), at z=L is seperated into two parts

$$p_f(\theta,L,x) = \frac{\delta_s R_{spon}(N)}{G(N)} \left\{\exp\left(\frac{G(N).L}{c.\cos(\theta)}\right) - 1\right\} \; ; \; x \geq L\tan(\theta) \qquad (A2.1)$$

$$p_f(\theta,L,x) = \frac{\delta_s R_{spon}(N)}{G(N)} \left\{\exp\left(\frac{G(N).x}{c.\sin(\theta)}\right) - 1\right\} \; ; \; x \leq L\tan(\theta)$$

where the wavelength and polarisation dependencies have been omitted for brevity. The total ammount of 'θ-directed' photons emitting from the output facet at z=L, $0 \leq x \leq w$ is then given by

$$P_f(\theta,L) = \int_0^w dx \; p_f(\theta,L,x) \qquad (A2.2)$$

which when applied to equation (A2.1) gives

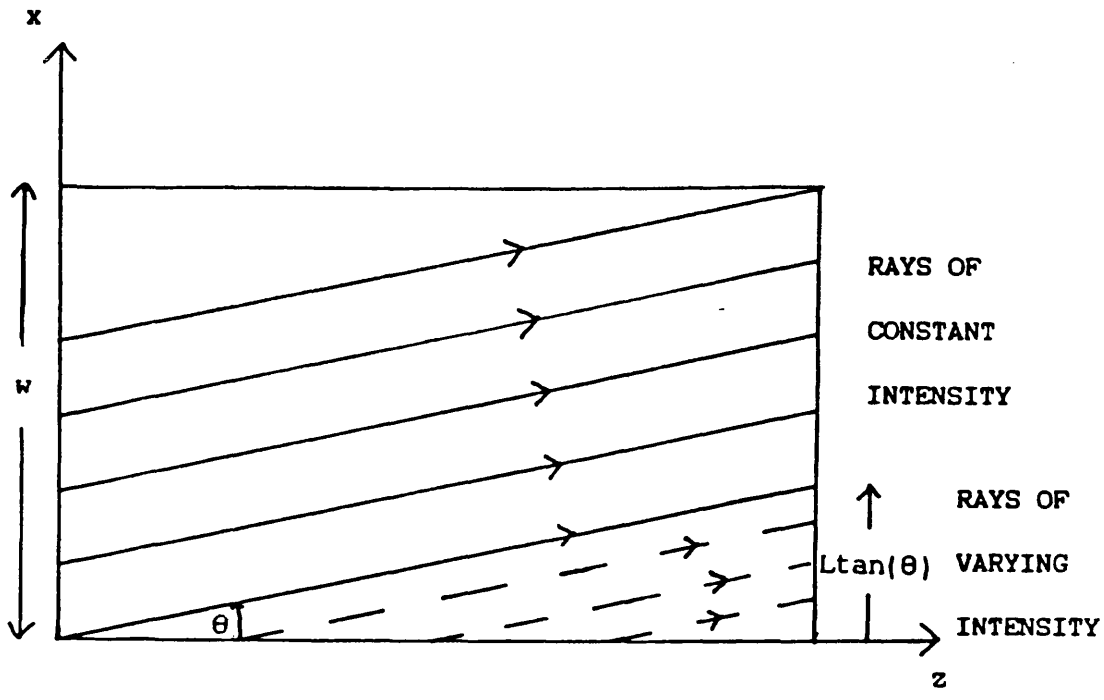

Fig(A2.1) Schematic diagram of the active region of the SLD showing rays of constant intensity at z=L between Ltan(θ) and w and varying intensity between 0 and Ltan(θ).

$$p_f(\theta,L) = \frac{\delta_s R_{spon}(N)}{G(N)} \left\{(w-L\theta)\exp\left(\frac{G(N).L}{c}\right) - w + \frac{c\theta}{G(N)}\exp\left(\frac{G(N)}{c}\right) - 1\right\} \quad \text{(A2.3)}$$

where θ has been assumed to be small so that $\cos(\theta) \cong 1$, $\sin(\theta) \cong \theta$ and $\tan(\theta) \cong \theta$. The '$\theta$' dependence in this equation lies outside of the exponential terms indicating that the angular distribution has a linear dependence on 'θ' for small angles. This agrees with the computed results in chapter(5).